DEPARTMENT OF PHYSICS
UNIVERSITY OF JYVÄSKYLÄ
RESEARCH REPORT No. 5/2009

MOLECULAR DEVICES FOR NANOELECTRONICS AND PLASMONICS

BY
ANTON KUZYK

Academic Dissertation
for the Degree of
Doctor of Philosophy

To be presented, by permission of the
Faculty of Mathematics and Science
of the University of Jyväskylä,
for public examination in Auditorium FYS-1 of the
University of Jyväskylä on August 7, 2009
at 12 o'clock noon

Jyväskylä, Finland
August 2009

Preface

The work reviewed in this thesis has been carried out during the years 2005-2009 at the Department of Physics at the University of Jyväskylä and at the Department of Applied Physics at the Helsinki University of Technology.

I want to thank all the people who were involved in research presented in this thesis. I was lucky to work together with Tommi Hakala, Dr. Jussi Toppari, Dr. Mika Pettersson and Prof. Henrik Kunttu. I would also like to acknowledge Dr. Sampo Tuukkanen, Dr. Vesa Hytönen, Teemu Ihalainen, Einari Niskanen, Veikko Linkko, Kimmo Laitinen and Hanna Tikkanen for their valuable contributions. I was fortunate to collaborate with Prof. Bernard Yurke, who introduced me to the fascinating world of DNA self-assembly. I also wish to thank all the people in the Nanoscience Center at the University of Jyväskylä and in the Department of Applied Physics at the Helsinki University of Technology, especially members of nanoelectronics and quantum dynamics groups, for creating an open and pleasant working atmosphere.

Above all I want to express my gratitude to Prof. Paivi Törmä. It is my great honor and pleasure to work under her guidance.

Finally, I wish to thank my family and relatives for their support and encouragement throughout all years of my studies.

Financial support from the Finnish National Graduate School in Nanoscience, Finnish Foundation for Technology Promotion and Magnus Ehrnrooth Foundation are gratefully acknowledged.

Espoo, April 2009

Anton Kuzyk

Abstract

Kuzyk, Anton

Jyväskylä: University of Jyväskylä, 2009, 79 p.
(Research report/Department of Physics, University of Jyväskylä,
ISSN 0075-465X; 05/2009
ISBN 978-951-39-3577-1 PDF 978-951-39-3578-8
diss.

This thesis is focused on fabrication and characterization of molecular devices. In connection with molecular electronics the dielectrophoresis based method for trapping and attaching nanoscale double-stranded DNA between nanoelectrodes was developed. Moreover, the method was extended to self-assembled DNA nanostructures. The method allowed to obtain valuable information about electrical and dielectrophoretic properties of DNA. In addition, two general approaches to the utilization of DNA origami structures for the assembly of materials are described and experimentally demonstrated.
In context of molecular plasmonics, a novel lithographic fabrication method for positioning dye molecules on plasmonic waveguides was developed. The potential for utilization of fluorescent molecules as couplers between far-field light and plasmons in microscale waveguides was explored. Energy transfer, mediated by surface plasmons, from donor molecules to acceptor molecules over ten micrometer distances was demonstrated. Moreover, it was showed that beside excitation and detection, fluorescent molecules can be used to manipulate properties of surface plasmons, e.g., to convert the frequency of propagating plasmons.

Keywords DNA, DNA self-assembly, dielectrophoresis, dyes, surface plasmons.

Author's address Anton Kuzyk
Department of Applied Physics
Helsinki University of Technology
Finland

Supervisor Professor Päivi Törmä
Department of Applied Physics
Helsinki University of Technology
Finland

Reviewers Professor Martti Kauranen
Optics Laboratory
Insitute of Physics
Tampere University of Technology
Finland

Professor Sebastiaan van Dijken
Department of Applied Physics
Helsinki University of Technology
Finland

Opponent Professor Friedrich C. Simmel
Physics Department E14
Technical University of Munich
Germany

List of Abbreviations

3′ end of ssDNA	phosphate end-group linked to 3^{rd} carbon in the sugar.
5′ end of ssDNA	hydroxyl end-group linked to 5^{th} carbon in the sugar.
A-DNA	double helix in A-form (dried B-form)
AFM	atomic force microscopy
B-DNA	double helix in B-form
bp	base pair(s)
C30	Coumarin 30
CNT	carbon nanotube
FRET	Föster type of resonance energy transfer (FRET).
DEP	dielectrophoresis
DFT	density functional theory
DNA	deoxyribonucleic Acid
dsDNA	double-stranded DNA
DTPA	dithiol-phosphoramidite
EBL	electron beam lithography
EDTA	ethylenediaminetetraacetic acid
ET	electron transfer
FET	field effect transistor
H-DNA	DNA triple helix structure
Hepes	N-2-Hydroxyethylpiperazine-N′-2-ethanesulfonic acid, ($C_8H_{18}N_2O_4S$)
ITO	Indium tin oxide
I–V	current–voltage
λ-DNA	DNA isolated from bacteriophage lambda
LPCVD	low-pressure chemical vapour deposition
MW	molecular weight
MWCNT	multi-walled carbon nanotubes
$NaBH_4$	Sodium borohydride
PCR	Polymerase Chain Reaction
PMMA	polymethylmethacrylate
poly(dA)-poly(dT)	dsDNA formed of adenine- and thymine-polynucleotides
poly(dC)-poly(dG)	dsDNA formed of cytosine- and guanine-polynucleotides

QD	Quantum dot
R6G	Rhodamine 6G
RH	relative humidity
RIE	reactive-ion etcher
SA	self-assembly
SEM	scanning electron microscope
SERS	surface enhanced Raman scattering
SNOM	scanning near-field optical microscope
SPCE	Surface plasmon coupled emission
ssDNA	single-stranded DNA
STM	scanning tunneling microscopy
STV	streptavidin
SWCNT	single-walled carbon nanotube
TAE	Tris-acetate-EDTA (ethylenediaminetetraacetic acid)
TCEP-HCl	Tris(2-Carboxyethyl) Phosphine and Hydrochloride
TEM	transmission electron microscopy
UHV	ultra-high vacuum
Z-DNA	double helix in left-handed Z-form

List of Publications

The main results of this thesis have been reported in the following articles:

PART I

I.I S. TUUKKANEN, A. KUZYK, J. J. TOPPARI, V. P. HYTÖNEN, T. IHALAINEN, AND P. TÖRMÄ, "Dielectrophoresis of nanoscale doublestranded DNA and humidity effects on its electrical conductivity". Appl. Phys. Lett. **87**, 183102 (2005).

I.II S. TUUKKANEN, J. J. TOPPARI, A. KUZYK, L. HIRVINIEMI, V. P. HYTÖNEN, T. IHALAINEN, AND P. TÖRMÄ, "Carbon nanotubes as electrodes for dielectrophoresis of DNA". Nano Lett. **6**, 1339 (2006).

I.III S. TUUKKANEN, A. KUZYK, J. J. TOPPARI, H. HÄKKINEN, V. P. HYTÖNEN, E. NISKANEN, M. RINKIÖ, AND P. TÖRMÄ, "Trapping of 27 bp-8 kbp DNA and immobilization of thiol-modified DNA using dielectrophoresis". Nanotechnology **18**, 295204 (2007).

I.IV A. KUZYK, B. YURKE, J. J. TOPPARI, V. LINKO, AND P. TÖRMÄ, "Dielectrophoretic trapping of DNA origami". Small **4**, 447 (2008).

I.V A. KUZYK, K. T. LAITINEN, AND P. TÖRMÄ, "DNA origami as a template for protein assembly". Nanotechnology **20**, 235305 (2009).

PART II

II.I A. KUZYK, M. PETTERSSON, J. J. TOPPARI, T. K. HAKALA, H. TIKKANEN, H. KUNTTU, AND P. TÖRMÄ, "Molecular coupling of light with plasmonic waveguides". Opt. Express **15**, 9908 (2007).

II.II T. K. HAKALA, J. J. TOPPARI, M. PETTERSSON, A. KUZYK, H. TIKKANEN, H. KUNTTU, AND P. TÖRMÄ, "Frequency conversion of propagating surface plasmon polaritons by organic molecules". Appl. Phys. Lett. **93**, 123307 (2008).

Other publications to which the author has contributed

1 YU. DEMIDENKO, A. KUZYK, V. LOZOVSKI AND O. TRETYAK, "A system of hidden quantum dots in the magnetic field: a near-field approach". J. Phys.: Condens. Matter **16**, 543 (2004).

2 S. TUUKKANEN, J. J. TOPPARI, V. P. HYTÖNEN, A. KUZYK, M.S. KULOMAA, AND P. TÖRMÄ, "Dielectrophoresis as a tool for nanoscale DNA manipulation". Int. J. Nanotechnology **2**, 280291 (2005).

3 T. K. HAKALA, J. J. TOPPARI, A. KUZYK, M. PETTERSSON, H. TIKKANEN, H. KUNTTU AND P. TÖRMÄ, "Vacuum Rabi splitting and strong coupling dynamics for surface plasmon polaritons and Rhodamine 6G molecules". Submitted arXiv:0902.0710.

4 V. LINKO, S. PAASONEN, A. KUZYK, P. TÖRMÄ, AND J. J. TOPPARI, "Characterisation of the conductance mechanisms of the DNA origami by AC impedance spectroscopy". Submitted.

5 T. K. HAKALA, V. LINKO, A. P. ESKELINEN, J.J TOPPARI, A. KUZYK, AND P. P. TÖRMÄ, "Field induced nano-imprint lithography for high-throughput pattern transfer". Submitted.

Author's contribution

In I.I the author carried out the main part of the sample fabrication, part of the electrical measurements and part of the analysis of the results.
In I.II and I.III the author carried out part of the sample fabrication and part of the

analysis of the results.
In I.IV and I.V the author carried out all the reported experiments.
In II.I the author carried out the main part of the sample fabrication and characterization.
In II.II the author participated in the analysis of the results.
The author is the main writer for the publications I.IV and I.V and participated in writing the publications I.I-I.III, II.I and II.II.

Contents

Preface i

Abstract iii

List of Abbreviations v

Introduction 1

I DNA molecular devices for nanoelectronics 3

1 Background 5
1.1 DNA structure 5
1.1.1 Deoxyribonucleic acid 5
1.1.2 DNA double helix 6
1.2 Self-assembly and DNA Nanotechnology 7
1.2.1 Two- and three-dimensional self-assembled DNA structures . 9
1.2.2 DNA origami 10
1.2.3 Assembly of materials using DNA self-assembly 11
1.3 DNA conductivity 12
1.4 Dielectrophoresis 14

2 Dielectrophoretic trapping and polarizability of DNA molecules 19
2.1 Dielectrophoresis of double stranded DNA 19
2.1.1 DEP trapping with lithographically fabricated electrodes . . . 19
2.1.2 DEP trapping with CNT electrodes 20
2.2 Polarizability of DNA molecules 23
2.3 Immobilization of the trapped DNA molecules on the electrodes . . . 25

3 Measurements of electrical properties of DNA molecules 27

4 DNA origami as a nanobreadboard 31
4.1 Connecting DNA origami to the outer world 31
4.2 Assembly of materials using DNA origami 35

5 Conclusions 41

References 43

II Molecular devices for plasmonics **47**

6 Background **49**
6.1 Surface plasmon polaritons 49
6.2 Coupling of light to surface plasmons 51
6.3 Molecular plasmonics 53
6.3.1 Decay of excited molecules to SPs 53
6.3.2 Detection of SPs with fluorescent molecules 54

7 Excitation, detection and frequency conversion of SPs with molecules **57**
7.1 Fabrication of plasmonic waveguides with molecules 57
7.2 Coupling between light and surface plasmons using molecules . . . 58
7.2.1 Plasmon propagation 58
7.2.2 Incoupling of plasmons by molecules 61
7.2.3 Outcoupling of plasmons by molecules 63
7.2.4 Efficiency of the energy transfer 64
7.3 Frequency conversion of propagating plasmons 65

8 Conclusions **69**

References **71**

III Appendices **73**

A Materials and methods (DNA related studies) **75**
A.1 Nanoelectrodes fabrication 75
A.2 Carbon nanotube electrode fabrication 75
A.3 Fabrication of DNA fragments and thiol-modified DNA 76
A.4 Preparation of DNA solution 77
A.5 Charging effects 78
A.6 Fabrication of DNA origami 80

B Materials and methods (molecular plasmonics) **85**
B.1 Waveguide fabrication and deposition of molecules 85

Introduction

Throughout the history, the technological development of humankind was driven by ability to learn and utilize properties of new materials. Some of the first tools used by man were made of stone, followed by bronze and iron. As a time went by, we learned to use large variety of materials which are found in Nature, but more importantly, we also learned to fabricate and utilize materials with desired properties. An excellent example is silicon; our ability to process it and use its electric properties has changed the world profoundly. From the chemical point of view, materials can be classified into two big categories, organic and inorganic compounds. Historically it happened that inorganic compounds are the most widely used nowadays, probably due to large natural availability and relatively simple processing. Unfortunately the properties of inorganic compounds can be modified only to a certain extend. This comes from the relative simplicity of composition. One the other hand organic compounds offer the possibility of complex composition and thus functionality (life is a perfect example for both). An enormous progress in chemical synthesis can be now used to create materials with large variety of desired properties. There is a general trend to wider utilization of organic compounds in the areas dominated previously by inorganic compounds, for example in electronics and light emitting devices. One can also think about using organic compounds from the living word, in a sense, those are evolution-optimized chemistry incarnates with a lot of unique properties. Utilization of organic compounds, both at the level of single molecule and of molecular assemblies, opens new interesting possibilities in many areas of research and technology. Controlled positioning on a chip is one of the crucial open challenges in application of single molecules and molecular assemblies in nanotechnology.

This thesis focuses on two different areas of application of organic molecules, and development of methods for positioning constitute a large part of the thesis. In Part I, DNA and the use of its exceptional self-assembly properties in nanotechnology are explored. Specifically, the following topics are discussed i) manipulation of DNA and DNA self-assembled structures in nanoscale using dielectrophoresis ii) DNA electrical conductivity iii) utilization of DNA for nanostructures fabrication and material assembly. The structure of this part of the thesis is the following. Chapter 1 provides the reader with basic information about DNA, its self-assembly properties and electrical conductivity. The chapter also gives background

information about dielectrophoresis. Experiments on dielectrophoretic trapping of DNA molecules are described in Chapter 2 and on electrical measurements in Chapter 3. Chapter 4 describes experiments on dielectrophoretic trapping of DNA self-assembled structures and assembly of materials using DNA structures as nanoscale templates. Conclusions are presented in Chapter 5. Detailed information on materials and methods used for the experiments is given in Appendix A.

Part II is focused on questions of molecular plasmonics, i.e., the use of fluorescent molecules for excitation, detection, and manipulation of surface plasmons. The structure of this part of the thesis is the following. Chapter 6 gives background information about surface plasmon polaritons and molecular plasmonics. Chapter 7 describes experiments on utilization of fluorescent molecules for excitation, detection and manipulation of surface plasmons. Conclusions are given in Chapter 8. Detailed information on materials and methods used for the experiments is given in Appendix B.

Part I

DNA molecular devices for nanoelectronics

1. Background

Deoxyribonucleic acid (DNA) is probably the most important molecule in the living world. Its main function is the long-term storage of information; it encodes the architecture and function of cells in a living organism. It is not surprising that for such an important function Nature chose a molecule with a lot of unique properties. From nanotechnology point of view DNA has a number of appealing features[1]: it is intrinsically nanoscale object with a diameter of about 2 nm, it has a short structural repeat (helical pitch) of about 3.4-3.6 nm, it has excellent mechanical properties (single-stranded DNA is a flexible molecule, whereas double-stranded DNA is relatively rigid in the length scale of about 50 nm) and probably the most important/useful property of DNA is complementarity (see below). In addition a rich toolbox is provided by both Nature and DNA biochemistry: DNA of wanted sequence can be synthesized at will (it is not very straightforward for most polymers), DNA can be cut at desired places and joined, variety of chemical modifications with certain functionality can be introduced at different positions of DNA.

Since the discovery of DNA helical structure in 1953 by Watson and Crick[2], properties and functions of DNA were studied extensively, some of them are well known already and some are still under debate. Recent advances in nanotechnology and nanofabrication made it possible to get new information and knowledge about DNA on a single molecule level. For example, structure of DNA and its interactions with other molecules, e.g. proteins, can be directly observed with scanning tunneling microscopy (STM)[3,4] and atomic force microscopy (AFM)[5,6]. Experiments on direct measurement of DNA electrical conductivity properties became realizable[7]. There are many exciting ways how DNA can be used in nanotechnology, and how nanotechnology can be used to discover new functions and properties of DNA.

1.1 DNA structure

1.1.1 Deoxyribonucleic acid

Single stranded DNA (ssDNA) is a polymer of deoxyribonucleotides (nucleotides), each of which contains a deoxyribose sugar, a phosphate and an aromatic nitrogenous base attached to the sugar. There are four different bases in DNA: Thymine (T), Cytosine (C), Adenine (A) and Guanine (G). Thymine and Cytosine are single ring structures called pyrimidines, and Adenine and Guanine are double ring structures called purines. Phosphate and sugar groups form a backbone of a DNA strand into which the bases are attached. Each DNA strand has a directionality. So called 5′ and

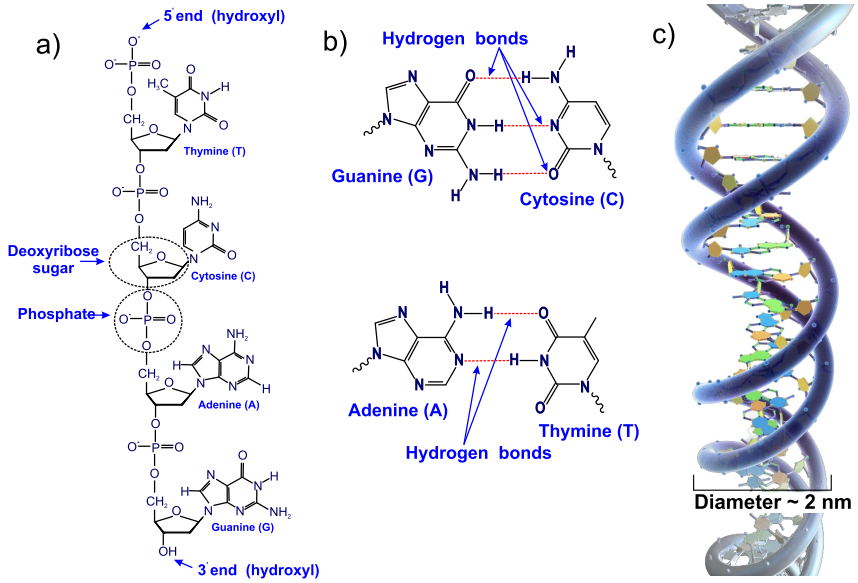

FIGURE 1.1 a) Schematic chemical structure of a single stranded DNA. b) Hydrogen bonding between bases. c) Helical structure of a double stranded DNA.

3′ ends are determined by the carbon atom (5th or 3rd) of the deoxyribose sugar into which the phosphate is attached. Chemical structure of ssDNA is schematically shown in Fig. 1.1a).

1.1.2 DNA double helix

DNA bases can form hydrogen bonds between each other in a very specific way. Adenine forms 2 hydrogen bonds with Thymine and Cytosine forms 3 hydrogen bonds with Guanine (see Fig. 1.1b)). This property is called complementarity. Double stranded DNA (dsDNA) is a complex of two ssDNA held together by hydrogen bonds between the complementary bases and has a helical form (see Fig. 1.1c)). Two strands are coiled in an antiparallel way, which means that one strand goes form 5′ to 3′ and the other from 3′ to 5′. Double-stranded DNA can have many possible conformations. Which conformation DNA adopts depends on the sequence of the DNA, the amount and direction of supercoiling, chemical modifications of the bases and also solution conditions. The structural configuration of DNA is thought to alter its electronic properties. In living organisms the so-called A-DNA, B-DNA, and Z-DNA forms have been observed. B-DNA is the most common type of DNA found in the cells of living organisms, it is the most stable structure for a random-sequence DNA molecule under physiological conditions and therefore it is a standard point of reference in any study of DNA properties. For this type of DNA, the center of the base pairs (bp) lies along the helix axis. The helix is right handed. The base pairs are separated by a distance of about 3.4 Å and are slightly tilted. There are, on average, 10.5 bp per each turn of the helix, which gives an average 36° angle between succes-

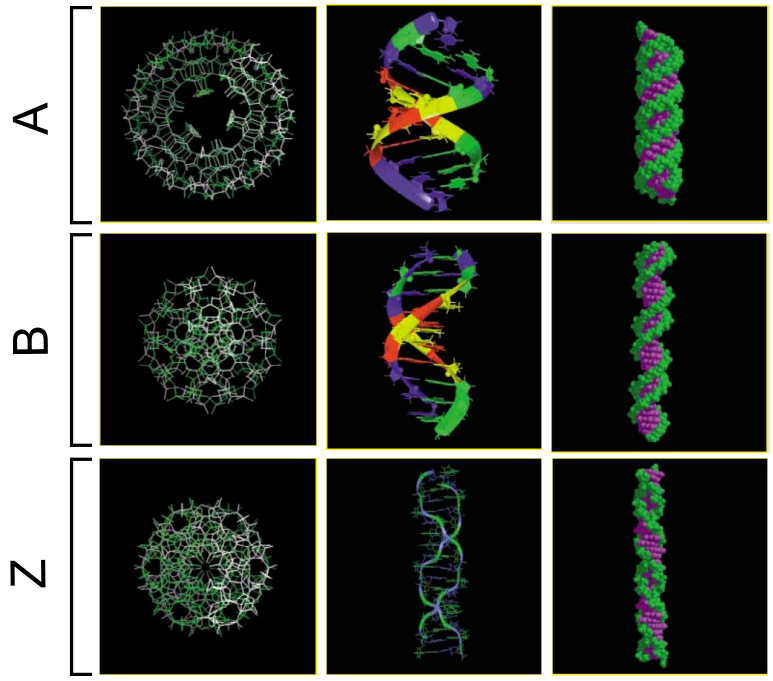

FIGURE 1.2 The A, B and Z DNA double helix forms

sive base pairs. More than 13 water molecules per nucleotide are required to form stable B-DNA form. A-DNA and Z-DNA are two structural variants. The A form is favored in many solutions that are relatively devoid of water. The A-DNA is still arranged in a right handed double helix, but the helix is wider and the number of base pairs per turn in A-DNA is 11. The plane of the bases is tilted about 20^o with respect to the helix axis. At least about 5-10 water molecules are necessary to form a more or less regularly ordered A structure. The Z-form is more radical departure from the B structure; the most obvious distinction is the left handed helical rotation. There are 12 bp per helical turn, and the structure appears more slender and elongated. The DNA backbone takes on zigzag appearance. The A-, B- and Z-DNA forms are shown in Fig. 1.2. In addition to these three forms there are many more exotic froms[8]: H-DNA[9] with a triple helical structure, four-stranded G-quadruplexes[10], C-DNA, D-DNA, E-DNA, L-DNA, P-DNA, S-DNA etc. In fact, only the letters F, Q, U, V, and Y are now available to describe any new DNA structure that may appear in the future.

1.2 Self-assembly and DNA Nanotechnology

Self-assembly (SA) can be defined as the *spontaneous* and *reversible* organization of molecular units into ordered structures by non-covalent interactions. The first property of a self-assembled system that this definition suggests is the spontaneity

of the self-assembly process: the interactions responsible for the formation of the self-assembled system act on a strictly local level - in other words, the nanostructure builds itself. It can be argued that any chemical reaction driving atoms and molecules to assemble into larger structures, such as precipitation, could fall into the category of self-assembly. However, there are at least three distinctive features that make self-assembly a distinct concept:

Order. First, the self-assembled structure must have a higher order than the isolated components, be it a shape or a particular task that the self-assembled entity may perform. This is generally not true in chemical reactions, where an ordered state may proceed towards a disordered state depending on thermodynamic parameters.

Interactions. The second important aspect of SA is the key role of weak interactions (e.g. Van der Waals, capillary, π - π, hydrogen bonds) with respect to more "traditional" covalent, ionic or metallic bonds. Although typically less energetic by a factor 10, these weak interactions play an important role in materials synthesis. Weak interactions hold a prominent place in materials, especially in biological systems, although they are often considered marginal with respect to "strong" (i.e. covalent, etc.) interactions. For instance, they determine the physical properties of liquids, the solubility of solids, the organization of molecules in biological membranes.

Building blocks. The third distinctive feature of self-assembly is that the building blocks are not only atoms and molecules, but span a wide range of nano- and mesoscopic structures, with different chemical compositions, shapes and functionalities. These nanoscale building blocks can in turn be synthesized through conventional chemical routes or by other self-assembly strategies.

Molecular self-assembly is the process by which molecules adopt a defined arrangement without guidance or management from an outside source. It is crucial to the function of cells and is an important aspect of bottom-up approaches to nanotechnology. It has been put forth as an inexpensive, parallel method for the synthesis of nanostructures that does not require expensive equipment and extreme conditions.

DNA nanotechnology is a subfield of nanotechnology which is based on the self-assembly properties of DNA. As was described in Section 1.1.1, DNA base pairs form hydrogen bonds between each other in a very specific way (C forms 3 bonds with G and A forms 2 bonds with T). DNA nanonotechnology seeks to use these unique molecular recognition properties of DNA and other nucleic acids to create novel programable structures out of DNA. The DNA is thus used as a construction material rather than as a carrier of genetic information. This has possible applications in molecular self-assembly, molecular computing[11], nanoelectronics and optics[12].

1.2.1 Two- and three-dimensional self-assembled DNA structures

The idea of using DNA as as a structural material was first introduced by Ned Seeman in the early 80's[13]. Since the simple double-helix lacks the complexity needed for forming tightly controlled two- and three-dimensional structures, a more complex building block had to be designed. Seeman and co-workers succeeded in making branched junction motifs with four double-helical arms, which resemble Holliday junctions[14]. Each arm had region of ssDNA which was complementary to ssDNA region in another arm (so-called sticky ends). It was hoped that these branched units would assemble into a quadrilateral lattice by sticky end cohesion (see Fig. 1.3a)). Unfortunately the junctions did not assemble into a two-dimensional lattice because the structure was not stiff enough. Since the original idea of using DNA junctions

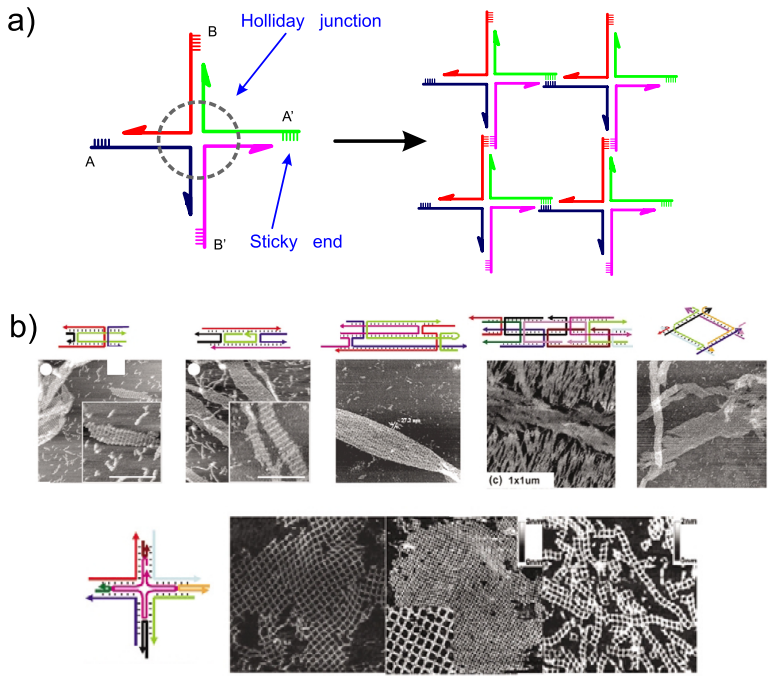

FIGURE 1.3 a) Schematic drawing of the four-armed junction proposed for two-dimensional lattice assembly via sticky ends cohesion. A and A', B and B' are complementary sequences. b) Schematic structures of common building blocks used to construct two-dimensional DNA arrays and examples of the corresponding assembled structures imaged with AFM. Adopted with permission from [15–20].

as a building blocks for assembly of two-dimensional structures, a large variety of distinct DNA building blocks (usually called tiles) have been designed and experimentally tested (see Fig. 1.3b))[15–20]. Besides two-dimensional lattices, assembly of three-dimensional DNA structures like nanotube[21–24], cube[25], octahedron[26], tetrahedra[27] and polyhedra[28] was demonstrated (for review see ref. [29]). However, the tile approach to assembly of DNA structures suffers from several serious limitations:

i) DNA sequences for tiles should be carefully designed to avoid secondary

structures and unwanted interactions. This task is far from being obvious.
ii) The possibility of fabrication of structures with controlled shapes/geometry or asymmetric arrays is rather limited.
iii) Synthesis of such nanostructures involves interactions between a large number of short oligonucleotides, the yield of complete structures is highly sensitive to stoichiometry (the relative ratios of strands). The synthesis of relatively complex structures requires multiple reaction steps and purifications and the yield is small.

1.2.2 DNA origami

There is an alternative approach to assembly of DNA structures. Instead of using DNA tiles as building blocks, it is based on folding linear DNA scaffold into complex structures. In 2004, Shih *et al.* showed that a single strand of DNA can be assembled into a octahedron by addition of 5 short DNA strands[26]. The most striking example of scaffolded assembly is the so-called DNA origami technique developed by Paul Rothemund in Caltech in 2006[30]. DNA origami is a two-dimensional structure made of 7.3 Kb single-stranded viral genome folded into desired shape with the help of short oligonucleotides (so-called staple strands). The schematic picture of DNA origami structure is given in Fig. 1.4a). The origami approach of DNA assembly is fast, extremely easy, relatively inexpensive and gives the possibility to create two-dimensional nanostructures of almost arbitrary shape with high yield (see Fig. 1.4b)). Furthermore, is has a few advantages compared to the tile approach:

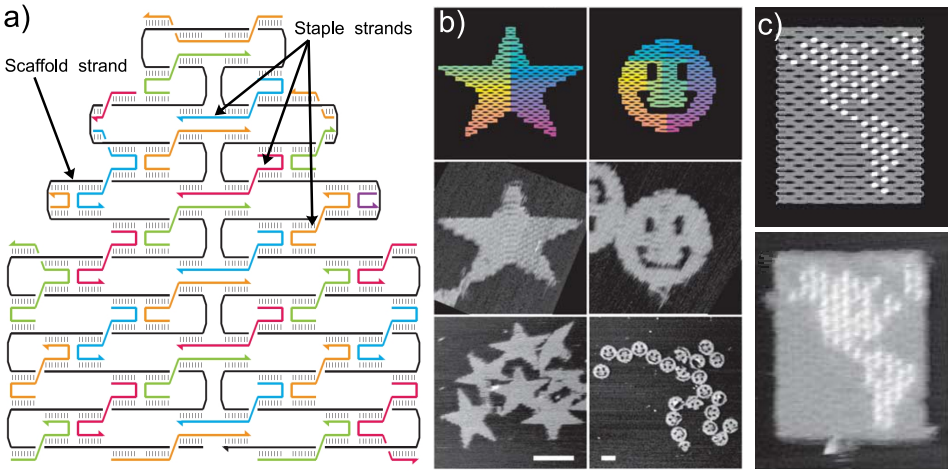

FIGURE 1.4 a) Schematic picture of DNA origami, long single stranded DNA (scaffold strand) is folded into the desired shape with the help of short oligos (staple strands). b) Examples of DNA origami structures. c) Patterning DNA origami using DNA hairpins. Adopted with permission from [30].

i) It is essentially "one-pot" method, it does not require multiple reaction steps and purifications.

ii) Staple strands are not designed to bind one another, thus, their relative concentrations are not important, and absolute concentrations do not need to be precise.
iii) One can uses unpurified staple strands, which reduces the cost of fabrication by a factor of 10.

Besides ability to create arbitrary shapes, DNA origami technique can have another very promising application. It can serve as template for assembly of materials (see the next Section 1.2.3). Already in his original paper[30] Rothemund demonstrated that its possible to decorate origami with complex patterns using DNA hairpins (loops of ssDNA) (see Fig. 1.4c)).

1.2.3 Assembly of materials using DNA self-assembly

As was mentioned before, DNA can be functionalised with various chemical groups. Some of those groups can serve as a binding sites for other materials (proteins, nanoparticles, semiconducting quantum dots etc.). Thus it possible to use DNA and DNA self-assembled structures as a template for assembly of materials[31]. First steps in this direction were taken using linear DNA. It was shown that it can be used as a template for fabrication of metal nanowires[32], assembly of proteins[33], nanoparticles[34] and carbon nanotubes[35]. Further on, it was demonstrated that two-dimensional DNA lattices can be used as templates for assembly of arrays of proteins[16,20,36,37], metal particles[38–41] and semiconducting quantum dots[42]. Examples of two-dimensional assembly of materials are given in Fig. 1.5a)-c). Utilization of DNA lattices as templates gives a possibility to fabricate large patterned structures with resolution comparable to the state of the art lithography techniques. However, it has one serious drawback; the two-dimensional DNA structures are usually periodic, and such periodic templates allow only periodic assembly of materials. Non-periodic assembly on the two-dimensional DNA templates build from the DNA tiles is rather complicated[37]. Another limitation comes from the fact that materials are usually assembled on prefabricated DNA templates, thus assembly of multiple materials requires utilization of multiple binding interactions.

One of the big advantages of the DNA origami technique is that, in principle, it allows programmable assembly of materials into arbitrary patterns. This is due to the fact that each of the staple strands it unique in sequence and its position inside the origami structure and can be functionalised separately. Therefore, the origami structure can serve as a nanoscale template, a "nanobreadboard", to a which a variety of components could be attached with nanometer resolution. The size and and the resolution (distance between two nearest pixels) of such breadboard is limited by lengths of the scaffold strand and the staple strands respectively. Realization of the "DNA origami as a nanobreadboard" idea can advance the assembly of materials by allowing programmable fabrication of non-periodic complex structures with

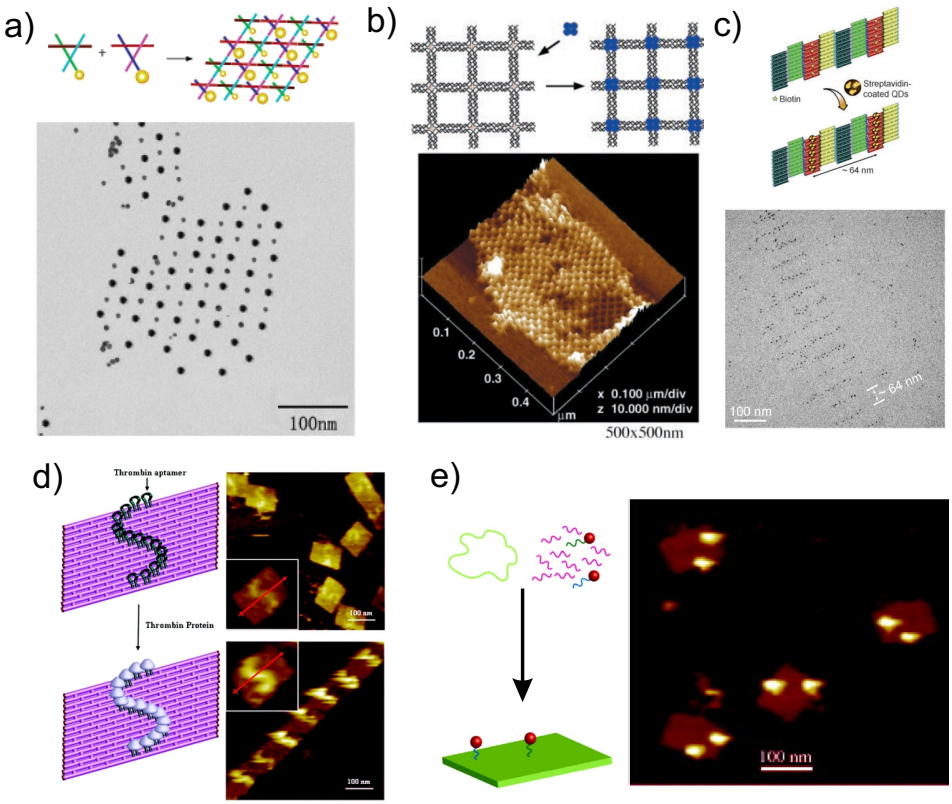

FIGURE 1.5 Assembly of materials using DNA as a template. a) Assembly of 5 nm and 10 nm gold particles into a two-dimensional array. b) Assembly of proteins . c) Assembly of semiconducting quantum dots. d) Assembly of proteins using DNA origami. Adopted from [38] (a), [16] (b), [42] (c), [43] (d) [44] (e).

below 10 nm resolution. The controlled attachment of proteins can find applications in biosensors, biomaterials, and tissue engineering. Ability of special arrangement of proteins with nanometer precision is of extreme importance for understanding fundamental bimolecular interactions. By attaching nanowires, carbon nanotubes or metal nanoparticles one can create molecular electronic or plasmonic circuits. So far, assembly of proteins (ref. [43] (see Fig. 1.5d)) and the paper **I.V.** of this thesis) and of two gold nanoparticles[44] (see Fig. 1.5e)) has been demonstrated with origami structures.

1.3 DNA conductivity

In 1962, soon after the discovery of DNA helical structure in 1953, Eley and Spivey suggested, that DNA molecules could act as electrical wires[45]. Later on, it was proposed that DNA, due to its unique properties of recognition and self-assembly, could be used as a building block for molecular electronics, where the basic concept is to use individual molecules as wires, switches, rectifiers, and memories[46]. To be

able to realize all these devices, the electrical properties of DNA and the charge transport/transfer mechanism should be investigated and understood at the single molecule level. Additionally, transport properties of DNA are of interest in several other fields, e.g. in genetic mutations and cancer therapy[47], and for DNA detectors based on its electrical properties[48]. It was thought that DNA could be a very promising molecule for studying electrical transport in a 1D system, because is gives a possibility of endless number of controlled structural manipulations (versus the hit and miss control in nanotubes), and charge transport mechanisms like hopping and tunneling can be studied in a controlled way.

A large number of reports on direct measurements of electrical conductivity on single DNA molecules was published in the late 1990's and the early 2000's. The pioneering work was done by Braun *et al.*[49], Fink and Schönenberger[50], Dekker and colleagues[51] and Kasumov *et al.*[52]. Already, the results obtained in those initial reports were somewhat contradicting: DNA was claimed to have metallic, semiconducting, insulating or even proximity induced superconducting properties. Unfortunately further research work did not bring full clarification into the field, conductivity measurements showed a large variety of possible electronic behavior and the whole field of DNA conductivity still remains highly controversial[7]. There are several factors that can influence the experimental results and should be taken into account:

The contact between the electrodes and the molecules. Ideally, these contacts should be ohmic so that any nonlinearity in the conductivity of the wire can be correctly attributed and studied. They must also be low in resistance to ensure that the properties measured are those of the molecule and not those of the molecule-contact interface. Moreover, the medium surrounding and supporting the molecule must be several orders of magnitude more insulating than the molecule itself because the contact area of the medium with the electrical contacts is often much greater than that between the electrical contacts and the molecule. The simple physical contact between the electrode and the molecule (molecule just laying over electrode) does not guarantee good electrical contact. It has long been recognized that to make good electrical contact between a molecule and an electrode, a chemical bond is required. This is usually done with sulfur or selenium bound to gold, platinum or silver[53], or by reaction between carboxylic acid groups at the end of carbon nanotube and DNA modified with amino groups[54–56].

DNA structure. The length of the molecule and its base sequence might be very important. A non-periodic sequence will lead to disorder along the one-dimensional molecule. Homogeneous sequences like poly(dA)-poly(dT), poly(dC)-poly(dG) should provide the best conditions for the π orbitals overlap. The character of the measured sample (e.g., rope vs single molecule) can also interfere with electrical properties.

Environment. Water and ions have a large influence on the secondary structure of dsDNA, and thus on its conductivity (see ref. [55] and the paper **I.I.** of this thesis) . For example from 5 to 10 water molecules per base pair are needed for A-DNA structure, while in conditions with more than 13 water molecules per base pair the B structure is preferred. Depending on the pH of the buffer solution in which the molecule is kept, it can have a different charge due to dissociation of the phosphate groups. Thus, the counterion concentration around DNA can also vary, and it is known that counterions induce nonzero force on electrons inside the molecule, thus interfering with electrical properties. Additionally, the conformation and thus the electrical conductivity depends on whether a molecule is free hanging or laying on the surface, and also on what kind of surface is used (mica, glass or some specially treated surfaces)[57].

Preparation and detection protocols. For example, the drying of DNA via flowing N_2 gas, which is usually done before measurements, tends to provide two or three molecules of water per nucleotide[58], thus suggesting that molecules are completely deformed after drying. Detection of single molecules by scanning probe microscopies or electron microscopies can "dope" DNA and change its electrical properties.

It became evident that it is extremely difficult to make clearly reproducible and easily interpreted experiments on the single molecule level. After more than two decades of research at least one conclusions can be made; although DNA is a very promising material for nanofabrication, it does not have high enough conductivity (at least highly conductive forms of DNA are not observed up to date) to serve as a building block for nanoelectronics as such. Still, the mechanism of charge transport/transfer in DNA is an important fundamental question.

1.4 Dielectrophoresis

Dielectrophoresis (DEP) is a phenomenon of the translational motion of matter caused by polarization effect in a non-uniform electric field[59,60]. The result of the electric field gradient is a force on any polarizable object, charged or neutral. The principle of DEP is illustrated schematically in Fig. 1.6. Surface charges are induced on the polarizable object in the electric field, positive on one side of the object and negative (of the same magnitude) on the other. There is a Coulomb interaction between induced surface charges and the electric field. In a uniform field, the net force due to the Coulomb interaction is zero, as shown in Fig. 1.6a). However, in a non-uniform field, as shown in Fig. 1.6b), the electric field density is higher on the right side of the object, therefore, there is a net force acting on the object in the direction of the higher field strength. In this simplified explanation of the DEP force, the effect of a surrounding medium was neglected. In the general case the polarization

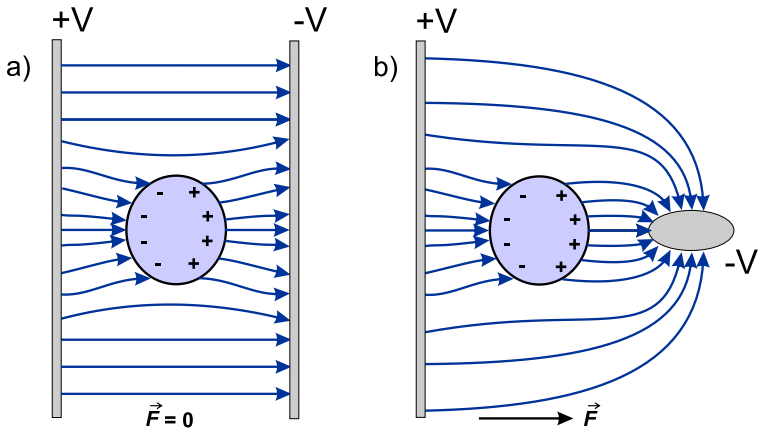

FIGURE 1.6 Schematic picture of dielectrophoresis.

of the medium should also be considered. There are two classes of DEP: positive and negative. In positive DEP, the particle, due to having higher polarizability than the surrounding medium, is pushed toward the region of higher electric field. If the suspended particle has a polarizability smaller than the surrounding medium, the particle is pushed toward the region of weaker electric field, and such phenomenon is called negative dielectrophoresis.

Several theoretical methods have been developed to describe the total dielectrophoretic force on a particle. The effective moment method[61,62] is commonly used, because it provides quite a simple analytical solution while maintaining a good physical insight to the behavior of the system. In this method the particle and the surrounding medium are considered to behave as an effective dipole with induced dipole moment $\overrightarrow{p}$, which is proportional to the electric field $\overrightarrow{E}$, i.e.,

$$\overrightarrow{p} = \alpha \overrightarrow{E}. \tag{1.1}$$

The constant of proportionality α is the polarizability of the object and depends on the geometry of the system and electrical properties of both the particle and the surrounding medium. The polarizability of a particle of volume V with a permittivity ε_p is

$$\alpha = V\varepsilon_p \mathrm{Re}[K], \tag{1.2}$$

where Re denotes real part, and K is the so-called Clausius-Mossotti factor, which depends on both the particle and the medium and is given by[63]

$$K = \frac{\varepsilon_p^* - \varepsilon_m^*}{\varepsilon_m^* + A(\varepsilon_p^* - \varepsilon_m^*)}. \tag{1.3}$$

Here A is a geometrical factor that varies from zero to one: $A = 1/3$ for a sphere,

$A = 1$ for a shot rod; ε_p^* and ε_m^* are complex permittivities of the particle and the medium, described as[64]

$$\varepsilon_p^* = \varepsilon_p - i\frac{\sigma_p}{\omega} \tag{1.4}$$

$$\varepsilon_m^* = \varepsilon_m - i\frac{\sigma_m}{\omega}. \tag{1.5}$$

In these equations, ω is the angular frequency of the applied field, ε_p and ε_p are the real part of permittivities, and σ_p and σ_m are the conductivities of the particle and the medium respectively.

In the presence of a non-uniform electric field the force on the particle is given by

$$\overrightarrow{F} = (\overrightarrow{p} \cdot \overrightarrow{\nabla})\overrightarrow{E} = \frac{\alpha}{2}\overrightarrow{\nabla}(E^2). \tag{1.6}$$

This electrical force is termed as the dielectrophoretic force. For an isotropic homogenous spherical particle with radius R and dielectric constant ε_p , the time-averaged dielectrophoretic force is

$$\overrightarrow{F} = 2\pi\varepsilon_m R^3 \mathrm{Re}[K]\overrightarrow{\nabla}E_{rms}^2, \tag{1.7}$$

where E_{rms} is the root-mean-square value of the electric field (assuming a sinusoidal time dependence)[60,61].

The Clausius-Mossotti factor is a frequency dependent variable. Its real part can vary between -0.5 and +1. When $\mathrm{Re}[K] > 0$, the particle experiences positive DEP, likewise, when $\mathrm{Re}[K] < 0$, the particle experiences negative DEP. The imaginary part varies between -0.5 and 0, and it is an important factor for the so-called traveling-wave DEP[65]. The schematic plot of the Clausius-Mossotti factor's frequency dependence is shown in Fig. 1.7. Several notifications about equation 1.7 should be made.

i) By changing the electric field frequency, the Clausius-Mossotti factor can experience a transition from a positive value to a negative value, which causes the DEP force on the particle to change its direction accordingly. This property of the Clausius-Mossotti factor of the particle under a specified suspending medium can be utilized for manipulation of particles.

ii) The DEP force is proportional to the volume of the particle, V, and this fact limits the application of DEP for the manipulation of nano-sized particles. In addition, the equation is derived classically, all permittivities and conductivities are assumed to be the bulk values. For nanoparticles and macromolecules a significant fraction of the atoms of the "particle" reside on the surface. Moreover, the particles can be charged and a so-called counter-ion cloud is formed around the charged particle, which can have a significant effect on DEP. Therefore, the application of this model to single molecules may not be quantitatively valid.

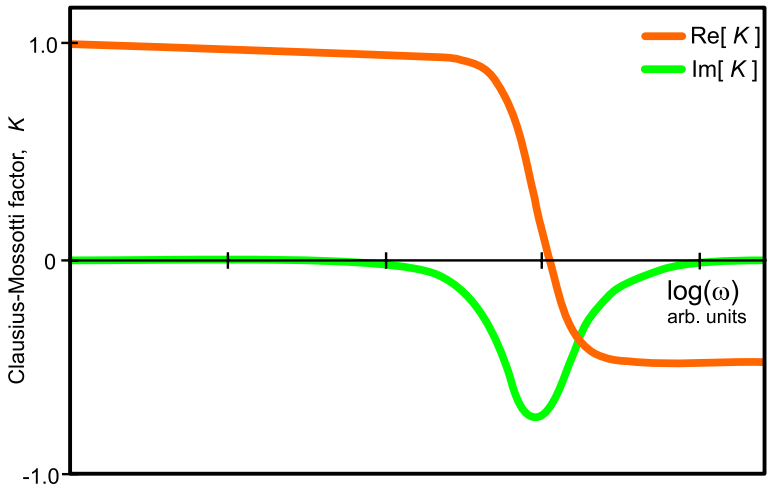

FIGURE 1.7 Frequency dependence of the Clausius-Mossotti factor for a spherical particle.

iii) The equation is valid for both DC and AC electric fields. Furthermore, the direction of the DEP force does not depend on the direction of the electric field. It is the field gradient that determines the direction of the force on the particle, not the field itself. For the AC field: the particle experiences time-varying force, but the direction of the time-varying force is always the same, even though the direction the electric field vector is changing in time. In most cases one needs to consider only time-averaged values of the field, as it is done in Equation (1.7).

iv) Sometimes the dipole approximation is not accurate enough and higher order multipoles have to be considered. The general solution has been obtained by Jones and Washizu[66,67].

Another frequently used method to describe DEP is the so-called Maxwell stress tensor method[68]. It requires a rigorous surface integration of the stress tensor over the particle, and the analytical solution is limited to the case of a homogeneous spherical particle and small field gradients. However, this method is preferred for numerical calculations, and has been implemented in some commercial finite-element software.

For the DEP force to be effective, it must overcome the Brownian motion, which can be treated as a random force whose maximum value is given roughly by[60]

$$F_{thermal} \approx k_B T / \sqrt[3]{V}, \tag{1.8}$$

where k_B is the Boltzmann constant, T is the temperature, and V is the volume of the particle. This sets rather strict requirements on the minimum particle size that can be manipulated, and very large electric field gradients are needed to manipu-

late nano-sized objects. Microfabricated electrodes are used to generate the required field gradients.

There are several other forces acting on the particle, which originate from the motion of the solvent under the high electric field[69]. The Joule heating can cause an electrothermal force. Also, the geometry of the electrodes used to generate DEP forces produces a tangential electric field at the electrode-electrolyte double layer inducing steady motion of the liquid, a flow termed as electro-osmosis. Each of these forces might limit the manipulation of particles with DEP.

So far the phenomenon of dielectrophoresis was used to manipulate cells[70,71], latex beads of different sizes[72,73], viruses[74], proteins[75], carbon nanotubes[76], and DNA[77] (the papers **I.I.-I.V.** of this thesis). There are several good reviews on the application of dielectrophoresis[78,79]. In addition there is a detailed overview of DNA DEP trapping in PhD thesis of Sampo Tuukkanen[80].

2. Dielectrophoretic trapping and polarizability of DNA molecules

2.1 Dielectrophoresis of double stranded DNA

2.1.1 DEP trapping with lithographically fabricated electrodes

The first studies of DNA dielectrophoretic trapping in this thesis were done in connection with DNA electrical measurements. A key experimental problem in measuring the conductance of DNA lies in the attachment of a single molecule or a DNA bundle to the electrodes. DEP is a very promising technique that allows reproducible fabrication of single molecule devices. For dielectrophoretic trapping of single double-stranded DNA molecules narrow finger-tip type gold electrodes were used (width ∼100 nm and gap ∼100 nm). Double-stranded 414 bp (∼140 nm) long DNA molecules with thiol groups in both ends were fabricated and diluted in HEPES buffer. Fabrication of electrodes and preparation of DNA is described in detail in Appendix A.1. Prior to DEP experiments, samples were cleaned with short

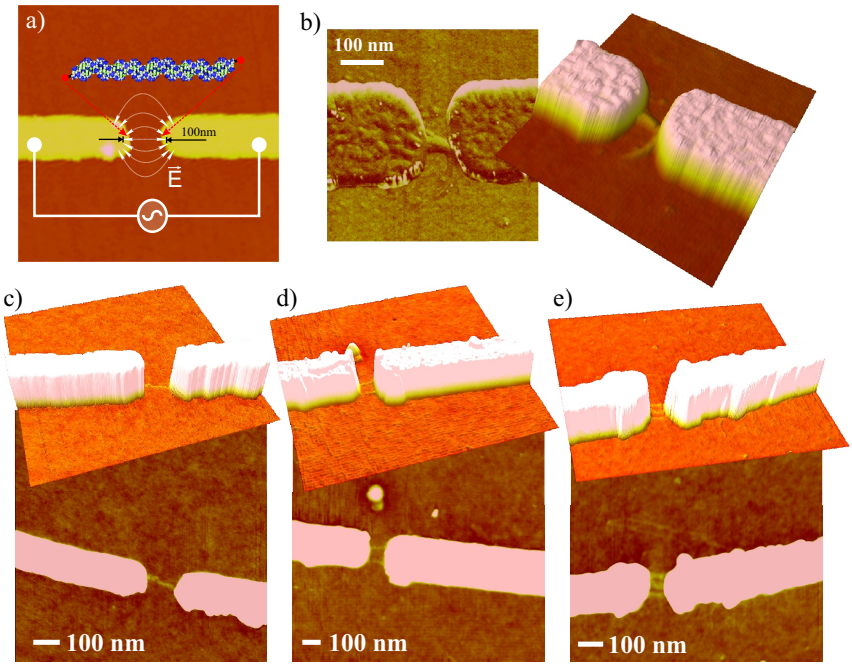

FIGURE 2.1 a) Schematic presentation of the experimental set-up for attachment of DNA to nanoelectrodes. Note that DNA is not in scale with the gap. DNA bundle b) and individual DNA molecules c)-e) trapped between electrodes using dielectrophoresis. Adapted with permission from the paper **I.I.** of this thesis.

flash of oxygen plasma in order to remove possible organic contamination from the surface of the sample and the electrodes. Trapping was done by incubating a few microliter drop of 1 nM DNA solution onto the substrate containing the electrodes and keeping the sample in a moist chamber to prevent the drop from drying while applying AC voltage to the electrodes. The voltage was applied for ∼20 min. After DEP, the drop was rinsed with 6.5 mM Hepes (pH 7.0 with NaOH) buffer and water and nitrogen dried. The principle of the attachment of DNA to electrodes is schematically shown in Fig. 2.1a). The electrode samples were imaged with AFM before and after the DEP trapping. More than hundred DEP experiments were done in order to find the optimal parameters for DNA trapping. It was found that for successful trapping, electrical fields with a frequency of ∼1 MHz should be used with more than 3 V_{pp} peak-to-peak amplitude (field strength $\sim 10^7$ V/m). It was also concluded that a reducing agent (in this case $NaHB_4$ (Sodium Borohydride)) has to be used to cleave the S-S (sulphur-sulphur) bonds between separate thiol modified DNA molecules in order to trap individual DNA molecules. Without the reducing agent only big agglomerates or bundles of DNA molecules were found in or near the gap. One can distinguish between bundles and single DNA molecules by the analysis of AFM images. The typical height of the DNA molecules on SiO_2 substrate is between 0.5 nm and 1.5 nm[57,81,82]. Objects with height of more than 2 nm were interpreted to be DNA bundles. The yield of trapping of individual molecules was as high as 50%. An example of DEP trapping of DNA bundles and individual DNA molecules is given on Fig. 2.1b)-e). To distinguish the real effect of DEP from the random adhesion of DNA or other particles to the substrate, reference electrodes were used. They were situated in the vicinity (∼50 μm away) of the electrodes used to generate alternating field for DEP, and were identical to them, except that the guiding voltage was not applied to the reference electrodes. The incubated drop of the DNA solution covered both trapping and reference electrodes at the same time. The attachment of individual DNA or DNA bundles to the reference electrodes was never observed. It should be stressed here that DNA molecules in solutions are coiled, and as can be seen from Fig. 2.1c)-e) the effect of DEP is not only trapping but also stretching of molecules. The successful attachment of single molecules between electrodes is the result of both trapping and stretching.

2.1.2 DEP trapping with CNT electrodes

As was discussed in Chapter. 1.4, for the effective trapping the DEP force should overcome the Brownian motion which is inversely proportional to $\sqrt[3]{V}$, where V is the volume of object to be trapped. Thus for the trapping of smaller objects higher DEP forces are needed. As can be seen from Eq. 1.7 the DEP force can be increased either by increasing the electric field or the electric field gradient. There are experimental limitations on how much the electrical field can be increased, too high fields

can induce harmful fluid flows (electrothermal and electroosmotic), heating and even electrolysis in the system. One can increase the electric field gradient by fabricating narrower electrodes. Nowadays, lithographically fabricated electrodes have a minimum line width in order of tens of nanometers. These structures do not always offer large enough electric field gradients to overcome Brownian motion for less than ∼10 nm sized objects, when sufficiently low voltages are used. Since a single-walled carbon nanotube (SWCNT) is only ∼1 nm in diameter, and a few nanometers in the case of multiwalled carbon nanotubes (MWCNTs), CNTs can be used as electrodes to produce very high electric field gradients[78]. In order to test the efficiency of CNT as a DEP electrode and compare it with the lithographically fabricated electrodes, samples that had one CNT electrode and one fingertip metal electrode were fabricated. DNA molecules of two different lengths (145 bp or 50 nm and 1065 bp or 360 nm) were used as objects for trapping. Detailed description of the CNT electrode fabrication and DNA preparation is given in Appendix A.2. The DNA was labeled with a dsDNA specific fluorescent label PicoGreen (Molecular Probes) and confocal microscopy was used to observe the DEP trapping. A schematic view of the experimental setup and an example of CNT electrode is shown on Fig. 2.2. Dielec-

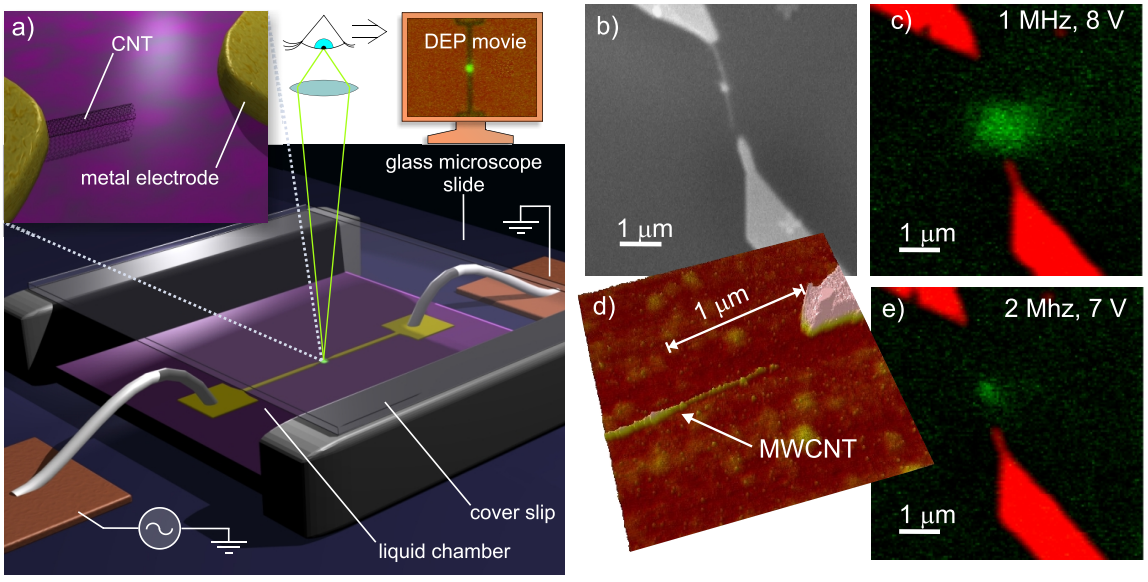

FIGURE 2.2 a) A schematic view of the experimental setup used in the DEP experiments under the confocal microscope. The DNA solution is in the moisture chamber between the substrate and the cover slip. The CNT electrode structure is presented in the close-up image. Repeated confocal microscope images are captured to obtain time-resolved information about the DEP process [Schematic 3D images by Tommi Hakala]. b) SEM and d) AFM images of the MWCNT electrode sample before the confocal microscope experiment. c) and e) show the fluorescent signal from trapped DNA (1065 bp) with a certain frequency and voltage used. Adapted with permission from the paper **I.II.** of this thesis.

trophoresis experiments under the confocal microscope (Zeiss Axiovert LSM510, Zeiss "Fluar" 40x/1.3 Oil objective) were performed by (fluorescent) imaging of a 10x10 μm^2 square area around the gap while applying sinusoidal AC voltage to the electrodes. Data were collected simultaneously from two channels: the fluorescence channel (equipped with 505 nm high band pass filter), which corresponded to the amount of DNA, and the reflection channel (equipped with 475-525 nm band pass filter), which showed the location of the electrodes. Time resolved data (DEP movie) was obtained by capturing two 128x128 pixel frames per second. An argon laser (488 nm) with power of 0.45 mW was used for imaging. It was tested in advance that the used laser powers did not induce bleaching of the PicoGreen dye. In the beginning of a DEP movie, the voltage was kept off for 10 s after which the sinusoidal AC signal was turned on (to a certain starting voltage value). The voltage was raised in 0.2 V_{pp} (0.07 V_{rms}) steps after each 20 s until the final voltage value was reached. Then the voltage was turned off but the data collection was continued for ~20 s to observe the DNA diffusion from the gap. For the analysis, the mean fluorescence intensity

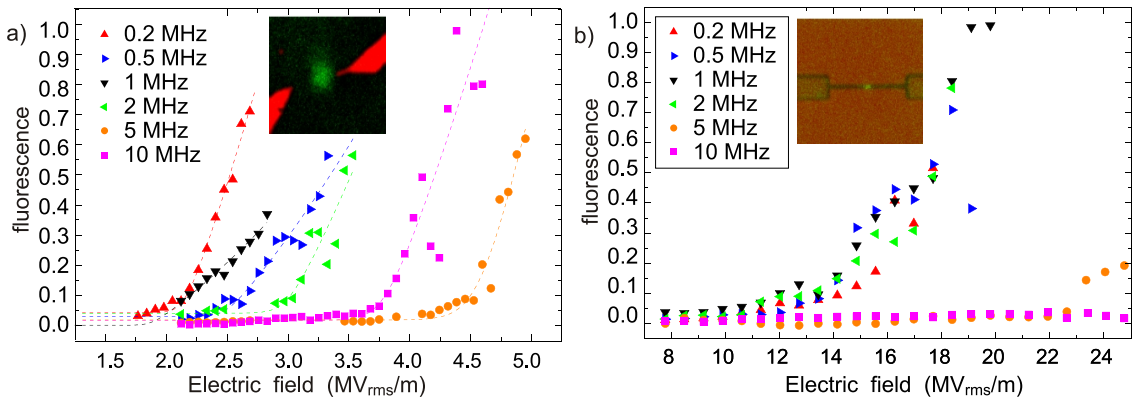

FIGURE 2.3 Trapping efficiency of CNT electrode vs finger-tip metal electrode for 1065 bp dsDNA. The normalized fluorescence a) in the end of the of CNT with electrode separation 1 μm (Fig. 2.2) and b) in the 100 nm gap of finger-tip metal electrodes as a function of the average electric field in the gap. Dotted lines in a) are fits to the data using the function $I = I_o + A(V^b + V_{min}^b)^{2/b}$ (see text). Adapted with permission from the paper **I.II.** of this thesis.

inside the circle shaped (diameter of 1.6 μm) area in the gap between the finger-tip electrodes (or at the end of CNT) was determined and subtracted by the mean intensity of the background fluorescence. The obtained value is proportional to the amount of trapped DNA. With this approach one can obtain quantitative information about the minimum voltage V_{min} for which the trapping begins for different DEP frequencies as well as qualitative information about the amount of trapped DNA molecules with different DEP voltages. Figure 2.3 shows the comparison of the trapping efficiency of the CNT electrode and the finger-tip metal electrode. By comparing the field strength one can clearly see that the CNT is more efficient elec-

trode for DEP trapping than the lithographically fabricated. The trapping efficiency was determined as the minimum voltage V_{min}, and the corresponding field strength, for which the trapping begins.

2.2 Polarizability of DNA molecules

Nowadays, separation of DNA molecules is mostly based on electrophoresis, i.e., electric field induced migration of the charged molecules in the electrolyte. Although proposed more than 15 years ago[83], it has been only recently experimentally demonstrated that dielectrophoresis can be used as an alternative separation technique[84]. The utilization of DEP offers the prospect of integration of the separation process into microfluidic devices with an obvious application in lab-on-chip systems. In order to utilize full potential of DEP as the separation technique for DNA molecules the qualitative information about DNA polarizability and its dependence on the experimental factors is needed. The high efficiency of the trapping in the case of the

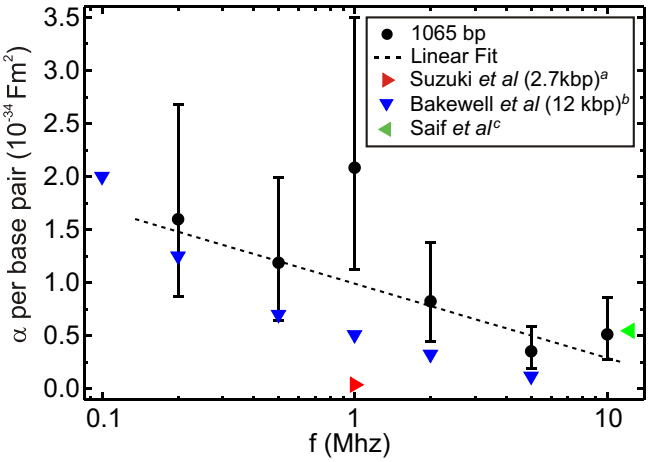

FIGURE 2.4 Polarizability per bp for 1065 bp DNA calculated from the fluorescence data. The error bar originates from the uncertainty of the trap radius. For comparison, values of DNA polarizability are taken from [85][a] [86][c] [87][b]. Adapted with permission from the paper **I.II.** of this thesis.

CNT electrode made it possible to do some estimations of DNA polarizability, which was calculated in the following way. The DEP trapping energy for a polarizable particle in an applied electric field $\overline{E}(\overline{r})$ is $U_{DEP}(\overline{r},\omega) = -\frac{1}{2}\alpha(\omega)\cdot[E(\overline{r})]^2$, where α is the frequency-dependent polarizability. Besides DEP, the particle also experiences the Brownian motion, which is associated with the thermal energy $U_{Th} = \frac{3}{2}k_BT$. The DEP trap collects DNA when $U_{DEP} \geq -U_{Th}$. First, the minimum voltage at which trapping began, V_{min}, was determined by fitting the fluorescent intensity to the function $I = I_o + A(V^b + V_{min}^b)^{2/b}$ which produces the V^2 dependence after the

the voltage V_{min} had been reached. Next, the finite element simulations by Comsole

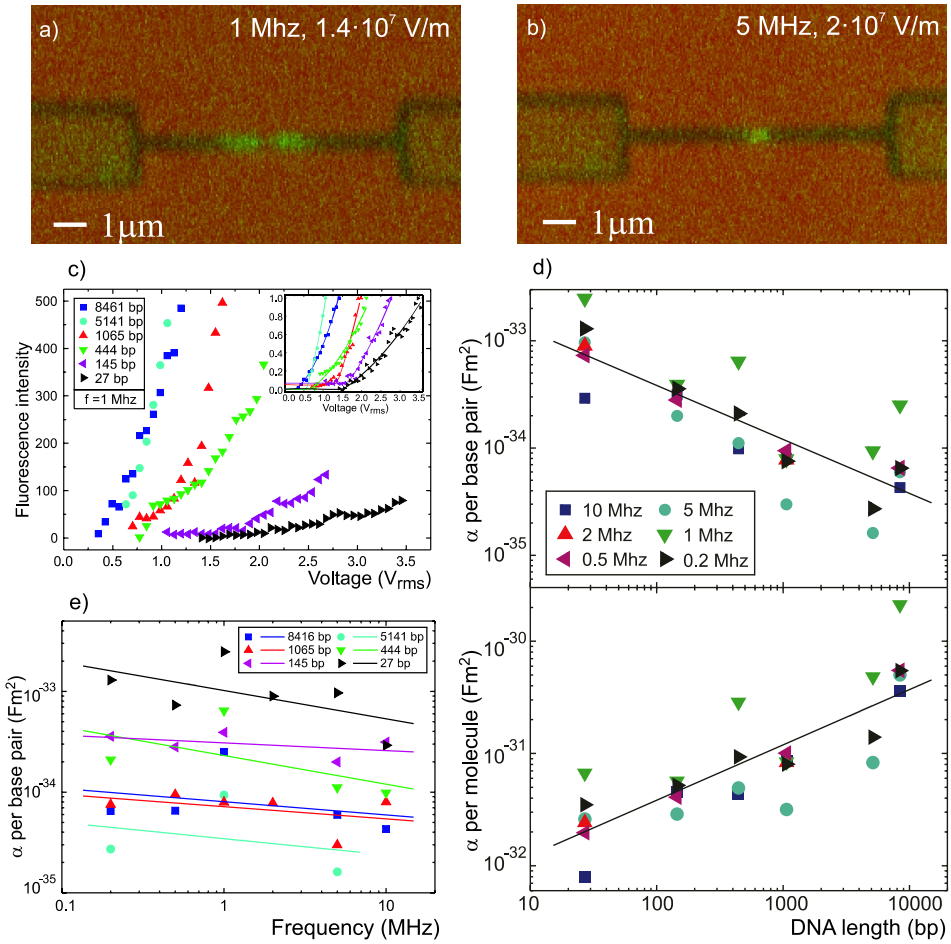

FIGURE 2.5 Confocal microscope images of trapped DNA with applied signal of frequency a) 1 MHz and b) 5 MHz. With higher frequency the DNA spot is smaller because of the decreased electrophoretic effects. c) The trapped amounts (the fluorescence in arbitrary units) of different size DNA fragments as a function of the trapping voltage using 1 MHz frequency. In the inset, the normalized fluorescence curves and fits to the function $I = I_o + A(V^b + V_{min}^b)^{2/b}$ are represented. d) Experimentally obtained polarizabilities (per molecule and per base pair) plotted as a function of the length of the DNA fragment with different frequencies. e) Experimentally obtained polarizabilities (per base pair) for the different size DNA fragments plotted as a function of frequency. Figures c)-e) are adapted with permission from the paper **I.III.** of this thesis.

Multiphysics software were performed to find out the electric field strength E_{min} at the edge of the trap (fluorescence spot) from the obtained V_{min} value. The typical radius for the observable fluorescence spot was $r = 0.5 \pm 0.1\mu$m. Thus, the E_{min} was read from the simulations at the distance r from the CNT end, perpendicular to it, in the plane parallel to the substrate, 0.2 nm above the CNT. The polarizability

was obtained from the condition $U_{DEPmin} = -U_{Th}$ as $\alpha = 3k_BT/E^2_{min}$. Normalized polarizability (polarizability per bp) as a function of frequency is shown on Fig. 2.4 together with values from literature[85–87] for various size DNA molecules. The DNA polarizability strongly depends on the frequency used and buffer conditions (e.g., ionic strength), as well as on the total length of molecule. Thus, it is not surprising that there is some discrepancy in polarizability values obtained from different experiments in Fig. 2.4.

Although the CNT electrodes are very effective for DEP trapping, it is experimentally very challenging to fabricate such electrodes in a reproducible way. Thus, in order to study DNA polarizability and its dependence on DNA length and frequency systematically, metal finger-tip electrodes were used with width of ∼100 nm and ∼100 nm separation between them (see Appendix A.1). Double-stranded DNA fragments with varying length (27-8461 bp) were fabricated by three different methods: annealing of the synthetic oligos, PCR, and restriction enzyme digestion of the plasmids multiplied in bacteria. For details of DNA preparation see Appendix A.3. Imaging under the confocal microscope was performed as described above for the carbon nanotube samples. An example of confocal microscope images of trapped DNA for two different sets of DEP parameters in the case of finger-tip electrodes is given in Fig. 2.5a) and b). The polarizability was calculated following the same steps as described above, i.e., first the V_{min} was determined experimentally, then the E_{min} was obtained from the simulations by Comsole Muliphysics software, and finally polarizability α was calculated from the condition $U_{DEPmin} = -U_{Th}$. Figures 2.5c)-e) show the dependence of the fluorescence intensity (amount of trapped DNA) in the gap of the electrodes on the applied voltage as well as the dependence of the polarizability on the frequency and the length of DNA. The polarizability values obtained from the confocal studies correspond to the range of the values found from the literature, which vary from $\sim 10^{-36}$ to $\sim 10^{-34} Fm^2/bp$ (see ref. [84] and references therein). As one can see, the polarizability per bp is larger for the shorter DNA fragments. This can be explained by the fact that the polarization of DNA is mainly caused by the counter-ion cloud, which itself has a certain minimum thickness.

2.3 Immobilization of the trapped DNA molecules on the electrodes

Another important information that can be obtained from the confocal microscope studies is the efficiency of immobilization of the trapped molecules on the electrodes. In order to attach DNA to a metal surface or a carbon nanotube, oligonucleotides modified with a thiol or an amino group are usually used. The immobilization of DNA on the gold electrodes through sulphur-gold bonding was stud-

ied for two different modifications (hexanethiol (C6) and dithiol-phosphoramidite (DTPA)). Two types of DNA molecules were prepared, 414 bp C6-DNA and 415 bp DTPA-DNA (for preparation details see Appendix A.3). The non-specific binding of the unmodified 444 bp DNA was used to compare the immobilization of the modified DNA molecules. The quantitative analysis was done by comparing the amount of the fluorescence that remained in the gap region after the trapping voltage was turned off. This indicates the efficiency of the attachment to the electrodes. The molecules without linkers diffused away from the trap very soon after the trapping voltage was turned off, whereas in the case of the C6- and DTPA-modified DNA a noticeable amount of the molecules remained on the gap (see Fig. 2.6).

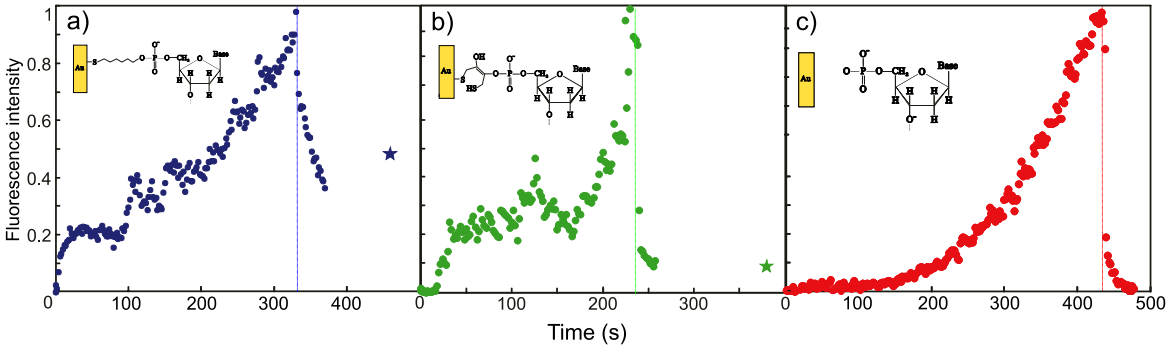

FIGURE 2.6 DEP trapping and immobilization of a) the C6-DNA, b) the DTPA-DNA and c) the unmodified 444 bp DNA to the fingertip electrodes using a 5 MHz frequency. In a), b) and c), the circles describe the data points obtained from the DEP movie and the stars represent the "remained fluorescence" measured separately after the laser excitation had been turned off for a certain time. The dashed lines represent the times when the voltage was turned off. Schematic views of the binding of linkers are shown in insets. Adapted from the paper **I.III.** of this thesis.

Somewhat surprisingly, hexanethiol modified DNA were more efficiently immobilized on the electrodes than those modified with DTPA. Naïvely, one can expect DTPA to be more efficient linker, since is has two sulfur atoms in the ring, which could allow double bonding to the electrodes. Density functional theory (DFT) calculations were used to get more insight into the binding process. The gold electrode was modelled by a tetrahedral 20 gold atom cluster. The calculations showed that hexanethiol can bind to the gold surface with a binding energy of 1.8 eV. On the other hand, DTPA linker did not show any binding affinity if the S-S bond was left intact. Partial hydration of the S-S bond resulted in binding of the linker with a binding energy of 1.2 eV. It has been recently experimentally demonstrated, that lipoic acid is much more efficient linker than hexanethiol for DNA attachment to gold nanoparticles[44]. This is in a way unexpected, since the structure of the lipoic acid is quite similar to the structure of DTPA.

3. Measurements of electrical properties of DNA molecules

With a reproducible method of trapping DNA molecules/bundles and their attachment between metal electrodes, it was possible to make systematic studies of DNA conductivity. DNA molecules were attached between gold electrodes by dielectrophoresis as described in Sec. 2.1. Samples were imaged with AFM before and after DEP trapping to ensure the presence of DNA between the electrodes. Conductivity measurements were performed inside an electrically shielded room, equipped with highly filtered feed-throughs for measurement lines. Current-voltage (I-V) characteristics of samples were obtained by measuring a number of individual DC current-voltage points. A tunable DC voltage bias was obtained from the battery powered DAC (digital-to-analog converter) circuit, which was digitally controlled through the optical lines. A low-pass RC filter (R=100 Ω and C=47 μF) was used to cut high frequency transients from the DC bias voltage. The DC bias voltage was changed from minimum to maximum by taking finite steps and letting the sample to stabilize for 3-5 s before recording the current. The maximum voltage varied from 0.1 V to 1 V. The most reliable results were obtained using the 0.1 V range which was small enough to prevent undesired effects, e.g., electrolysis and collecting contaminating particles form the air. Measurements were done at room temperature ($\sim$23 ^{o}C) both with relative air humidity of $\sim$30 $\%$ ('dry' environment) and of 80-90$\%$ ('moist' environment). Measurements in humid air were performed by placing the sample inside a moist chamber during the I-V measurements. The relative humidity and temperature were measured using Honeywell Humidity sensor (HIH-3602-A).

In the dry environment, all DNA samples showed insulating behavior: I-V curves were linear at small voltages with the resistance of tens of TΩ. This is in agreement with observations by several other groups[81,88,89]. Drying of the sample after DEP with nitrogen flow leads to dramatic dehydration of DNA suggesting that DNA is significantly deformed from its natural state. After measurements in the dry environment, the samples were placed inside a moist chamber and I-V characteristics were measured simultaneously with the relative humidity level. In the moist conditions, some samples behaved in a similar way to reference samples (which contained no DNA), indicating that there were either no DNA properly attached to the electrodes or DNA was not conducting for some reason, such as being severely deformed. However, several samples showed clear enhancement of conductivity in the moist conditions. One of the samples that showed increased conductivity in humid air was the one with three DNAs attached between the electrodes, shown in Fig. 2.1e). After half an hour in the moist atmosphere, the resistance of the sample

dropped to ∼250 MΩ. After that, the resistance slowly increased during the measurements, being 700 MΩ after three hours. This deterioration of the conductivity during the measurements could be related to disturbance of the DNA structure caused by gathering of contaminants from the moist air, which was observed in many samples by AFM imaging after measurement. Two sets of I-V curves measured at moist conditions are shown in Fig. 3.1a), together with the I-V characteristics for dry conditions, corresponding to the resistance of about 10 TΩ. After

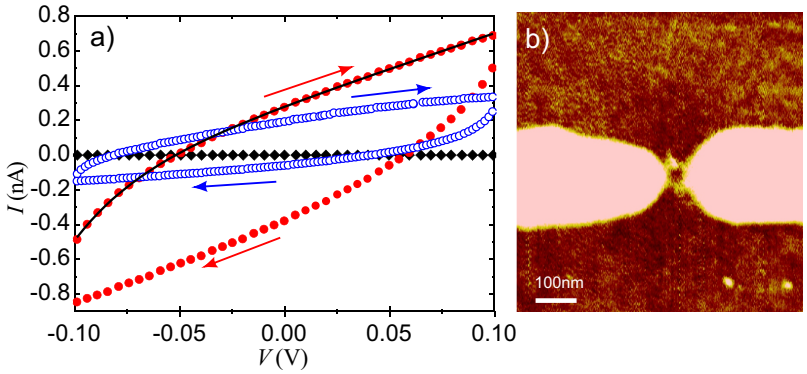

FIGURE 3.1 a) I-V characteristics of three DNAs attached between the electrodes. Black diamonds are measured in the dry environment (R ∼10 TΩ) while red circles are measured after 30 min in moist conditions, corresponding to the minimum resistance of the sample R ∼250 MΩ. Blue open circles are measured in moist conditions after three hours. By that time the resistance had increased to ∼700 MΩ. The hysteretic behavior is due to enhanced charging effects in moisture, as shown by fitting the data to the classical theory to compensate the (de)charging effects (the solid curve). b) The AFM height image of the same sample taken right after conductivity measurements. Clearly, at least two DNA molecules are preserved. Adapted with permission from the paper **I.I.** of this thesis.

measurements in moisture, the sample was dried with nitrogen and the resistance increased back to the original dry value of tens of TΩ. The sample was imaged with AFM right after these measurements confirming that at least two DNAs were still properly attached (see Fig. 3.1b)). The scan noise in the AFM image is probably due to contaminants collected from the moist air during the measurements. The increase of conductivity in the moist conditions, i.e., resistance dropping to hundreds of MΩ in moist conditions, was observed in several different samples with a single or a few DNA. Such behavior was never observed in reference samples, for which control experiments were done using exactly the same procedure for the DEP and subsequent transport measurements, but using a buffer solution without DNA. Reference samples also showed clear difference between the dry and the moist environment measurements. However, in moist conditions, the minimum resistance observed in the reference experiments was ∼7 GΩ, and the resistance in dry environment was always ∼10 TΩ.

The hysteretic behavior observed in the measurements of the I-V characteristics can be explained by currents due to charging of the total capacitance of the sample formed by the capacitance of the electrodes and parasitic stray capacitances. In the case of step-like DC bias voltage, one easily obtains (see Appendix A.5) for the measured current

$$I = \frac{V_n}{R} + I_0 \alpha \frac{1-\alpha^n}{1-\alpha} \tag{3.1}$$

where n means the nth I-V point measured and V_n is the corresponding bias voltage. Other parameters are: R the resistance of the sample, I_0 the maximum charging current at bias voltage transients (depends on the resistances of the measurement instruments) and α=$e^{-\tau_m/\tau}$ the exponential of the ratio between the stabilization time, τ_m, and the time constant of charging, τ. Fig. 3.1a) shows this formula fitted to the data measured from the sample with 3 DNA molecules (Fig. 2.1e)). The obtained time constant, τ , was of the order of 30 s in that case. The origin of such big time constant is not totally clear.

Though the effect of humidity to the conductivity of individual DNA molecules and DNA bundles was evident, the nature of the charge transport or transfer cannot be completely determined based on these experiments. One of the possibilities is enhanced electron transport/transfer caused by humidity induced conformational changes in DNA structure. As it was already mentioned above, the direct electronic conductivity, by means of overlapping π-orbitals of the base pairs along the molecular axis, is likely to be sensitive to the helical conformation of DNA (note that the contributions of protons or counterions might also be affected by the deformations). The deformations of the structure can be due to, e.g., ambient conditions or interactions with the substrate surface[57]. It has been observed that the humidity of air affects the structure of a single double-stranded DNA on graphite so that it appears in its natural B-DNA form at moist conditions, but collapses to a form resembling A-DNA when dried to the surface[90]. Nowadays, it is quite generally accepted that DNA conductivity depends on humidity, recently several experimental papers were published on the topic[55,91,92]. Also in several theoretical papers the effect of water and conformational changes on DNA electronic structure was considered[93,94]. Again results are somewhat inconsistent, for example Kleine-Ostmann and colleagues claim that increase of DNA conductivity in high humidity environments is due to water molecules accumulated at the DNA phosphate backbone and it is not the intrinsic DNA conductivity[92]. On the other hand, Vedala *et al.* made a more careful study on the influence of environmental factors (buffers, humidity, temperature) on DNA conductivity[55] and came to the conclusion that buffers of high conductivity significantly affected the intrinsic conductivity measurement, and the measured signal originated mostly from the salts residues. However, the authors also observed a measurable current through DNA molecules in the case of low con-

ductivity buffers, and the signal was attributed to the intrinsic DNA conductivity. As for the theory work, Song *et al.*[93] claimed that the increase in the conductivity in the experiments described above cannot be attributed simply to the conformational changes of DNA. However, in ref. [94] Berashevich and Chakraborty showed that besides conformational changes (from A to B form) there is another effect that can influence the conductivity properties, namely, the interaction of the nucleobases with water molecules leads to breaking of some of the π bonds and appearance of unbound π electrons. These unbound electrons contribute significantly to the charge transfer at room temperature by up to 10^3 times. Definitely more experimental and theoretical work should be done in order to understand the influence of environmental factors on DNA electrical properties. Some insight into the nature of charge transport/transfer could be also obtained from the AC measurements[95,96].

4. DNA origami as a nanobreadboard

As was described above, DNA origami has a great potential for the nanoscale assembly of materials. This is due to the fact that each of the short oligos used to fold the origami structure is unique in its sequence and position and can be modified to serve as a binding site. Thus, one can consider the origami structure as an array of pixels or a "nanobreadboard" (see Fig.4.1), a nano-scale template to which variety of (functional) materials can be attached, for example semiconducting quantum dots can serve as light emitters, metal particles as capacitors, carbon nanotubes as interconnects or transistors etc. Besides possible applications in nanoeletronics, origami templates can also be used to assemble multiprotein arrays allowing creation of artificial complex enzyme cascades[97]. To realize the full potential of the "nanobreadboard" idea one has to develop methods for i) controlled on-chip positioning of origami structures which also provide electrical contacts to origami, ii) assembly of multiple materials with high yield and precision with origami as a template. It the following sections I will describe the dielectrophoresis based method

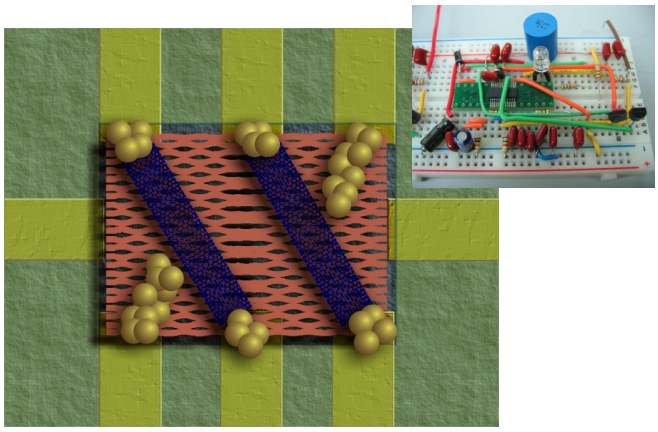

FIGURE 4.1 Schematic picture of DNA origami as a nanobreadboard. Origami structures can be considerers as an array of pixels to which different materials can be attached, or "plugged in" as in breadboard (inset).

for trapping of origami structures between metal nanoelectrodes and present and compare two general approaches for the assembly of materials .

4.1 Connecting DNA origami to the outer world

As was shown above, dielectrophoresis is a very efficient method for nanoscale manipulation of DNA molecules. Thus, it was decided to use DEP as a method for

on-chip positioning of DNA origami structures. It should be noted here that before this work there were no reports on DEP trapping of DNA self-assembled structures. One of the first difficulties that arose in the experiments was due to the fact that self-assembly is usually done in buffers of relatively high ionic strength (conductivity) to reduce the repulsion between negatively charged DNA backbones. On the other hand, DEP trapping should be performed in a buffer with a relatively low conductivity (well below 1 mS/cm)[85]. Thus, before DEP, buffers should be somehow changed. It is possible to overcome this problem by ligation, which is known to increase mechanical and thermal stability of DNA structures[98] and thus allows changing of buffers. Another difficulty is that trapping of DNA origami structures seems to be more sensitive to the experimental conditions (DEP frequency and voltage, buffer conductivity) than single DNA molecules, thus one has to test a wide range of parameters in order to find the optimal that allows trapping of single structures precisely in the middle of the electrodes.

For the trapping, fingertip-type gold electrodes with widths of 20-25 nm and gaps of 70-90 nm were used . Electrodes were fabricated on a SiO_2 substrate using standard electron beam lithography and evaporation of metal (1 nm of Ti followed by 15-20 nm Au) in an ultrahigh vacuum (UHV) chamber (see Fig. 4.2a). For details of the electrodes fabrication see Appendix A.1. Two types of DNA origami structures were used for trapping (see Fig. 4.2b)): a rectangular (71×98 nm^2) structure, and a disk-shaped ($\sim$100 nm in diameter) structure with three holes (the so-called smiley). Detailed information on these kinds of structures can be found on pages 26-28 and 32-35 of Supplementary Note 1 of the reference [30]. The origami structures were fabricated by thermal annealing (from 90 °C to 20 °C, at rate of 1 °C/min, in 0.1 °C steps) of 50 μl solution of 10 nM of single-stranded viral DNA (from the M13mp18 virus) with 10x excess concentration of staple strands. After annealing,

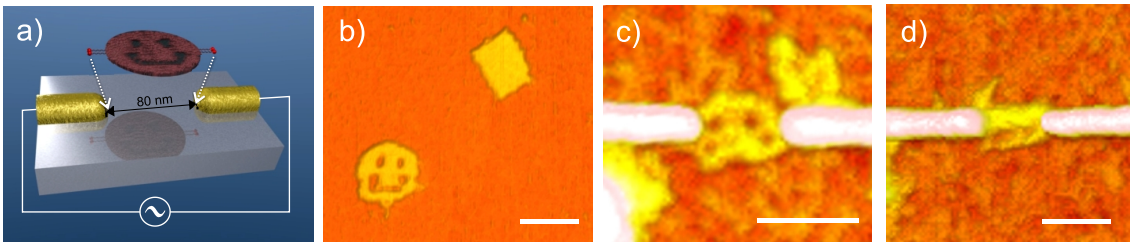

FIGURE 4.2 Trapping of DNA origami structures with dielectrophoresis. a) Schematic view of the origami trapping experiments. b) AFM image of origami structures used for DEP trapping. The image is taken on a MICA surface using tapping mode AFM in liquid. c) AFM image of a single smiley and d) rectangular origami trapped with the optimal DEP parameters (on SiO_2 surface, tapping mode AFM in air). The scale bar is 100 nm. Adapted from the paper **I.IV.** of this thesis.

the origami sample was ligated using T4 DNA ligase. In the final step of origami solution preparation, the 1x TAE Mg^{++} buffer used for origami annealing (1x Tris-

Acetate-EDTA (TAE) with 12.5 mM magnesium acetate, pH ∼8.1, σ ∼3.5 mS/cm) was changed to a Hepes-based buffer of smaller conductivity using spin filtering, which should also wash out T4 DNA ligase and glycerol from the ligation procedure. Two types of buffers were used: (Buffer 1) 6.5 mM Hepes, 2 mM NaOH, 1 mM magnesium acetate (pH ∼7.2, σ ∼300 μS/cm) and (Buffer 2) 6.5 mM Hepes, 2 mM NaOH, 1 mM magnesium chloride (pH ∼7.2, σ ∼590 μS/cm). Final concentration of the origami structures in the solution for the DEP experiments was about 1 nM. The ligation procedure was necessary for the origami structures to be stable in buffers with such a low conductivity (low salt concentration). After the ligation, origami structures were stable at least for a few weeks in the Hepes-based buffers, if kept at room temperature. For details of origami fabrication, see Appendix A.6. Altogether, more than 200 electrodes samples were fabricated to obtain reliable statistics of the trapping process.

DEP experiments were performed by incubating a 10 μL drop of an origami solution onto the surface of the nanoelectrode sample and keeping it in a moist chamber, to prevent the drop from drying, while applying a sinusoidal AC voltage to the electrodes. To find the optimal conditions for trapping, the DEP parameters were varied over a wide range. Frequencies from 1 MHz to 15 MHz, and voltages from 0.6 to 2.4 V_{pp} (peak-to-peak value) were tested. With careful tuning of the DEP parameters, it was possible to trap a single origami structure between the electrodes (see Fig. 4.2c) and d)).

For the whole frequency range DNA origami structures underwent positive DEP (attracted to field maxima rather than minima). However, in order to trap a single structure precisely in the middle of the electrode high frequencies had to be used. The results agree qualitatively with DEP experiments with dsDNA, where DNA was more localized in the trap under higher DEP frequencies (see Fig. 2.5 in the Section 2.2). Below 10 Mhz, origami structures were mostly trapped along the electrodes in the region around the gap, and the yield of origami structures trapped precisely in the gap was very low, below 1 $\%$. However, for the optimal DEP frequency, somewhat above 10 Mhz, the yield became as high as 10$\%$ and clearly fewer origami structures were observed in other places than the gap. An example of the frequency effect on trapping is shown in Fig. 4.3 with rectangular origami structures in Buffer 1. Another parameter which should be optimized for the trapping of single origami structre is the DEP voltage. As was discussed in Chapter. 2, for the DEP trapping of single DNA molecules, it was experimentally observed that for each frequency there is a certain threshold voltage below which no trapping is observed and above which the amount of trapped DNA particles grows rapidly with voltage (see Fig. 2.3 and 2.5c)). This is because the trapping potential caused by the voltage should overcome the Brownian motion, which determines the minimum trapping voltage. Naïvely, one could expect that higher voltages would lead to stronger trapping over a larger area. Indeed, with voltage even slightly above the optimal, the

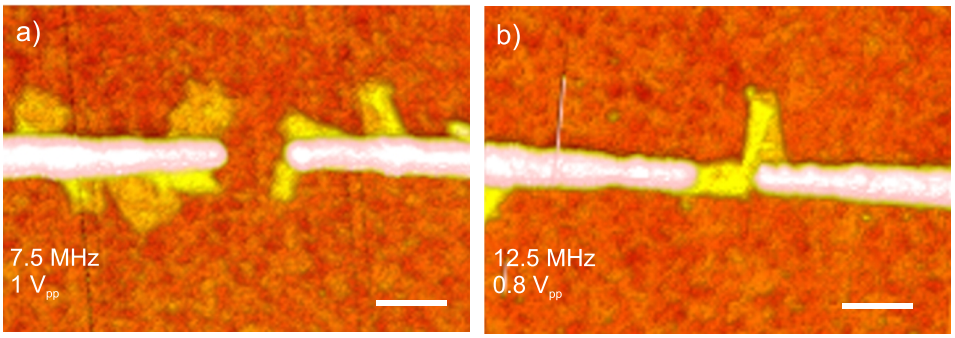

FIGURE 4.3 Effect of the DEP frequency on the trapping of an origami structure. a) DEP frequency below optimal, origami structures are trapped along the electrodes but not in the gap. b) Optimal DEP frequency, one origami structure is trapped precisely in the gap and another one is trapped at the end of the electrode. The scale bar is 100 nm. Adapted from the paper **I.IV.** of this thesis.

trapping of origami structures takes place not only in the gap but also along the electrodes close to the gap. The effect is demonstrated in Fig. 4.4 with smileys in Buffer 1. Another observation was that smaller voltages were required at higher

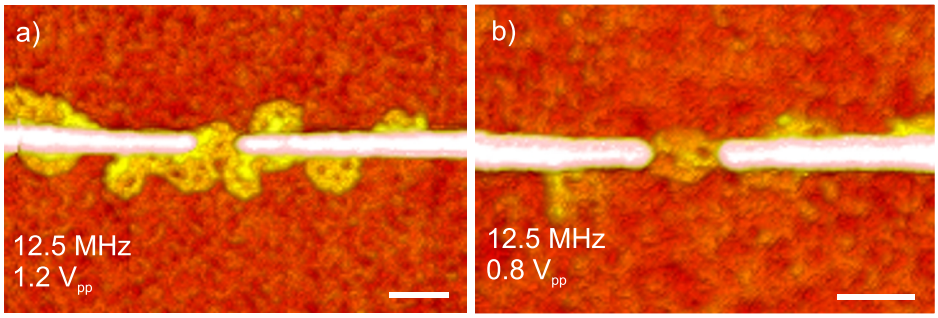

FIGURE 4.4 Effect of the DEP voltage on the trapping of an origami structure. a) DEP voltage above optimal, smileys are trapped not only in the gap but also along the electrodes close to the gap. b) Optimal DEP voltage, a single origami structure is trapped precisely in the gap. The scale bar is 100 nm. Adapted from the paper **I.IV.** of this thesis.

frequencies for the successful trapping of origami structures, which was somewhat surprising considering that the polarizability is expected to decrease with frequency. A plausible explanation is given by the liquid flow due to AC electro-osmosis[69] which reaches a maximum at a certain frequency[99]. The optimal frequency for the trapping of an origami structure was rather high (above 10 MHz) and could be located above this maximum. For frequencies above the maximum, the harmful liquid flow decreases with increasing frequency and therefore lower voltages are sufficient.

After extensive testing of trapping parameters it was observed that the best yield for trapping one origami structure precisely between the electrodes was obtained using 12.5 MHz frequency, and voltages of 1 V_{pp} for magnesium chloride

containing Buffer 2 and 0.8 V_{pp} for magnesium acetate containing Buffer 1. As expected, for the buffer of higher conductivity the trapping voltage should be higher. The yield for trapping a single origami structure with optimal DEP parameters was ∼5 % for Buffer 2 and ∼10 % for Buffer 1. The higher yield is most probably due to the reduced fluid flows (electrothermal and ac electro-osmotic) in the buffer of lower conductivity.

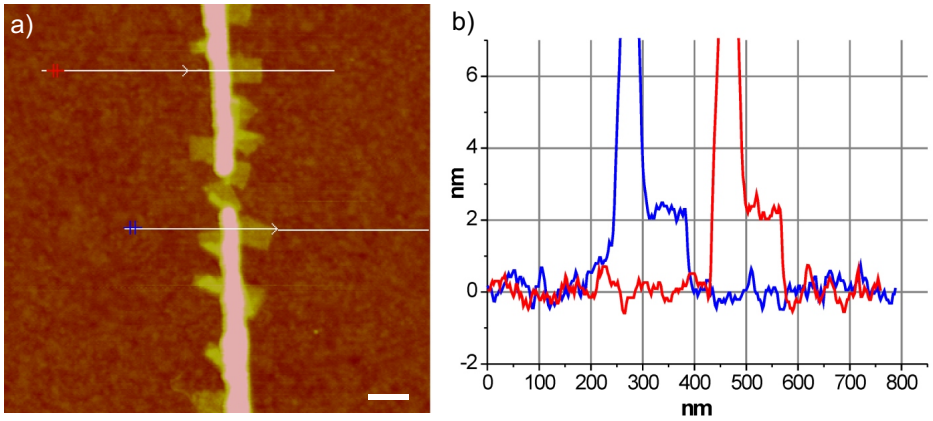

FIGURE 4.5 Height profile of DNA origami structures on SiO_2 surface. a) AFM image of a sample. The scale bar is 100 nm. b) Height profiles along the white lines in a). Adapted from the paper **I.IV.** of this thesis.

As can be seen from the images (Fig. 4.3 and 4.4), the origami structures are often folded after trapping. The problem can be technical (such as folding during the water wash), or fundamental (such as the DEP process favors folded shapes due to increased polarizability), or folding due to complicated fluid flow near the electrodes. The first could be solved by technical improvements; the second may require the attachment of material on the origami structure that helps it to preserve its two-dimensional shape. More tests should be done in order to find the origin of the folding. One important observation from the AFM images is that the origami structures tend to show the height of ∼2 nm (Fig. 4.5), whereas the typical height of a single double-stranded DNA on SiO_2 is ∼1 nm[57]. This suggests that DNA double strands inside origami structures are less deformed due to the interaction with the SiO_2 surface than a single dsDNA, which may be of interest in connection to studies of DNA conductivity where the conformation of DNA is expected to play a major role[57,96,100].

4.2 Assembly of materials using DNA origami

In general, two approaches can be used for utilizing the DNA origami structure for material assembly (see Fig. 4.6):

Approach (1): DNA origami can be used as a prefabricated template for assembly

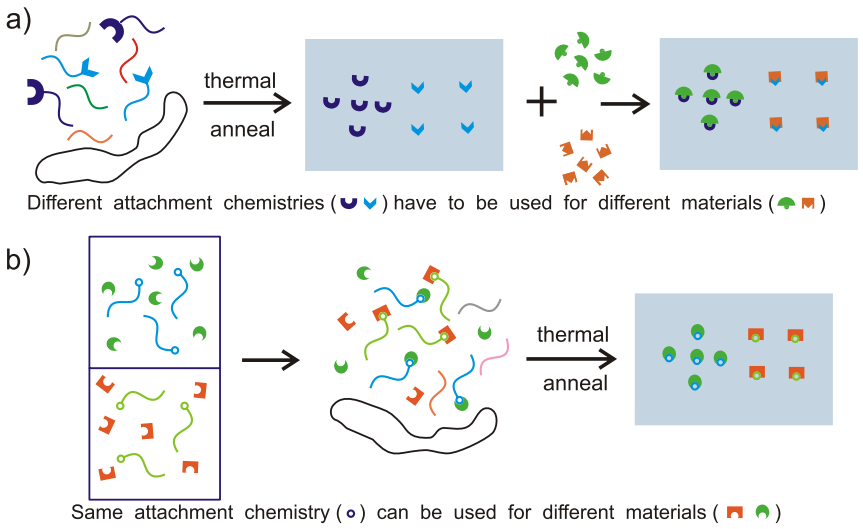

FIGURE 4.6 Two approaches for utilizing DNA origami structure for material assembly. a) DNA origami used as a prefabricated template, materials of choice are attached after the origami structures are assembled. Each material requires different attachment chemistry. b) Simultaneous assembly of DNA origami and materials. The same attachment chemistry can be used for different materials. The assembly of the DNA origami structure drives the assembly of materials. Adopted from the paper **I.V.** of this thesis.

of materials (Fig. 4.6a)). First, origami structures are assembled with certain staple strands having proper functionalizations which serve for attachment of materials of choice. Then the materials are attached to origami structures. Attachment of only one material by this approach is straightforward if the material has binding sites that will attach to functionalizations inside origami: the only important question is the addressability of the functionalization groups inside the origami structure for further attachment. However, for attachment of several materials the complexity of the approach grows with the number of materials that should be attached, since each material needs different attachment chemistry if the materials are to be attached at predefined positions.

Approach (2): Assembly of the DNA origami structure can be used to drive the assembly of materials, i.e., both assemblies take place simultaneously (Fig. 4.6b)). At the first stage, the materials of interest are attached to certain staple strands in separate parallel processes. Then the materials are assembled along the DNA origami assembly. The advantage of this approach is that the same attachment chemistry can be used for different materials. Important questions in this approach are: i) Will the assembly of DNA origami structures be altered by the materials attached to staple strands? ii) Since the origami structures are made by thermal anneal, will the materials tolerate the annealing temperatures?

Streptavidin (STV) protein was chosen as material for assembly to test the efficiency of those two approaches. Streptavidin-biotin recognition served as an attachment chemistry. It is one of the most commonly used attachment chemistries

in biotechnology due to one of the largest free energies of association observed for noncovalent binding[101]. Other advantages are potentially high yields and orthogonality. Moreover, a large variety of STV conjugates are commercially available or can be prepared in a laboratory (metal nanoparticles, semiconducting QD, fluorescent dyes, single walled carbon nanotubes). Thus, streptavidin-biotin recognition is a promising candidate for versatile assembly of materials on DNA structures. First,

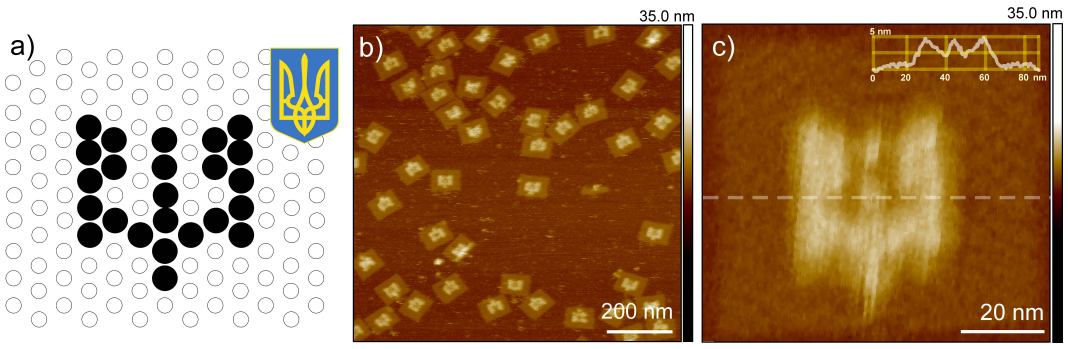

FIGURE 4.7 DNA origami as a prefabricated template for streptavidin assembly. a) Schematic picture of the pattern for SA assembly. The pattern is chosen to resemble the coat of arms of Ukraine (inset). b) Wide field AFM image shows the high yield of STV assembly. c) High magnification AFM image to illustrate the high precision of STV assembly. The inset shows a height profile along the dashed line. Adopted from the paper **I.V.** of this thesis.

the assembly of STV using approach 1 was tested. Inside origami 24 staple strands were chosen to have 5′ biotin modification. After origami anneal, biotin modifications formed a pattern that resembles the coat of arms of Ukraine (inset in Fig. 4.7a)). The minimal distance between two biotin modifications was ∼6 nm. Origami structures were fabricated by thermal annealing (from 90 °C to 20 °C at rate of 1 °C/min in 0.1 °C steps) of 50 μL solution of 10 nM of single-stranded viral DNA (from the M13mp18 virus), with 10x excess concentration of staple strands in 1x TAE Mg++ buffer (1x Tris-Acetate-EDTA (TAE) with 12.5 mM magnesium acetate, pH ∼8.1). After that, STV was added and origami structures were imaged with AFM. For details of origami fabrication see Appendix A.6. As can be seen from the AFM images in Fig. 4.7, STV assembled into the pattern with high yield (Fig. 4.7b)) and precision (Fig. 4.7c)). This result also shows that biotin modification inside origami can be addressed by STV after origami assembly. Note that biotins were attached to the staple strands only through a C6 linker, no additional spacer was used. The yield of assembly was determined as a ratio of structures that resemble the pattern of choice to the total number of origami structures. The definition of "good" structure is rather subjective since it relied on visual inspection. Structures that were considered to resemble the pattern ("good") are marked with black circles in Fig. 4.9a). From 44 origami structures 30 clearly resembled the pattern of choice, thus the yield of assembly estimated in this way was ∼68%. In addition, it is possible that some origamis were im-

mobilized on the surface with the STV structure under the origami, in which case the pattern would not be as well resolved in AFM images. Thus the yield of assembly may be even higher than 68%. Then, the possibility to assemble materials simulta-

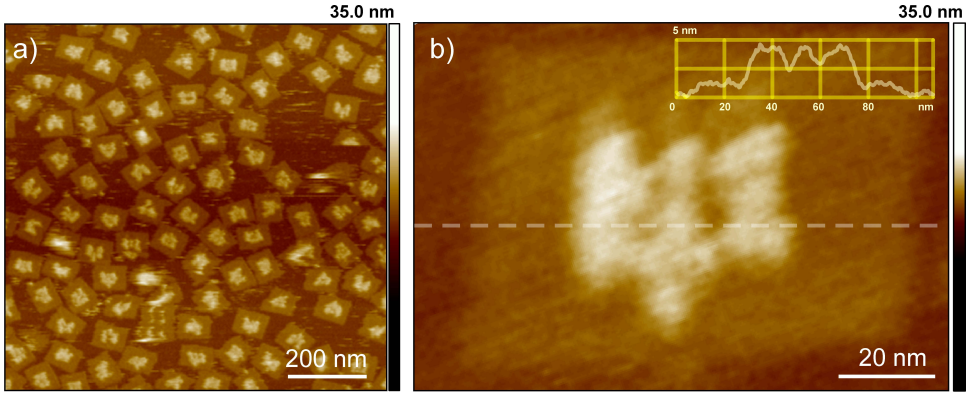

FIGURE 4.8 Assembly of proteins simultaneously with DNA origami assembly (approach 2). a) Wide field AFM image shows the high yield of STV assembly. b) High magnification image to illustrate the high precision of STV assembly. The inset shows a height profile along the dashed line. Adopted from the paper **I.V.** of this thesis.

neously with the origami structures (approach 2) was tested. The same pattern as in the previous example was used. However, this time each of the biotin modified staple strands was functionalized with STV separately before origami annealing, then mixed with the rest of the staple strands and the viral strand. Since the denaturation of STV occurs at temperatures above 75 °C, starting temperature of annealing was 70 °C. It is known that biotin binding increases the midpoint of temperature of thermally induced denaturation of streptavidin[102]. Thus, in order to increase the thermal stability of STV, it was further saturated with biotin after being bound to biotin modified staple strands. Fig. 4.8 shows AFM images of origami-STV structures assembled using approach 2. Again the assembly yield was reasonably high and individual proteins were assembled with high precision. Origami-STV structures fabricated by approach 2 were sensitive to damage induced by AFM tip (the stability problem of DNA origami structures could be solved e.g., by ligation (see ref. [98] and the paper **I.IV.** of this thesis)), thus it was difficult to estimate the yield of assembly accurately, but at least 26 origami structures out of 81 in Fig. 4.9b) clearly showed the pattern, giving 32% as the lower limit for the yield. Possible reasons for decreased mechanical stability of the structures and reduced observed yield of assembly are sterical hindrances introduced by bulky STV molecule (STV is a 53 kDa protein) and/or reduced diffusion rates of the STV conjugated oligoes. However, the results showed that the attachment of the protein to staple strands did not prevent the assembly of origamis. Here it should be noted that STV has neutral charge and assembly of charged proteins by approach 2 could be inhibited by electrostatic repulsion. Approach 2 can be useful for assembly of materials which cannot be directly attached to DNA structures in approach 1 because they require utilization of

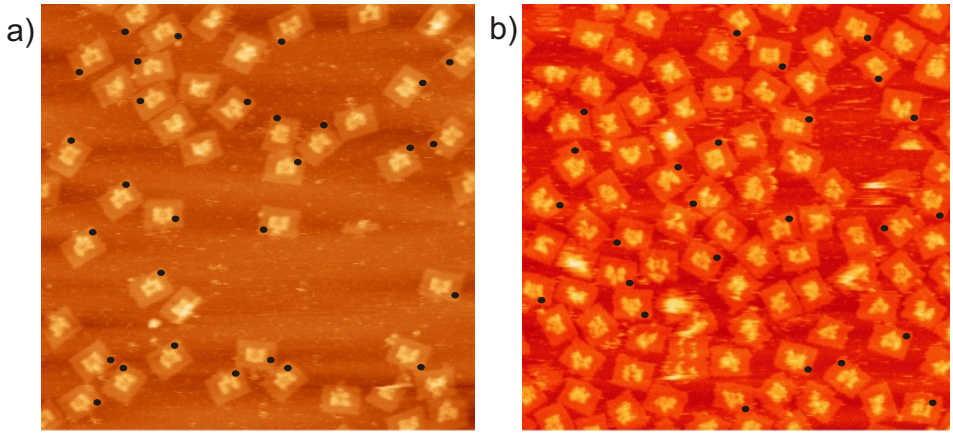

FIGURE 4.9 Evaluation of the assembly yield. a) STV assembly using DNA origami as a template (approach 1). b) Simultaneous assembly of STV and DNA origami structures (approach 2). The scan size is 1x1 μm in both a) and b).

special methods in order to bind them to DNA molecules (for example see ref. [103] and references therein). DNA conjugates with such materials can be prepared beforehand and then the materials can be assembled simultaneously with the DNA origami structures.

An important issue in approach 2 is possible dissociation and reassociation of bonds between the materials and DNA, which might limit its applicability, especially if several materials should be assembled using the same attachment chemistry. For example, it is known that biotin-streptavidin interaction can be reversibly broken in nonionic aqueous solutions at elevated temperatures[104]. For approach 2

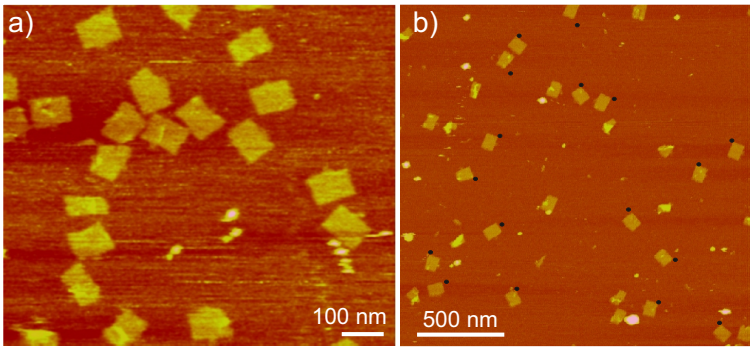

FIGURE 4.10 a) Example of DNA origami structures annealed from 50 °C. b) Evaluation of the assembly yield for origamis assembled by thermal annealing from 50 °C to 20 °C. Structures that are considered to be "good" are marked with black circles. Adopted from the paper **I.V.** of this thesis.

experiments, a buffer of relatively high ionic strength (12.5 mM of magnesium acetate) and 70 °C as starting annealing temperature ware used: biotin-streptavidin bonds stay stable under such conditions[104]. In addition, the ratio of biotin-labeled DNA to free biotin (used to increase the thermal stability of STV) in annealing so-

lution was 1:90. If dissociation of streptavidin/biotin bonds took place, there would be a large number of biotin without DNA to reassociate with, and consequently in our experiment one should then expect $\sim$98% of pixels in the pattern to be missing. This was, obviously, not the case.

Some materials may require even lower annealing temperatures in approach 2. To widen the choice of possible materials, the assembly of DNA origami structures with different starting temperatures for annealing was tested. Origami structures were assembled with yields of more than 50% with starting temperatures as low as 50 °C (see Fig. 4.10), which is below the denaturation temperature of the most proteins under physiological conditions. In this case, 20x excess concentrations of staple strands were used. Recently Simmel and co-workers have demonstrated isothermal assembly of DNA origami structures which is useful for assembly of temperature-sensitive components[105].

5. Conclusions

In this part of the thesis it was demonstrated that dielectrophoresis is a powerful tool for nanoscale manipulation of DNA molecules and DNA self-assembled structures. It allows fabrication of single DNA devices with high yield, which is a basis of studies of molecular properties, e.g. electrical conductivity, on single molecule level. Dielectrophoresis is also a good candidate for bridging top-down and bottom-up fabrication approaches. In addition it was shown that unique DNA self-assembly properties can be used for assembly of materials into complex patterns with below 10 nm resolution. The presented results suggest that a large variety of proteins, and utilizing this also enzymes, can be arranged using the DNA origami assembly. This has potential for creating multiprotein assemblies with nanometer scale precision, as well as potential for efficient self-assembly of complex nanostructures made of materials relevant for electronics, optics and sensing. Combination of DEP and the unique DNA self-assembly properties can find application in less-than-100-nm scale device fabrication.

References

[1] Seeman, N. C. "DNA in a material world". *Nature* **421**, 427 (2003).

[2] Watson, J. D. and Crick, F. H. C. "Molecular structure of nucleic acids: a structure for deoxyribose nucleic acid". *Nature* **171**, 737 (1953).

[3] Amrein, M., Stasiak, A., Gross, H., Stoll, E., and Travaglini, G. "Scanning tunneling microscopy of recA-DNA complexes coated with a conducting film". *Science* **240**, 514 (1988).

[4] Beebe, T., Wilson, T., Ogletree, D., Katz, J., Balhorn, R., Salmeron, M., and Siekhaus, W. "Direct observation of native DNA structures with the scanning tunneling microscope". *Science* **243**, 370 (1989).

[5] Hansma, H. G., Vesenka, J., Siegerist, C., Kelderman, G., Morrett, H., Sinsheimer, R. L., Elings, V., Bustamante, C., and Hansma, P. K. "Reproducible imaging and dissection of plasmid DNA under liquid with the atomic force microscope". *Science* **256**, 1180 (1992).

[6] Hansma, H. G., Laney, D. E., Bezanilla, M., Sinsheimer, R. L., and Hansma, P. K. "Applications for atomic force microscopy of DNA". *Biophys. J.* **68**, 1672 (1995).

[7] Endres, R. G., Cox, D. L., and Singh, R. R. P. "Colloquium: The quest for high-conductance DNA". *Rev. Mod. Phys.* **76**, 195 (2004).

[8] Ghosh, A. and Bansal, M. "A glossary of DNA structures from A to Z". *Acta Crystallogr., Sect D: Biol. Crystallogr.* **59**, 620 (2003).

[9] Bernues, J., Beltran, R., Casasnovas, J., and Azorin, F. "DNA-sequence and metal-ion specificity of the formation of H-DNA". *Nucl. Acids Res.* **18**, 4067 (1990).

[10] Burge, S., Parkinson, G. N., Hazel, P., Todd, A. K., and Neidle, S. "Quadruplex DNA: sequence, topology and structure". *Nucl. Acids Res.* **34**, 5402 (2006).

[11] Adleman, L. M. "Molecular computation of solutions to combinatorial problems". *Science* **266**, 1021 November (1994).

[12] LaBean, T. H. and Li, H. "Constructing novel materials with DNA". *Nano Today* **2**, 26 (2007).

[13] Seeman, N. C. "Nucleic acid junctions and lattices". *J. Theor. Biol.* **99**, 237 (1982).

[14] Kallenbach, N. R., Ma, R., and Seeman, N. C. "An immobile nucleic acid junction constructed from oligonucleotides". *Nature* **305**, 829 (1983).

[15] Park, S. H., Barish, R., Li, H., Reif, J. H., Finkelstein, G., Yan, H., and LaBean, T. H. "Three-helix bundle DNA tiles self-assemble into 2D lattice or 1D templates for silver nanowires". *Nano Lett.* **5**, 693 (2005).

[16] Yan, H., Park, S. H., Finkelstein, G., Reif, J. H., and LaBean, T. H. "DNA-templated self-assembly of protein arrays and highly conductive nanowires". *Science* **301**, 1882 (2003).

[17] Mao, C., Sun, W., and Seeman, N. C. "Designed two-dimensional DNA holliday junction arrays visualized by atomic force microscopy". *J. Am. Chem. Soc.* **121**, 5437 (1999).

[18] Winfree, E., Liu, F., Wenzler, L. A., and Seeman, N. C. "Design and self-assembly of two-dimensional DNA crystals". *Nature* **394**, 539 (1998).

[19] LaBean, T. H., Yan, H., Kopatsch, J., Liu, F., Winfree, E., Reif, J. H., and Seeman, N. C. "Construction, analysis, ligation, and self-assembly of DAN triple crossover complexes". *J. Am. Chem. Soc.* **122**, 1848 (2000).

[20] Park, S. H., Yin, P., Liu, Y., Reif, J. H., LaBean, T. H., and Yan, H. "Programmable DNA self-assemblies for nanoscale organization of ligands and proteins". *Nano Lett.* **5**, 729 (2005).

[21] Rothemund, P. W. K., Ekani-Nkodo, A., Papadakis, N., Kumar, A., Fygenson, D. K., and Winfree, E. "Design and characterization of programmable DNA nanotubes". *J. Am. Chem. Soc.* **126**, 16344 (2004).

[22] Mitchell, J. C., Harris, J. R., Malo, J., Bath, J., and Turberfield, A. J. "Self-assembly of chiral DNA nanotubes". *J. Am. Chem. Soc.* **126**, 16342 (2004).

[23] Liu, D., Park, S. H., Reif, J. H., and LaBean, T. H. "DNA nanotubes self-assembled from triple-crossover tiles as templates for conductive nanowires". *Proc. Nat. Acad. Sci. U.S.A.* **101**, 717 (2004).

[24] Yin, P., Hariadi, R. F., Sahu, S., Choi, H. M. T., Park, S. H., LaBean, T. H., and Reif, J. H. "Programming DNA tube circumferences". *Science* **321**, 824 (2008).

[25] Chen, J. H. and Seeman, N. C. "Synthesis from DNA of a molecule with the connectivity of a cube". *Nature* **350**, 631 (1991).

[26] Shih, W. M., Quispe, J. D., and Joyce, G. F. "A 1.7-kilobase single-stranded DNA that folds into a nanoscale octahedron". *Nature* **427**, 618 (2004).

[27] Goodman, R. P., Schaap, I. A. T., Tardin, C. F., Erben, C. M., Berry, R. M., Schmidt, C. F., and Turberfield, A. J. "Rapid chiral assembly of rigid DNA building blocks for molecular nanofabrication". *Science* **310**, 1661 (2005).

[28] He, Y., Ye, T., Su, M., Zhang, C., Ribbe, A. E., Jiang, W., and Mao, C. "Hierarchical self-assembly of DNA into symmetric supramolecular polyhedra". *Nature* **452**, 198 (2008).

[29] Simmel, F. "Three-dimensional nanoconstruction with DNA". *Angew. Chem. Int. Ed.* **47**, 5884 (2008).

[30] Rothemund, P. W. K. "Folding DNA to create nanoscale shapes and patterns". *Nature* **440**, 297 (2006).

[31] Aldaye, F. A., Palmer, A. L., and Sleiman, H. F. "Assembling materials with dna as the guide". *Science* **321**, 1795 (2008).

[32] Gu, Q., Cheng, C., Gonela, R., Suryanarayanan, S., Anabathula, S., Dai, K., and Haynie, D. "DNA nanowire fabrication". *Nanotechnology* **17**, R14 (2006).

[33] Keren, K., Krueger, M., Gilad, R., Ben-Yoseph, G., Sivan, U., and Braun, E. "Sequence-specific molecular lithography on single DNA molecules". *Science* **297**, 72 (2002).

[34] Warner, M. G. and Hutchison, J. E. "Linear assemblies of nanoparticles electrostatically organized on DNA scaffolds". *Nat. Mater.* **2**, 272 (2003).

[35] Keren, K., Berman, R. S., Buchstab, E., Sivan, U., and Braun, E. "DNA-templated carbon nanotube field-effect transistor". *Science* **302**, 1380 (2003).

[36] Garibotti, A. V., Knudsen, S. M., Ellington, A. D., and Seeman, N. C. "Functional DNAzymes organized into two-dimensional arrays". *Nano Lett.* **6**, 1505 (2006).

[37] Park, S. H., Pistol, C., Ahn, S. J., Reif, J. H., Lebeck, A. R., Dwyer, C., and LaBean, T. H. "Finite-size fully addressable DNA tile lattices formed by hierarchical assembly procedures". *Angew. Chem. Int. Ed.* **45**, 735 (2006).

[38] Zheng, J., Constantinou, P. E., Micheel, C., Alivisatos, A. P., Kiehl, R. A., and Seeman, N. C. "Two-dimensional nanoparticle arrays show the organizational power of robust DNA motifs". *Nano Lett.* **6**, 1502 (2006).

[39] Le, J. D., Pinto, Y., Seeman, N. C., Musier-Forsyth, K., Taton, T. A., and Kiehl, R. A. "DNA-templated self-assembly of metallic nanocomponent arrays on a surface". *Nano Lett.* **4**, 2343 (2004).

[40] Zhang, J., Liu, Y., Ke, Y., and Yan, H. "Periodic square-like gold nanoparticle arrays templated by self-assembled 2D DNA nanogrids on a surface". *Nano Lett.* **6**, 248 (2006).

[41] Sharma, J., Chhabra, R., Liu, Y., Ke, Y., and Yan, H. "DNA-templated self-assembly of two-dimensional and periodical gold nanoparticle arrays". *Angew. Chem. Int. Ed.* **45**, 730 (2006).

[42] Sharma, J., Ke, Y., Lin, C., Chhabra, R., Wang, Q., Nangreave, J., Liu, Y., and Yan, H. "DNA-tile-directed self-assembly of quantum dots into two-dimensional nanopatterns". *Angew. Chem. Int. Ed.* **47**, 5157 (2008).

[43] Chhabra, R., Sharma, J., Ke, Y., Liu, Y., Rinker, S., Lindsay, S., and Yan, H. "Spatially addressable multiprotein nanoarrays templated by aptamer-tagged DNA nanoarchitectures". *J. Am. Chem. Soc.* **129**, 10304 (2007).

[44] Sharma, J., Chhabra, R., Andersen, C. S., Gothelf, K. V., Yan, H., and Liu, Y. "Toward reliable gold nanoparticle patterning on self-assembled DNA nanoscaffold". *J. Am. Chem. Soc.* **130**, 7820 (2008).

[45] Eley, D. D. and Spivey, D. I. "Semiconductivity of organic substances. Part 9.-Nucleic acid in the dry state". *Trans. Far. Soc.* **58**, 411 (1962).

[46] Flood, A. H., Stoddart, J. F., Steuerman, D. W., and Heath, J. R. "Chemistry. Whence molecular electronics?". *Science* **306**, 2055 (2004).

[47] Retèl, J., Hoebee, B., Braun, J. E., Lutgerink, J. T., van den Akker, E., Wanamarta, A. H., Joenje, H., and Lafleur, M. V. "Mutational specificity of oxidative DNA damage". *Mutat. Res.* **299**, 165 (1993).

[48] Dekker, C. and Ratner, M. "Electronic properties of DNA". *Phys. World* **14**, 29 (2001).

[49] Braun, E., Eichen, Y., Sivan, U., and Ben-Yoseph, G. "DNA-templated assembly and electrode attachment of a conducting silver wire". *Nature* **391**, 775 (1998).

[50] Fink, H. and Schonenberger, C. "Electrical conduction through DNA molecules". *Nature* **398**, 407 (1999).

[51] Porath, D., Bezryadin, A., de Vries, S., and Dekker, C. "Direct measurement of electrical transport through DNA molecules". *Nature* **403**, 635 (2000).

[52] Kasumov, A. Y., Kociak, M., Gueron, S., Reulet, B., Volkov, V. T., Klinov, D. V., and Bouchiat, H. "Proximity-induced superconductivity in DNA". *Science* **291**, 280 (2001).

[53] Hipps, K. W. "Molecular electronics: It's all about contacts". *Science* **294**, 536 (2001).

[54] Roy, S., Vedala, H., Roy, A. D., Kim, D.-h., Doud, M., Mathee, K., Shin, H.-k., Shimamoto, N., Prasad, V., and Choi, W. "Direct electrical measurements on single-molecule genomic dna using single-walled carbon nanotubes". *Nano Lett.* **8**, 26 (2008).

[55] Vedala, H., Roy, S., Doud, M., Mathee, K., Hwang, S., Jeon, M., and Choi, W. "The effect of environmental factors on the electrical conductivity of a single oligo-DNA molecule measured using single-walled carbon nanotube nanoelectrodes". *Nanotechnology* **19**, 265704 (2008).

[56] Guo, X., Gorodetsky, A. A., Hone, J., Barton, J. K., and Nuckolls, C. "Conductivity of a single DNA duplex bridging a carbon nanotube gap". *Nat. Nanotechnol.* **3**, 163 (2008).

[57] Kasumov, A. Y., Klinov, D. V., Roche, P.-E., Guéron, S., and Bouchiat, H. "Thickness and low-temperature conductivity of DNA molecules". *Appl. Phys. Lett.* **84**, 1007 (2004).

[58] Tran, P., Alavi, B., and Gruner, G. "Charge transport along the λ-DNA double helix". *Phys. Rev. Lett.* **85**, 1564 (2000).

[59] Pohl, H. A. "The motion and precipitation of suspensoids in divergent electric fields". *J. Appl. Phys.* **22**, 869 (1951).

[60] Pohl, H. A. *Dielectrophoresis*. Cambridge University Press,Cambridge, (1978).

[61] Jones, T. B. *Electromechanics of Particles*. Cambridge University Press, New York City, (1995).

[62] Jones, T. B. "Basic theory of dielectrophoresis and electrorotation". *IEEE Eng. Med. Biol. Mag.* **22**, 33 (2003).

[63] Zheng, L., Brody, J. P., and Burke, P. J. "Electronic manipulation of DNA, proteins, and nanoparticles for potential circuit assembly". *Biosensors & Bioelectronics* **20**, 606 (2004).

[64] Cui, L., Holmes, D., and Morgan, H. "The dielectrophoretic levitation and separation of latex beads in microchips". *ELECTROPHORESIS* **22**, 3893 (2001).

[65] Wang, X. B., Huang, Y., Becker, F. F., and Gascoyne, P. R. C. "A unified theory of dielectrophoresis and travelling wave dielectrophoresis". *J. Phys. D: Appl. Phys.* **27**, 1571 (1994).

[66] Jones, T. B. and Washizu, M. "Multipolar dielectrophoretic and electrorotation theory". *J. Electrostat.* **37**, 121 (1996).

[67] Washizu, M. "Equivalent multipole-moment theory for dielectrophoresis and electrorotation in electromagnetic field". *J. Electrostat.* **62**, 15 (2004).

[68] Wang, X., Wang, X., and Gascoyne, P. R. C. "General expressions for dielectrophoretic force and electrorotational torque derived using the Maxwell stress tensor method". *J. Electrostat.* **39**, 277 (1997).

[69] Castellanos, A., Ramos, A., González, A., Green, N. G., and Morgan, H. "Electrohydrodynamics and dielectrophoresis in microsystems: scaling laws". *J. Phys. D: Appl. Phys.* **36**, 2584 (2003).

[70] Masuda, S., Washizu, M., and Nanba, T. "Novel method of cell fusion in field constriction area in fluid integration circuit". *IEEE Trans. Ind. Appl.* **25**, 732 (1989).

[71] Masuda, S., Washizu, M., and Kawabata, I. "Movement of blood cells in liquid by nonuniform traveling field". *IEEE Trans. Ind. Appl.* **24**, 217 (1988).

[72] Muller, T., Gerardino, A., Schnelle, T., Shirley, S. G., Bordoni, F., Gasperis, G. D., Leoni, R., and Fuhr, G. "Trapping of micrometre and sub-micrometre particles by high-frequency electric fields and hydrodynamic forces". *J. Phys. D: Appl. Phys.* **29**, 340 (1996).

[73] Hughes, M. P. and Morgan, H. "Dielectrophoretic trapping of single sub-micrometre scale bioparticles". *J. Phys. D: Appl. Phys.* **31**, 2205 (1998).

[74] Hughes, M. P., Morgan, H., and Rixon, F. J. "Dielectrophoretic manipulation and characterization of herpes simplex virus-1 capsids". *Eur. Biophys. J.* **30**, 268 (2001).

[75] Kawabata, T. and Washizu, M. "Dielectrophoretic detection of molecular bindings". *IEEE Trans. Ind. Appl.* **37**, 1625 (2001).

[76] Vijayaraghavan, A., Blatt, S., Weissenberger, D., Oron-Carl, M., Hennrich, F., Gerthsen, D., Hahn, H., and Krupke, R. "Ultra-large-scale directed assembly of single-walled carbon nanotube devices". *Nano Lett.* **7**, 1556 (2007).

[77] Hölzel, R. and Bier, F. F. "Dielectrophoretic manipulation of DNA". *IEE Proc. Nanobiotechnol.* **150**, 47 (2003).

[78] Burke, P. J. *Nanodielectrophoresis: electronic nanotweezers*. American Scientific Publishers, (2004).

[79] Lapizco-Encinas, B. H. and Rito-Palomares, M. "Dielectrophoresis for the manipulation of nanobioparticles". *Electrophoresis* **28**, 4521 (2007).

[80] Tuukkanen, S. *Dielectrophoresis as a tool for on-chip positioning of DNA and electrical characterization of nanoscale DNA*. Research report, no. 13/2006, Department of Physics, University of Jyväskylä, (2006).

[81] Storm, A. J., van Noort, J., de Vries, S., and Dekker, C. "Insulating behavior for DNA molecules between nanoelectrodes at the 100 nm length scale". *Appl. Phys. Lett.* **79**, 3881 (2001).

[82] Noort, S. J. T. V., der Werf, K. O. V., Grooth, B. G. D., Hulst, N. F. V., and Greve, J. "Height anomalies in tapping mode atomic force microscopy in air caused by adhesion". *Ultramicroscopy* **69**, 117 (1997).

[83] Ajdari, A. and Prost, J. "Free-flow electrophoresis with trapping by a transverse inhomogeneous field". *Proc. Nat. Acad. Sci. U.S.A.* **88**, 4468 (1991).

[84] Regtmeier, J., Duong, T. T., Eichhorn, R., Anselmetti, D., and Ros, A. "Dielectrophoretic manipulation of DNA: separation and polarizability". *Anal. Chem.* **79**, 3925 (2007).

[85] Suzuki, S., Yamanashi, T., Tazawa, S., Kurosawa, O., and Washizu, M. "Quantitative analysis of DNA orientation in stationary ac electric fields using fluorescence anisotropy". *IEEE Trans. Ind. Appl.* **34**, 75 (1998).

[86] Saif, B., Mohr, R. K., Montrose, C. J., and Litovitz, T. A. "On the mechanism of dielectric relaxation in aqueous DNA solutions". *Biopolymers* **31**, 1171 (1991).

[87] Bakewell, D. and Morgan, H. "Dielectrophoresis of DNA: time- and frequency-dependent collections on microelectrodes". *IEEE Trans. Nanobiosci.* **5**, 139 (2006).

[88] Zhang, Y., Austin, R. H., Kraeft, J., Cox, E. C., and Ong, N. P. "Insulating behavior of λ-DNA on the micron scale". *Phys. Rev. Lett.* **89**, 198102 (2002).

[89] Kleine, H., Wilke, R., Pelargus, C., Rott, K., Pühler, A., Reiss, G., Ros, R., and Anselmetti, D. "Absence of intrinsic electric conductivity in single dsDNA molecules". *J. Biotechnol.* **112**, 91 (2004).

[90] Zareie, M. H. and Lukins, P. B. "Atomic-resolution STM structure of DNA and localization of the retinoic acid binding site". *Biochem. Biophys. Res. Commun.* **303**, 153 (2003).

[91] Yamahata, C., Collard, D., Takekawa, T., Kumemura, M., Hashiguchi, G., and Fujita, H. "Humidity dependence of charge transport through DNA revealed by silicon-based nanotweezers manipulation". *Biophys. J.* **94**, 63 (2008).

[92] Kleine-Ostmann, T., Jordens, C., Baaske, K., Weimann, T., de Angelis, M., and Koch, M. "Conductivity of single-stranded and double-stranded deoxyribose nucleic acid under ambient conditions: The dominance of water". *Appl. Phys. Lett.* **88**, 102102 (2006).

[93] Song, C., Xia, Y., Zhao, M., Liu, X., Li, J., and Li, L. "The electronic structure evolution of DNA during its conformation transition process". *Phys. Chem. Chem. Phys.* **10**, 5077 (2008).

[94] Berashevich, J. and Chakraborty, T. "How the surrounding water changes the electronic and magnetic properties of DNA". *J. Phys. Chem. B* **112**, 14083 (2008).

[95] Wang, J. "Electrical conductivity of double stranded DNA measured with ac impedance spectroscopy". *Phys. Rev. B* **78**, 245304 (2008).

[96] Linko, V., Paasonen, S., Kuzyk, A., Törmä, P., and Toppari, J. J. "Characterisation of the conductance mechanisms of the DNA origami by AC impedance spectroscopy". *submitted* (2009).

[97] Wilner, O. I., Weizmann, Y., Gill, R., Lioubashevski, O., Freeman, R., and Willner, I. "Enzyme cascades activated on topologically programmed DNA scaffolds". *Nat. Nanotechnol.* **4**, 249 (2009).

[98] O'Neill, P., Rothemund, P. W. K., Kumar, A., and Fygenson, D. K. "Sturdier DNA nanotubes via ligation". *Nano Lett.* **6**, 1379 (2006).

[99] Gierhart, B. C., Howitt, D. G., Chen, S. J., Smith, R. L., and Collins, S. D. "Frequency dependence of gold nanoparticle superassembly by dielectrophoresis". *Langmuir* **23**, 12450 (2007).

[100] Tuukkanen, S., Kuzyk, A., Toppari, J. J., Hytönen, V. P., Ihalainen, T., and Törmä, P. "Dielectrophoresis of nanoscale double-stranded DNA and humidity effects on its electrical conductivity". *Appl. Phys. Lett.* **87**, 183102 (2005).

[101] Wilchek, M. and Bayer, E. A. "The avidin-biotin complex in bioanalytical applications". *Anal. Biochem.* **171**, 1 (1988).

[102] González, M., Argaraña, C. E., and Fidelio, G. D. "Extremely high thermal stability of streptavidin and avidin upon biotin binding". *Biomol. Eng.* **16**, 67 (1999).

[103] Duckworth, B., Chen, Y., Wollack, J., Sham, Y., Mueller, J., Taton, T., and Distefano, M. "A universal method for the preparation of covalent protein-DNA conjugates for use in creating protein nanostructures". *Angew. Chem. Int. Ed.* **119**, 8975 (2007).

[104] Holmberg, A., Blomstergren, A., Nord, O., Lukacs, M., Lundeberg, J., and Uhlén, M. "The biotin-streptavidin interaction can be reversibly broken using water at elevated temperatures". *Electrophoresis* **26**, 501 (2005).

[105] Jungmann, R., Liedl, T., Sobey, T. L., Shih, W., and Simmel, F. C. "Isothermal assembly of DNA origami structures using denaturing agents". *J. Am. Chem. Soc.* **130**, 10062 (2008).

Part II

Molecular devices for plasmonics

6. Background

It is often said that now we are living in the "Information Age" or the "Information Era", times that are characterized by the ability of individuals to transfer information freely and to have instant access to knowledge that would have previously have been difficult or impossible to find. This was made possible mainly by the progress in such technologies as electronics and photonics, in other word, by the knowledge of how to use electrons and photons to carry, store, and process information. Electronics is mostly used to process information and to transport it on relatively short distances. On the other hand photonics is mostly used to transport information over large distances. The integration of both photonics and electronics is limited by the difference in size of typical components. Nowadays, transistors used in silicon integrated circuits have features of 100 nanometers or smaller. In optics, the typical size of components is limited by the diffraction limit and is in the order of micrometers. Surface plasmon polaritons (SPP) or surface plasmons (SPs), allow to confine light below the diffraction limit. Thus, they may offer the solution to the size-compatibility problem, and provide the path to integrated electrical and optical circuits. As a phenomenon, surface plasmons have been known for a long time[1]. However, only recent advantages in nanofabrication allowed controlled manipulation of SPs in sub-wavelength scales[2]. Combination of properties of fluorescent molecules and surface plasmons opens new interesting ways to manipulate properties of SPs[3,4] and influence the florescence properties of molecules[5].

6.1 Surface plasmon polaritons

When the light interacts with free electrons in a metal films, the surface electrons on the metal/dielectric interface oscillate collectively and absorb, scatter, or re-radiate the incident photons. This results in surface electromagnetic wave that propagates in the plane of the film (Fig. 6.1a)) with ranges around 10 to 100 μm but decays exponentially with increasing distance into each medium from the interface (Fig. 6.1b)). These propagating electromagnetic modes are properly termed surface plasmon polaritons (SPP), but are often referred to simply as surface plasmons (SPs). The electromagnetic field of SPs is confined to the vicinity of the dielectric/metal interface. This confinement leads to an enhancement of the electromagnetic field intensity by a factor of 10 to 100 relative to the incident intensity resulting in an extraordinary sensitivity of SPs to surface conditions. The electromagnetic field of a surface plasmon polariton at a dielectric/metal interface can be obtained from the solution of the Maxwell's equations in each medium and the associated boundary conditions

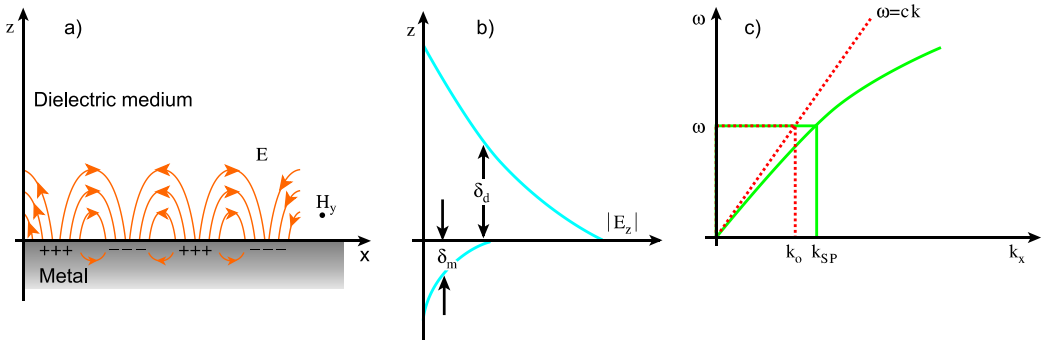

FIGURE 6.1 Schematic picture of surface plasmon polaritons, surface electromagnetic waves which propagate in the plane of the film (a) but decay exponentially with increasing distance into each medium from the interface (b). c) SPs dispersion relation (green), and comparison with dispersion for free propagation light (red). The momentum mismatch between k_{sp} and k_0 should be overcome in order to couple light to SPs. Adapted with permission from [2].

(for a derivation see, for example, ref. [6]). From the solution one obtains SPs dispersion relation (Fig. 6.1c)), i.e., the frequency dependence on the SP wave-vector, k_{sp},

$$k_{sp} = k_0 \sqrt{\frac{\varepsilon_d \varepsilon_m}{\varepsilon_d + \varepsilon_m}}, \tag{6.1}$$

where ε_d and ε_m are frequency dependent permittivities of the metal and the dielectric material respectively, and k_0 is the free-space wavevector. Real parts of permittivities ε_d and ε_m should have opposite signs in order for SPs to be possible at the interface. The condition is satisfied for metals, since the real part of ε_m is negative. An important characteristics of SPs is the propagation length δ_{sp}, which is described by the following equation:

$$\delta_{sp} = \frac{c}{\omega} \left(\frac{\varepsilon'_m + \varepsilon_d}{\varepsilon'_m \varepsilon_d} \right)^{\frac{3}{2}} \frac{(\varepsilon'_m)^2}{\varepsilon''_m}. \tag{6.2}$$

Where ε'_m and ε''_m are the real and imaginary parts of the dielectric function of the metal, i.e., $\varepsilon_m = \varepsilon'_m + i\varepsilon''_m$. For a "good" metal, such as silver, the propagation distances are typically in the range of 10 to 100 μm for the visible spectrum, increasing to milliliter range for the near infrared. Other important characteristics are decay lengths into the dielectric (δ_d) and the metal (δ_m) (see Fig. 6.1b)) which are in the order of 100 nm and 10 nm respectively.

Surface plasmons are essentially light waves that are trapped on the surface. Thus, they are intrinsically two-dimensional in nature and, in principle, could be easily manipulated. One of the most important features of SPs is that they can be confined to dimensions much smaller than the wavelength of the light in free space. This could allow to scale down optical devices, and ultimately provide the

pass to integrated electrical and optical circuits for the information processing at the nanoscale[2,7–9]. Significant progress has been made in this direction during the last decade. Plasmonic waveguides of various geometries[10–13] and sizes down to ∼100 nm[14,15] have been demonstrated. Also various plasmonic optical elements such as lenses, mirrors, interferometers, filters, splitters and demultiplexers[12,16–21] were realized. Some progress has also been achieved in integration of plasmonic and optical waveguides[22]. Figure 6.2 shows a few examples of plasmonic optical elements.

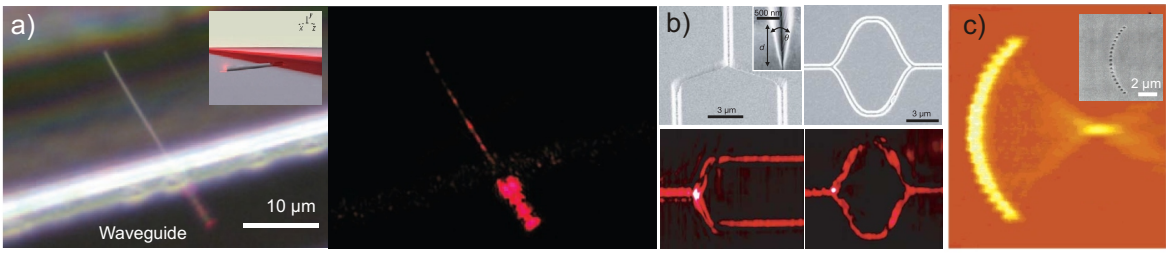

FIGURE 6.2 Plasmonic optical elements. a) Integration of photonic and silver nanowire plasmonic waveguides (schematic picture in the inset). On the left: image taken with white light illuminations shows the positions of optical and plasmonic waveguides. On the right: image without illumination showing plasmon propagation along the nanowire. b) Channel plasmon waveguide, splitter and interferometer. On the top, SEM images of the structures, on the bottom SNOM images showing plasmon propagation, and splitting. c) Plasmonic lenses based on an array of holes arranged in a quarter circle with 5 μm radius. The focusing is demonstrated by imaging the plasmon intensity with SNOM. In the inset ia a SEM image of the structure. Adopted with permission from ref. [22] (a), ref. [12] (b) and ref. [17] (c).

6.2 Coupling of light to surface plasmons

In order to excite a surface plasmon polariton the frequency of the incident light must equal the frequency of the SP, and the component of the wave vector of the incident light parallel to the surface, $k_0 \sin\theta$ where θ is the angle of incidence, must equal the wave vector of the SP, k_{sp}. The first condition is easily satisfied. However, as one can see from Eq. 6.1 and Fig. 6.1c), the SP wave vector k_{sp} is larger than k_0. The resulting mismatch must be bridged in order to couple far field light to SPs. Several experimental arrangements were designed to provide the missing momentum (see Fig. 6.3). Probably the most frequently used the is the so-called Kretschmann geometry[23], shown in Fig. 6.3a) and b).

In this configuration, a metal film is illuminated through a prism at an angle of incidence larger than the critical angle for total internal reflection. The prism is optically more dense medium, thus, the wavevector of light increases and at certain angle of incidence θ_{sp} such that $k_{sp} = k_0 n_{prizm} \sin\theta_{sp}$ light can be coupled to SPs. The coupling is observed as a sharp minima in the reflectivity from the prism (inset of

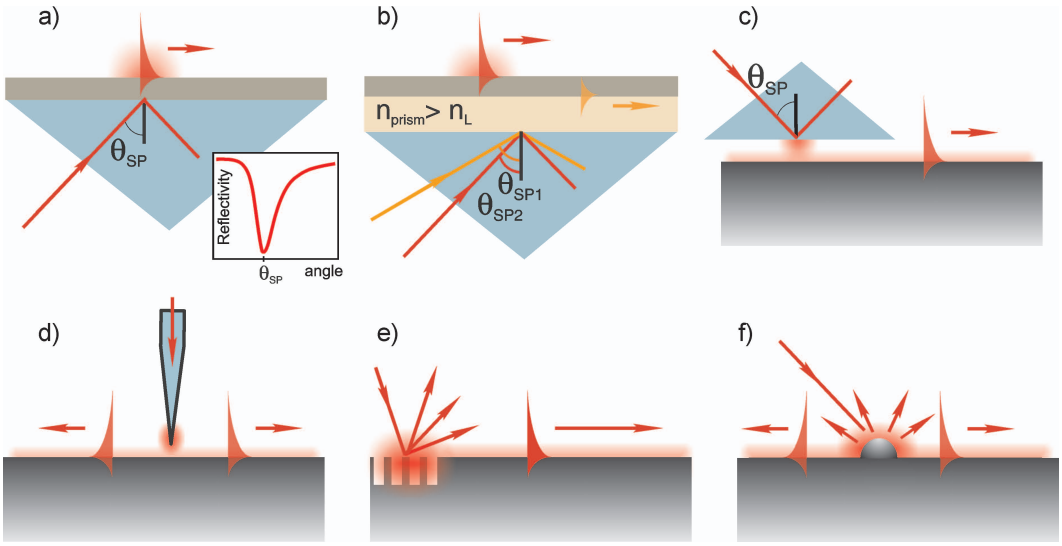

FIGURE 6.3 Schematic pictures of SP excitation geometries. a) Kretschmann geometry. The inset shows a typical dependence of the prism reflectivity on angle. At angle θ_{sp} a sharp minimum is observed due to the coupling of light to SPs. b) Two-layer Kretschmann geometry. c) Otto geometry. d) Excitation with a SNOM probe. e) Diffraction on a grating. f) Diffraction on surface features. Adapted with permission from [6].

Fig. 6.3a)). In such configuration SPs are excited only on one side of the metal film. It it possible to excite SPs on both sides, for this an additional dielectric layer with a refractive index smaller than n_{prizm} should be deposited between the prism and the metal film (Fig. 6.3b)). Although light can be couple to SPs on both interfaces, the coupling happens at different angles of illumination. For a thick metal film the so-called Otto configuration can be used to excite SPs (Fig. 6.3c)). It is similar in principle to the Kretschmann geometry. The difference here is that the prism where the total internal reflection occurs is placed close to the metal surface, so that photon tunneling occurs through the air gap between the prism and the surface. Another way to excite plasmons is by illumination through SNOM (scanning near-field optical microscope) tip (Fig. 6.3d)). The technique is analogous to the Otto configuration and has an advantage of local (with sub-wavelength precision) excitation of SPs at the position of the SNOM tip. The missing momentum can be also provided through diffraction of light on a periodic structure (Fig. 6.3e)). This method has advantages of high efficiency and localization of coupling, which come at a price of additional fabrication steps to create the periodic structure. In principle no special geometry is needed to excite plasmons on rough surfaces (Fig. 6.3f)). SPs excitation is possible since light diffracted on defects has all wavevectors and some of them are equal to k_{sp}. The disadvantage of this approach is that excitation conditions are not well defined and the efficiency of excitation is low. Besides these methods, SPs can be also excited by emitters which are placed in close proximity to the surface. This method is discussed in detail in the next section.

6.3 Molecular plasmonics

Utilization of the interaction between surface plasmons and molecules opens new possibilities in manipulation of properties of both plasmons and molecules. Molecules can be used to excite and detect SPs (see the paper **II.I.** of this thesis). Moreover, it is possible to influence the frequency of plasmons (see paper **I.II.** of this thesis) and its propagation[24,25]. Surface plasmons can also be used for energy transfer between molecules over relatively large distances (in the order of few tenths of μm, for example see ref. [26–28] and the paper **II.I.** of this thesis). Such energy transfer can find application, e.g, in artificial light harvesting systems. A wide range of fluorescent molecules or semiconducting quantum dots can be used to manipulate SPs. Usually, no special interaction geometry is needed, any light source can be used to excite SPs via molecules. Moreover, with molecules it is possible to localize the excitation and the detection regions below the diffraction limit. In addition, the use of molecules has the potential for integration with molecular electronics and the use of molecular self-assembly in fabrication. On the other hand, plasmons can be used to influence the fluorescent properties of molecules[29], e.g to enhance their fluorescence[30,31]. Probably the most widely applied interaction of molecules and plasmons is surface enhanced Raman scattering (SERS)[32]. The next sections provide some background into the interaction of fluorescent molecules and SPs.

6.3.1 Decay of excited molecules to SPs

The properties of a single emitter near a planar metallic surface are strongly influenced by the presence of the interface. First of all, the interface modifies the boundary conditions of the electromagnetic field, and it may alter both the radiative decay rate and the spatial distribution of the emitted radiation. Secondly, the excited emitter can lose its energy to the metal via non-radiative energy transfer. There are several excellent reviews on the topic of emitter-interface interaction[29,33]. This section is focused on the interaction of fluorescent molecules with SPs. Consider an emitter

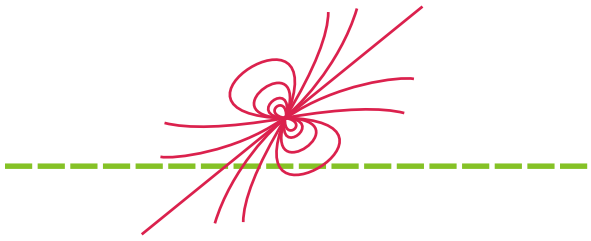

FIGURE 6.4 Electric field lines of an electric dipole. The dashed line represents an interface.

situated close to an interface. In the classical approach the emitter can be modeled as a forced damped dipole oscillator; it is *forced*, because the field reflected by the interface provides a driving term, it is *damped* because it radiates power, it is an electric

dipole because many atomic or molecular transitions that produce light are of electrical dipole nature. The field due to the dipole it shown schematically in Fig. 6.4. In the near field region, i.e., at distances of about λ, the field contains components with a wide range of wavevectors k. Some of those k have their component in the plane of the surface that is equal to k_{sp}. Thus, the dipole can couple to the surface plasmon mode. In addition to SPs, an excited emitter can also decay radiatively (with emission of far field light) or non-radiatively to so-called lossy waves. The efficiency of coupling to different decay channels depends on the details of the system. Figure 6.5 shows the calculated fraction of power dissipated by an emitter to different decay channels. The emitter has a wavelength of emission 614 nm, immersed in vacuum and positioned above a silver interface. As one can see, the relative fractions of dissipated power strongly depend on the orientation of the emitter and its distance from the surface. The highest coupling to the SP mode ($\sim$90%) is achieved for an emitter which is situated $\sim$ 200 nm from the surface with a dipole moment oriented perpendicular to the interface (Figure 6.5a)). For isotropic orientation of the dipole moment, coupling to the SP mode can be as high as 30% at distances of $\sim$ 20 nm from the surface. The fact that a significant fraction of excited emitters adjacent to a metal surface decay to non-radiative channels, one of which is SPs, effectively decreases the radiative quantum yield. This is definitely an unwanted effect for light emitting devices, e.g., OLED, since, unless recovered in some way, the energy in the non-radiative modes is lost[34,35]. However, one can think about using this process to directly excite SPs. Recent realization of organic plasmon-emitting diode[36], i.e, an electrically controlled source of plasmons, is an example of advances in this direction. Plasmonic decay route is also the origin of the phenomenon of surface plasmon-coupled emission (SPCE), which has a great promise as a new method of fluorescence detection[37].

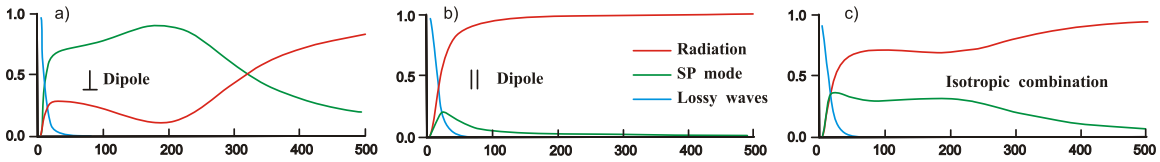

FIGURE 6.5 The calculated fraction of power dissipated by an emitter to different decay channels for different orientation of the emitter's dipole. Adapted from [29].

6.3.2 Detection of SPs with fluorescent molecules

Imaging of SPs is usually done by coupling to the far-field. In a sense, it is a reverse process to the excitation. Again, one has to match the wavevectors k_{sp} and k_0. In a very similar way to the excitation schemes (see Fig. 6.3) SPs can be coupled to far field light by a SNOM tip, by the so-called leakage radiation in Kretschmann or Otto geometry, or by diffraction of SPs on a surface defect or a grating. Another way to

detect SPs is to use fluorescent molecules. If a molecule is placed in the SP near-field, it may be excited. There are several ways how the excited molecule can decay to its initial state. Those include decay through the emission of a photon, fluorescence light, through decay back to SPs or to lossy waves. Detection of SPs is based on the fluorescence decay. The fluorescence light is red shifted with respect to the excitation light, which allows easy filtering from possible background radiation in the system. For successful imaging with molecules several technical issue should be taken into account. Molecules should be deposited in the close proximity of the metal surface. However, direct contact of the molecules to the metal surface has to be avoided as it leads to a complete quenching of the fluorescence. To avoid irreversible photobleaching of the molecules, excitation intensities should be kept relatively low[18,38]. Besides molecules, also Er ions[39] and semiconducting quantum dots can be used to image the SP fields .

7. Excitation, detection and frequency conversion of SPs with molecules

The easiest way to combine fluorescent molecules and plasmonics structures on a chip is by thin film deposition of molecules on the top of thin metal films. Several techniques can be used, e.g., Langmuir-Blodgett films, spin-coating, evaporation etc. These techniques are usually quite straightforward and they allow to control the amount of molecules and in some cases even the distance between a plasmonic structure and molecules. In order to create well defined regions of molecules in pre-defined positions lithography methods should used. In the next section a method, developed in the paper **II.I.** of this thesis, that allows deposition of several different types of molecules on top of a plasmonic waveguide structure is described.

7.1 Fabrication of plasmonic waveguides with molecules

Before positioning the molecules, the 5 μm wide plasmonic silver waveguides and alignment patterns were fabricated by regular e-beam lithography (EBL) and lift-off techniques on a top of an ITO (Indium tin oxide) coated glass. The waveguides

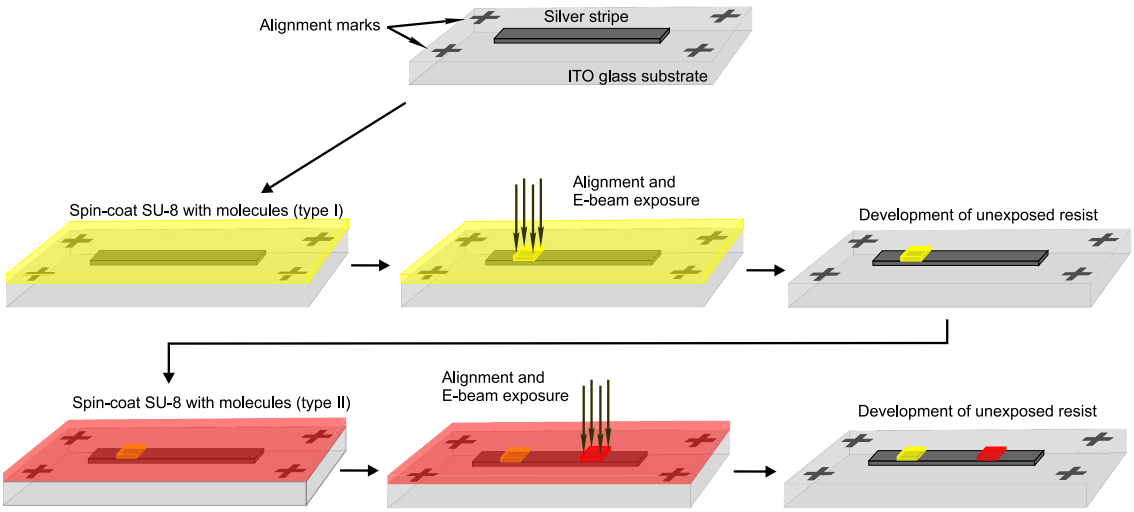

FIGURE 7.1 Fabrication of a plasmonic waveguide with molecules.

consist of a thin adhesion layer (2 nm) of titanium and on top of that a 100-130 nm thick evaporated layer of silver. For positioning, the molecules were mixed with SU-8 epoxy-based polymer resist (Microchem SU-8 2025). SU-8 is a negative resist leaving the exposed area on the chip after EBL. The dye–SU-8 solution was spin

coated on top of the waveguide. To obtain desired thin layers the final solutions were further diluted by a suitable amount of cyclopentanone. The actual thickness was verified by AFM. The immobilization of the dye molecules by e-beam lithography of the SU-8 resist involved a precise alignment step using marks created at the same process step as the waveguide. Finally, the patterning was done on the areas where the dye molecules were intended and the rest of the surface was cleaned using SU-8 developer (Microchem). The fabrication process is schematically presented on Fig. 7.1. The fabrication method is scalable and can be repeated in cycles to position several different molecules, the size and accuracy of positioning of the molecular areas are limited only by the resolution and the alignment accuracy of the lithography technique, which in case of EBL are ∼20 nm and ∼50 nm respectively. Note that use of a positive resist like PMMA, where areas unexposed by the e-beam are left on the surface, can not be used for deposition of several types of molecules in different positions, because a polymer area positioned in the first cycle would be harmed by the exposure during a subsequent cycle. Details for the waveguide fabrication and deposition of molecules are given in Appendix B.

7.2 Coupling between light and surface plasmons using molecules

7.2.1 Plasmon propagation

To realize a full cycle of coupling of far-field light into propagating SPs and SPs back to far-field, Coumarin 30 (C30) and Rhodamine 6G (R6G) were chosen as donor and acceptor molecules respectively. Donor-acceptor pair was chosen in such a way that there is sufficient overlap between emission of donor and absorption of acceptor (see Fig. 7.2). In the used dye-SU-8 solutions the mass percentage of the donor molecule

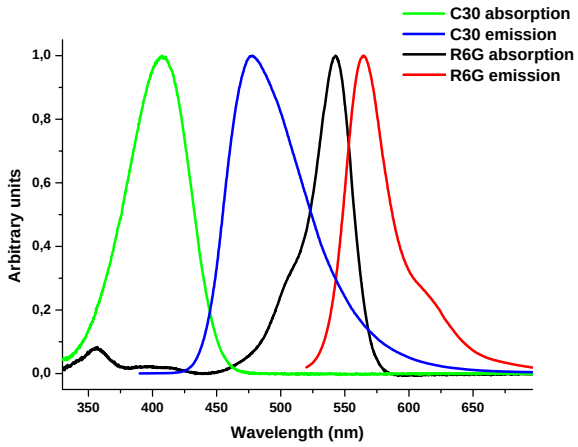

FIGURE 7.2 Absorption and emission spectra of Coumarin 30 and Rhodamine 6G.

C30, of the dry SU-8 resin weight, varied from 2.5 % to 11%, and the mass percentage of the acceptor R6G varied between 2.5 % and 7.9 %. C30 and R6G were positioned on top of the silver stripe as described above. The structure of the sample is shown schematically on Fig. 7.3a). Red squares correspond to the acceptor molecules embedded in SU-8 and cyan area to SU-8 with the donor molecules. The long silver stripe is the waveguide for plasmon propagation and the squares on the sides provide a reference measurement to rule out the contribution from free space propagation. An AFM image of a typical sample is shown in Fig. 7.3b). Confocal mi-

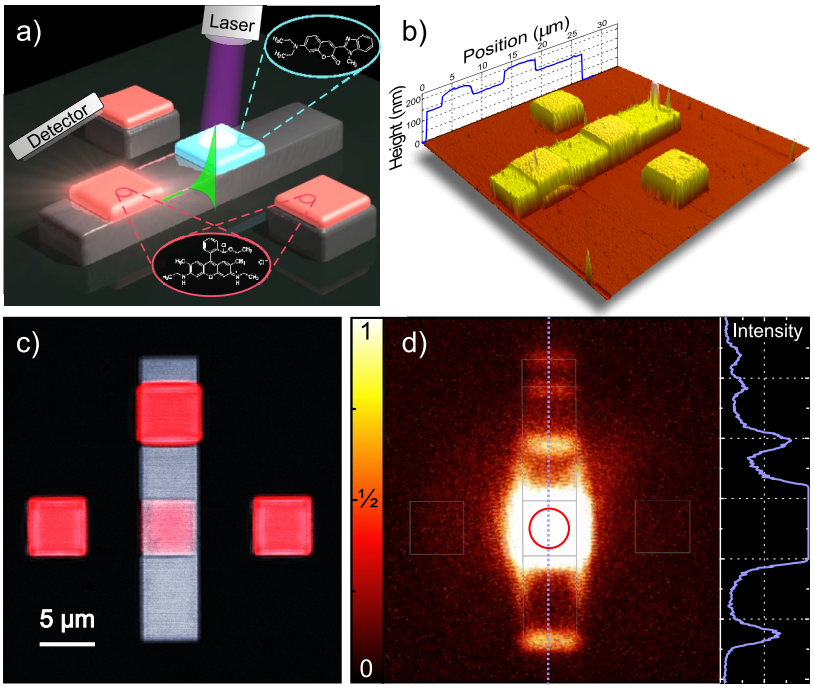

FIGURE 7.3 a) Schematic presentation of the structure of the samples and the measurement. b) Measured AFM image of a typical structure. The height profile along the center of the waveguide is shown on the left. The size of the square regions is 5 x 5 μm^2. c) An image taken with a single scanner setup by scanning the sample with the excitation light and simultaneously collecting data in two channels. d) An image taken with a dual scanner setup where the donor molecules are excited with 405 nm (the red circle corresponds to the area of excitation) and emission with a bandpass of 520-620 nm is collected with a second independent scanner. The contour of the waveguide is overlaid with the intensity map for easy comparison. The intensity profile along the blue dotted line, indicated in the figure, is shown on the right. Adapted from the paper **II.I.** of this thesis.

croscope equipped with a dual scanner (Olympus Fluoview-1000, 100x air objective (NA=0.95)) was used for the measurements. Dual scanner allowed simultaneous excitation of the donor area and detection of light from the acceptor areas. Donor molecules were excited by the diode laser at 405 nm controlled by the first scanner. The excitation laser was kept at low powers (10-100 μW) in order to avoid bleaching of the dye molecules and scanned the selected region (circle with a diameter

of 3-4 μm) in so-called "tornado" mode, i.e. spiral-like motion. The second scanner was used to collect the emission from the whole sample point by point, resulting in a confocal image. The scanning speed for excitation and detection was 10 ms/pixel and 40 ms/pixel, respectively. The size of the measurement area was 800x800 pixels^2 corresponding to the dimensions of 42x42 μm^2. The excitation laser was filtered by a dichroic mirror when the detection bandpass was near the excitation wavelength. Otherwise, a beam splitter was used allowing collection of spectra which were not modified by filters. The emission spectra were recorded with the same instrument by scanning the spectral region in 3 nm steps of 6 nm bandpass.

The first step was to prove that there were propagating plasmons in the system. Figures 7.3c) and 7.3d) show confocal microscope images of a sample. The center of the structure had a 5x5 μm^2 area of donor molecules. The acceptor was placed in the upper, right and left arms of the cross in regions with the dimensions of 5x5 μm^2, while the lower arm had no dye on it. The thickness of the donor layer was 50 nm in all the samples, and in this structure, the thickness of the acceptor layer was 60 nm. Silver stripe connected the upper and lower arms providing a plamonics waveguide channel. The disconnected areas on the sides acted as references. The plasmon propagation was demonstrated by confocal images where scattering from several places along the metal stripe was observed whereas the reference areas, with no metallic connection to the excitation area, showed very little or no signal. The image of the structure in Fig. 7.3c) was taken in the single scanner mode with 488 nm excitation and is combination of images from two detection channels. One of the channels was set to collect the reflection of the excitation laser and provided an image of metal structures (the grey-blue color), the other channel (the red color) was set to collect emission at 520–620 nm corresponding to the emission of the acceptor and also part of the emission spectra of the donor. The Fig. 7.3d) was taken with the dual scanner configuration by exciting the region of the donor with 405 nm laser and simultaneously recording the image with the second scanner. The collection bandpass was 520–620 nm. The signal in the region of the donor was saturated due to direct excitation. A weaker signal was observed in different regions of the plasmonic channel while there was essentially no signal from the reference regions, i.e., left and right arms. The absence of signal in the reference regions rules out free space propagation and indicates that the observed signal originates from propagating SPs. In order to further check the presence of propagating plasmons, samples with varying length (7.5-22.5 μm) between the donor edge and the stripe end were fabricated and the dependence of the intensity of the scattered signal at the end of the stripe on the length was measured. The intensity showed exponential dependence on the length with a characteristic propagation length varying from 7 to 10 μm between different sets of samples. These values are in agreement with the obtained plasmon propagation length of $\sim$20 μm for extended silver at 514 nm and silver-air interface[40]. For 633 nm wavelength and for a stripe width of 5 μm the propagation length is approx-

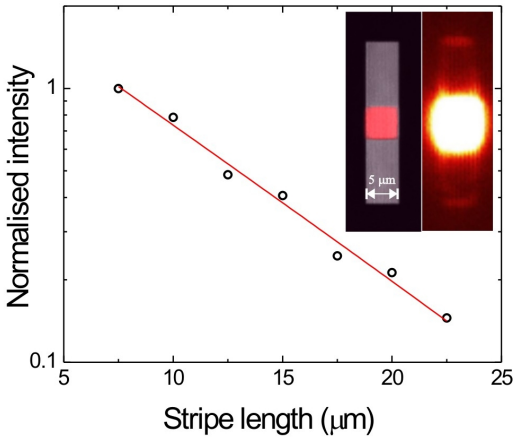

FIGURE 7.4 Intensity of the scattered signal at the end of the stripe as a function of the stripe length (black circles). The red line is the fitted exponential decay yielding propagation length of 7.7 μm. Inset: Confocal microscope images of one of the measured waveguides taken with the single scanner and the dual scanner setups. The waveguide has 10 μm from the edge of the donor (in the middle) to the end of the stripe, where signal from scattered plasmon is clearly visible in the two scanner image. Adapted from the paper **II.I.** of this thesis.

imately half from the value in extended silver. Results from one set of samples are shown in Fig. 7.4.

7.2.2 Incoupling of plasmons by molecules

The fact that the plasmons are exited by the molecules is proven by the spectral information from the emissions as presented in Fig. 7.5. The figure shows a single plasmonic channel with the donor region in the center and the acceptor region in the upper arm. The thickness of the donor layer is 50 nm and the thickness of the acceptor layer is 550 nm. The lower arm contains no acceptor molecules but is otherwise identical to the upper arm. The spectra were taken using the dual scanner setup as described above. Consider first the lower arm. The strongest emission signal is observed at the back edge of the region with SU-8 resist (this region is the same as the acceptor region in the upper arm but without dye molecules). The spectrum of the signal is shown in the inset c) of Fig. 7.5. The spectrum is nearly identical to the spectrum of C30 measured by a direct excitation (shown with a blue line). The emission shown in inset c) originates from scattered SPs (the edge of the SU-8 layer acts as a scattering center), which were exited by the donor molecules. In fact, if no efficient scattering centers are available, most of the emission is lost by dissipation into heat. The donor emission is also visible in the upper arm of the structure, although there the acceptor contribution is visible as well, as discussed in detail below. Further information about coupling of the donor molecules to SPs was obtained by investigating the effect of an additional spacer layer of SU-8 polymer between the metal

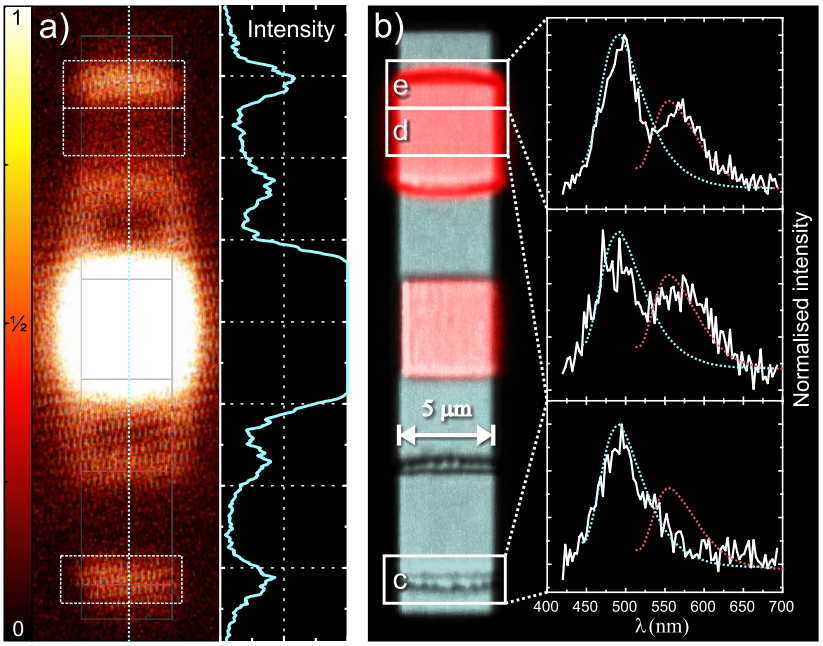

FIGURE 7.5 Confocal microscope images of a plasmonic channel. a) An image obtained by a dual scanner measurement where the excitation was only on the donor area in the middle and the collection was scanned over the sample, showing plasmon propagation as the scattered light along the metal stripe. The donor molecules were located in the center of the rectangular region, and the acceptor molecules in the upper arm. The SU-8 structure without dye molecules in the lower arm served as a reference. The intensity profile along the blue dotted line is shown on the right. b) The spectra measured at different regions under excitation of the donor with 405 nm laser are shown in the insets c)-e). The reference spectra of the donor (blue) and acceptor (red) measured by direct excitation are shown for comparison. The donor spectra was observed far away from the excitation region and that is a signature of excitation decay to the plasmons, and the acceptor spectra demonstrate molecular energy transfer via surface plasmons over the ten micrometer long distance. Adapted from the paper **II.I.** of this thesis.

and the donor layer. The results of the experiments are shown in Fig. 7.6. Three samples were prepared with otherwise similar structures but sample a) contained no metal, sample b) had a donor layer directly on the metal film and sample c) had additionally a spacer layer with a thickness of 40 nm between the metal and the donor layer. All the samples were measured under the same excitation and collection conditions. Comparing the sample a) and sample b) shows a small increase of the emission intensity from the donor molecules in the sample b). However, adding the spacer layer increases the emission intensity from the donor region strongly as can be seen by comparing the samples b) and c). This effect can be explained by the efficient coupling of excited donors to SPs (or at least partly to lossy waves) in b) which decreases the emission intensity to the far field. The thickness of the spacer layer corresponds to a distance within which the molecules are strongly coupled to

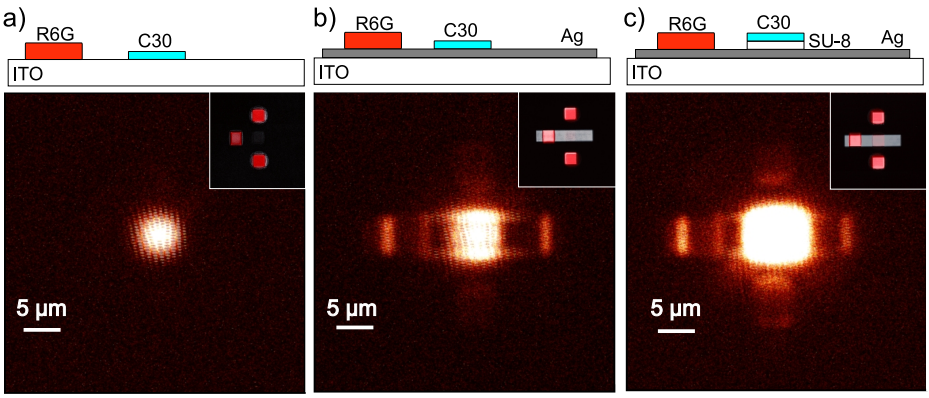

FIGURE 7.6 The effect of the spacer layer between the donor and the metal on the emission intensity. a) A sample without any metal layer but with donor region in the center and acceptor regions in the three arms. The right arm has no dye. b) Similar to a) but with a plasmonic channel added. c) similar to b) but with a spacer layer of 40 nm thickness added between the donor and the metal. Images are takes in dual scanner configuration with 405 nm excitation scanner localized on the donor region and imaging scanner set to the detection bandpass of 520–620 nm including both donor and acceptor emission. The height of the donor layer was 50 nm and the height of the acceptor layer is 550 nm. In the insets: confocal images are shown with gray-blue showing the reflection image and red showing the acceptor and donor emission image (488 nm excitation and 520–620 nm bandpass detection).

SPs. Adding the spacer layer decreases the coupling with resulting increase of the emission intensity to the far field, as seen in c). The increase of the emission intensity of donors from sample a) to sample c), which both have molecules away from the metal surface, can be explained by a mirror effect increasing the efficiency of excitation and collection of the far-field light.

7.2.3 Outcoupling of plasmons by molecules

Outcoupling of the plasmons via molecules is shown by the spectra in Fig. 7.5b), insets d) and e). The polymer matrix in the upper arm of the structure contains acceptor molecules. The strongest emission signal appears at the back edge of the rectangular acceptor region but some intensity is also observed in the center. In both cases, the spectrum is composed of spectra of both the donor and the acceptor as can be seen by comparison with the emission spectra of directly excited donor and acceptor. The relative contribution of the acceptor is strongest in the spectra measured at the center of the acceptor region, but at the edge its contribution is also substantial. The absolute intensity of the total emission in the center of the acceptor region d) is lower than at the edge e) as can be seen from Fig. 7.5a). In the center of the acceptor area d) the emission with the donor spectra could originate from scattering of SPs from the imperfections of the polymer area. The remaining interesting questions are what are the mechanisms of the acceptor excitation, and acceptor emission

to the far field? It is plausible that most of the acceptor excitation is caused directly by SPs. Then what about the acceptor emission? It could be either direct emission to the far field from the molecules excited by SPs, or surface plasmon coupled emission (SPCE) in the sense that the acceptors, after being excited by SPs, may emit back to plasmons which consequently scatter from the edges of the polymer region. Based on the fact that the acceptor emission is stronger at the edge of the acceptor region (also evident from Fig. 7.5a) and from the relative strength of the donor and acceptor emission) it can be concluded that the majority of the emission from the acceptor is SPCE. It is reasonable to expect that those molecules which are excited by the SPs can also be coupled back to SPs (the effect is explained in detail in Section 7.3). Therefore, one can expect to observe considerable SPCE at the scattering centers. In any case, the observation of the acceptor emission clearly shows that the initial excitation by 405 nm light is coupled to the SPs via donor molecules, followed by propagation of SPs over $\sim$10 μm and excitation of acceptors, thus demonstrating molecular coupling and plasmonic energy transfer.

7.2.4 Efficiency of the energy transfer

Unfortunately it was not possible to get quantitative data on the efficiencies of different steps of the energy transfer from the experimental data presented above. However, some estimates can be done. First, the absorption in the donor layer can de estimated in the following way. According to literature data Coumarine 30 has a molar absorption coefficient of 42740 $M^{-1}cm^{-1}$ at 405 nm[41]. Using this value for a typical sample with a thickness of 50 nm and a concentration of 5% (by weight) yields that 15.6% of the excitation intensity is absorbed. In this estimation the optical path length is multiplied by a factor of two due to a reflecting metal surface. The quantum yield for fluorescence adds another factor of 0.67 for the efficiency. In a favorable case the coupling efficiency to plasmons can be of the order of 70%. The propagation length of SPs is taken from the measurement (see Fig. 7.4) to be 10 μm yielding a factor of 0.368 for a 10 μm long stripe. At this point the estimation shows that about 2.7% of the initial intensity has been transferred to the acceptor site.

Next we calculate absorption in the acceptor layer. From the emission spectrum of Coumarine 30 and molar absorption coefficient data for Rhodamine 6G, it can be estimated that along the 5 μm long acceptor area, 72.3% of the SPs intensity is absorbed. Altogether, our simple estimation gives that about 2% of the initial laser power is absorbed in the acceptor region. Of course there are many unknown factors which were not taken into account in this estimation, such as effect of SPs on the absorption and emission efficiencies, variation of fluorescence quantum yield with distance from the surface, scattering of light from the surfaces and scattering of SPs from the surface imperfections, emission of SPs to the substrate and extension of SP field out of the acceptor layer. Therefore, the obtained number represents rather a

best case scenario but nevertheless a realistic one.

7.3 Frequency conversion of propagating plasmons

As was mentioned above, molecules which are excited by SPs can decay back to SPs. This process can be used to manipulate the frequency of propagating SPs. The operation principle of the frequency converter is shown schematically in Fig. 7.7a). SPs were launched into a microscale plasmon waveguide by a SPP source consist-

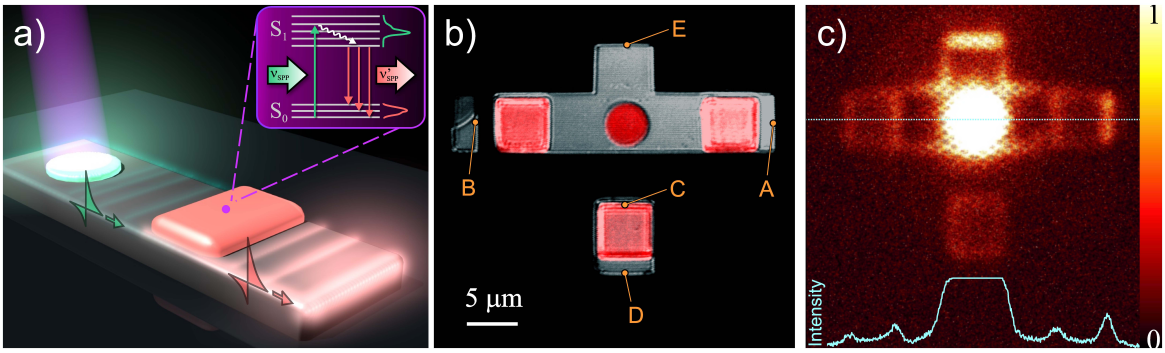

FIGURE 7.7 a) Schematics of the frequency conversion. SPs are launched by the SP source (cyan circle) and propagate along the waveguide to the conversion area (red square) with the converter molecules embedded. SPs are represented in the image as light with corresponding color and by an electric field distribution drawn at the edges of the silvery waveguide. The inset shows a schematic energy diagram of excitation of a converter molecule by SPs in the conversion area and the coupling back to SPs. At the end of the waveguide, SPs are scattered to far field. b) An image taken by scanning the sample with the excitation light (λ=488 nm) and simultaneously collecting data in two channels. First channel: the gray-blue color corresponds to the reflection image showing the metallic waveguide. Second channel overlaid with the first one: the red color corresponds to a collection band that includes emission from R6G (the red squares) and partly from the C30 (the red circle). The letters correspond to the positions from where the spectra are recorded during the conversion experiment. c) A plasmon image of the same sample taken with a dual scanner setup where the C30 area in the middle is excited with 405 nm, and emission with a bandpass of 500–600 nm is collected with a second independent scanner. The intensity profile along the blue dotted line is shown below the image. Adapted with permission from the paper **II.II.** of this thesis.

ing of fluorescent Coumarine 30 (C30) molecules or, alternatively, semiconducting quantum dots (QDs) deposited at close proximity to the waveguide surface and excited by 405 nm laser light. The waveguide was a 5 μm wide silver stripe of $\sim$130 nm thickness. The emerged SPs had a distinct spectrum of the emitters used as the SP source, i.e., maxima near λ=480 nm for C30 and λ=550 nm for QDs. After excitation, the SPs propagated along the waveguide reaching the area of the converter molecules, Rhodamine 6G (R6G) for C30 or Sulforhodamine 101 (SR101) for QDs.

The SP donor and the SP convertor pairs were chosen such that there was an overlap between the donor emission and convertor absorption spectra. Thus, the convertor molecules were exited by the SPs. Consequently, the exited converter molecule decayed nonradiatively via vibrational relaxation to the bottom of the electronic excited state, as shown in the inset of Fig. 7.7a). Then the excited state could decay by emitting free space light or couple back to the waveguide as a lossy wave or a SP with a spectrum that is characteristic for the convertor molecules. The converted SPs further propagated to the end of the waveguide. The edge of the waveguide served as an efficient scattering center of SPs to far field. The typical sample used in the experiments is shown in Fig. 7.7b). Samples were fabricated using e-beam lithography and characterized using dual scanner confocal microscope as descried above.

Figure 7.7c) shows a "plasmon image" of the sample taken with a dual scanner setup where the C30 area in the middle is excited with 405 nm, and emission with a bandpass of 500–600 nm is collected with a second independent scanner. As one can see the signal from the region of the SP source is saturated due to direct excitation. However, a clear signal is observed in different regions of the waveguide arms. There is no plasmonic channel connected to the lower R6G region, which is manifested by significantly weaker signal caused by far field excitation of R6G by the C30 emission directly through a small solid angle or via scattering in the setup. It is also

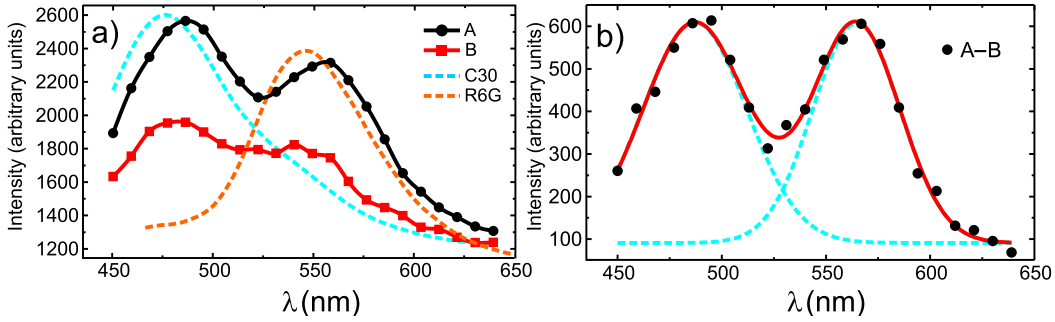

FIGURE 7.8 a) Spectra recorded from the positions shown in Fig. 7.7: A (black circles) and B (red squares). Cyan and orange dashed lines are the emissions of pure C30 and R6G, respectively. b) Spectrum of A (black circles) after the subtraction of the spectrum of B, the far-field contribution. Red line is a fit to the data as a sum of two Gaussian peaks (blue dotted lines) corresponding to the emissions of C30 (480 nm) and R6G (530 nm). Adapted with permission from the paper **II.II** of this thesis.

seen that the SPs are efficiently scattered from the edges of the waveguides, as well as from the edges of the SU-8 regions. The spectra recorded from positions A and B while exciting C30 are shown in Fig. 7.8a), together with reference emission spectra of C30 and R6G. The spectra shown are averaged from 2-5 measurements. The spectrum of A clearly shows a combination of C30 and R6G emissions. However, even though B is disconnected from the waveguide, there is a clear contribution of R6G in the spectrum recorded at B, which indicates that the R6G excited by SPs has

also far field emission to B. This emission consists of direct far-field emission of the converter molecule and also of scattering of the converted SPs from the end of the conversion region. Both of these contributions are scattered to the detector by the silver edge at position B. Due to the symmetry of the sample, the same far-field contribution can be assumed to be present also in position A. One can thus obtain the pure plasmonic spectrum of A by subtracting the intensity at B from the intensity at A. Note that the spectrum of B contains also converted SPs that are scattered from the end of the waveguide; therefore, the subtraction gives a minimum estimate of SP intensity at A. The spectrum of A after the subtraction is shown in Fig. 7.8b). In order to obtain the contributions of C30 and R6G in the emission, two Gaussian peaks were fitted to the spectrum in Fig. 7.8b) and integrated separately corresponding to C30 and R6G intensities. This yielded 45%/55% distribution between R6G and C30, respectively. Thus the total SPs conversion efficiency of ∼45% was obtained, which is comparable to the efficiencies obtained when using nanoparticle-localized surface plasmons to enhance conversion of far field light[42].

Frequency conversion was also tested for samples that used quantum dots as the SPs source and Sulforhodamine 101 (SR101) dye as a convertor. QDs are more stable with respect to bleaching. The bleaching time of QDs was observed to be over an order of magnitude longer than that of C30.

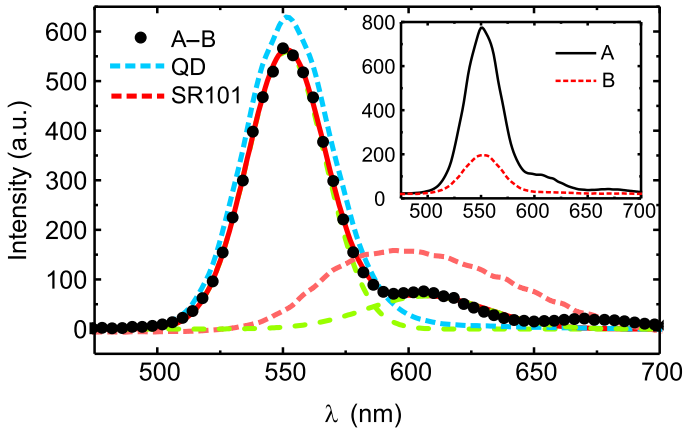

FIGURE 7.9 Frequency conversion for QD Sulforhodamine pair. SP spectrum of A (black circles), i.e., the spectrum of B subtracted from the spectrum of A. The red line is a fit to the data as a sum of two Gaussian peaks (green dotted lines) corresponding to the emissions of QD (565 nm) and SR101 (600 nm). Cyan dotted and red dashed line are the emissions of pure QD and SR101, respectively. Inset shows the spectra recorded from A (black solid) and B (red dashed). Adapted with permission from the paper **II.II** of this thesis.

The QDs (Invitrogen, Qdot® 565 ITK™ amino) and SR101 have the emission maxima at λ=550 nm and λ=600 nm respectively. Similar analysis as above yielded 15% conversion (see Fig. 7.9). The lower conversion efficiency is probably due to the smaller overlap between the QD emission and the SR101 absorption. Semiconduct-

ing quantum dots could have an interesting application in plasmonics. Due to broad absorption of QD, one could think about building plasmonic multiplexer that would convert of a large band into a single frequency. This is complementary to molecules that typically convert one narrow band into another.

8. Conclusions

In this part of the thesis it was demonstrated how fluorescent molecules can be used to fabricate basic plasmonic devices. A new method for deposition of molecules on plasmonic structures was developed. The method allows positioning of several types of molecules with high accuracy and resolution, and could be easily scaled to the nanoscale dimension without any fundamental restrictions. It was shown that molecules can be used as couplers between far-field light and surface plasmons. Energy transfer from donor to acceptor molecules over distances of the order of 10 μm was observed. Moreover, it was shown that fluorescent molecules can be used to manipulate the properties of SPs, i.e., to convert the frequency of propagating plasmons. The presented experiments are a proof-of-principle of fundamental concepts for molecular plasmonics: plasmonic waveguide in which input, output and simple passive element (frequency convertor) are realized with molecules. The use of molecules offers the prospect of integration with molecular electronics and the use of molecular self-assembly in fabrication.

References

[1] Ritchie, R. H. "Plasma losses by fast electrons in thin films". *Phys. Rev.* **106**, 874 (1957).

[2] Barnes, W. L., Dereux, A., and Ebbesen, T. W. "Surface plasmon subwavelength optics". *Nature* **424**, 824 (2003).

[3] Van Duyne, R. P. "Molecular plasmonics". *Science* **306**, 985 (2004).

[4] Zheng, Y. B., Yang, Y.-W., Jensen, L., Fang, L., Juluri, B. K., Flood, A. H., Weiss, P. S., Stoddart, J. F., and Huang, T. J. "Active molecular plasmonics: Controlling plasmon resonances with molecular switches". *Nano Lett.* **9**, 819 (2009).

[5] Lakowicz, J. R. "Radiative decay engineering 5: metal-enhanced fluorescence and plasmon emission". *Anal. Biochem.* **337**, 171 (2005).

[6] Zayats, A. V., Smolyaninov, I. I., and Maradudin, A. A. "Nano-optics of surface plasmon polaritons". *Phys. Rep.* **408**, 131 (2005).

[7] Atwater, H. "The promise of plasmonics". *Sci. Am.* **296**, 56 (2007).

[8] Maier, S. A. *Plasmonics: Fundamentals and Applications*. Springer, 1 edition, May (2007).

[9] Ozbay, E. "Plasmonics: Merging Photonics and Electronics at Nanoscale Dimensions". *Science* **311**, 189 (2006).

[10] Weeber, J.-C., Krenn, J. R., Dereux, A., Lamprecht, B., Lacroute, Y., and Goudonnet, J. P. "Near-field observation of surface plasmon polariton propagation on thin metal stripes". *Phys. Rev. B* **64**, 045411 (2001).

[11] Steinberger, B., Hohenau, A., Ditlbacher, H., Stepanov, A. L., Drezet, A., Aussenegg, F. R., Leitner, A., and Krenn, J. R. "Dielectric stripes on gold as surface plasmon waveguides". *Appl. Phys. Lett.* **88**, 094104 (2006).

[12] Bozhevolnyi, S. I., Volkov, V. S., Devaux, E., Laluet, J., and Ebbesen, T. W. "Channel plasmon subwavelength waveguide components including interferometers and ring resonators". *Nature* **440**, 508 (2006).

[13] Smolyaninov, I. I., Hung, Y.-J., and Davis, C. C. "Surface plasmon dielectric waveguides". *Appl. Phys. Lett.* **87**, 241106 (2005).

[14] Ditlbacher, H., Hohenau, A., Wagner, D., Kreibig, U., Rogers, M., Hofer, F., Aussenegg, F. R., and Krenn, J. R. "Silver nanowires as surface plasmon resonators". *Phys. Rev. Lett.* **95**, 257403 (2005).

[15] Sanders, A. W., Routenberg, D. A., Wiley, B. J., Xia, Y., Dufresne, E. R., and Reed, M. A. "Observation of plasmon propagation, redirection, and fan-out in silver nanowires". *Nano Lett.* **6**, 1822 (2006).

[16] Liu, Z., Steele, J. M., Srituravanich, W., Pikus, Y., Sun, C., and Zhang, X. "Focusing surface plasmons with a plasmonic lens". *Nano Lett.* **5**, 1726 (2005).

[17] Yin, L., Vlasko-Vlasov, V. K., Pearson, J., Hiller, J. M., Hua, J., Welp, U., Brown, D. E., and Kimball, C. W. "Subwavelength focusing and guiding of surface plasmons". *Nano Lett.* **5**, 1399 (2005).

[18] Ditlbacher, H., Krenn, J. R., Schider, G., Leitner, A., and Aussenegg, F. R. "Two-dimensional optics with surface plasmon polaritons". *Appl. Phys. Lett.* **81**, 1762 (2002).

[19] Volkov, V. S., Bozhevolnyi, S. I., Devaux, E., Laluet, J.-Y., and Ebbesen, T. W. "Wavelength selective nanophotonic components utilizing channel plasmon polaritons". *Nano Lett.* **7**, 880 (2007).

[20] Weeber, J.-C., González, M. U., Baudrion, A.-L., and Dereux, A. "Surface plasmon routing along right angle bent metal strips". *Appl. Phys. Lett.* **87**, 221101 (2005).

[21] Drezet, A., Koller, D., Hohenau, A., Leitner, A., Aussenegg, F. R., and Krenn, J. R. "Plasmonic crystal demultiplexer and multiports". *Nano Lett.* **7**(6), 1697 (2007).

[22] Pyayt, A. L., Wiley, B., Xia, Y., Chen, A., and Dalton, L. "Integration of photonic and silver nanowire plasmonic waveguides". *Nat. Nanotechnol.* **3**, 660 (2008).

[23] Kretschmann, E. and Raether, H. "Radiative decay of non-radiative surface plasmons excited by light". *Z. Naturforsch. A* **23a**, 2135 (1968).

[24] Pala, R. A., Shimizu, K. T., Melosh, N. A., and Brongersma, M. L. "A nonvolatile plasmonic switch employing photochromic molecules". *Nano Lett.* **8**(5), 1506 (2008).

[25] Pacifici, D., Lezec, H. J., and Atwater, H. A. "All-optical modulation by plasmonic excitation of CdSe quantum dots". *Nat. Photonics* **1**, 402 (2007).

[26] Andrew, P. and Barnes, W. L. "Energy transfer across a metal film mediated by surface plasmon polaritons". *Science* **306**, 1002 (2004).

[27] Maier, S. A., Kik, P. G., Atwater, H. A., Meltzer, S., Harel, E., Koel, B. E., and Requicha, A. A. "Local detection of electromagnetic energy transport below the diffraction limit in metal nanoparticle plasmon waveguides". *Nat. Mater.* **2**, 229 (2003).

[28] Gunn, J. M., Ewald, M., and Dantus, M. "Polarization and phase control of remote surface-plasmon-mediated two-photon-induced emission and waveguiding". *Nano Lett.* **6**, 2804 (2006).

[29] Barnes, W. L. "Fluorescence near interfaces: the role of photonic mode density". *J. Mod. Opt.* **45**, 661 (1998).

[30] Ritchie, G. and Burstein, E. "Luminescence of dye molecules adsorbed at a Ag surface". *Phys. Rev. B* **24**, 4843 (1981).

[31] Glass, A. M., Wokaun, A., Heritage, J. P., Bergman, J. G., Liao, P. F., and Olson, D. H. "Enhanced two-photon fluorescence of molecules adsorbed on silver particle films". *Phys. Rev. B* **24**, 4906 (1981).

[32] Kneipp, K., Kneipp, H., Itzkan, I., Dasari, R. R., and Feld, M. S. "Ultrasensitive chemical analysis by raman spectroscopy". *Chem. Rev.* **99**, 2957 (1999).

[33] Chance, R. R., Prock, A., and Silbey, R. *Molecular Fluorescence and Energy Transfer Near Interfaces*, volume 37 of *Advances in Chemical Physics*. (2007).

[34] Hobson, P., Wedge, S., Wasey, J., Sage, I., and Barnes, W. "Surface plasmon mediated emission from organic light-emitting diodes". *Adv. Mater.* **14**, 1393 (2002).

[35] Okamoto, K., Niki, I., Shvartser, A., Narukawa, Y., Mukai, T., and Scherer, A. "Surface-plasmon-enhanced light emitters based on InGaN quantum wells". *Nat. Mater.* **3**, 601 (2004).

[36] Koller, D., Hohenau, A., Ditlbacher, H., Galler, N., Reil, F., Aussenegg, F., Leitner, A., List, E., and Krenn, J. "Organic plasmon-emitting diode". *Nat. Photonics* **2**, 684 (2008).

[37] Lakowicz, J. R. "Radiative decay engineering 3. surface plasmon-coupled directional emission". *Analytical Biochemistry* **324**, 153 (2004).

[38] Ditlbacher, H., Krenn, J. R., Felidj, N., Lamprecht, B., Schider, G., Salerno, M., Leitner, A., and Aussenegg, F. R. "Fluorescence imaging of surface plasmon fields". *Appl. Phys. Lett.* **80**, 404 (2002).

[39] Verhagen, E., Kuipers, L., and Polman, A. "Enhanced nonlinear optical effects with a tapered plasmonic waveguide". *Nano Lett.* **7**, 334 (2007).

[40] Lamprecht, B., Krenn, J. R., Schider, G., Ditlbacher, H., Salerno, M., Felidj, N., Leitner, A., Aussenegg, F. R., and Weeber, J. C. "Surface plasmon propagation in microscale metal stripes". *Appl. Phys. Lett.* **79**, 51 (2001).

[41] Du, H., Fuh, R. A., Li, J., Corkan, L. A., and Lindsey, J. S. "PhotochemCAD: A computer-aided design and research tool in photochemistry". *Photochemistry and Photobiology* **68**, 141 (1998).

[42] Yeh, D.-M., Huang, C.-F., Lu, Y.-C., and Yang, C. C. "White-light light-emitting device based on surface plasmon-enhanced CdSe/ZnS nanocrystal wavelength conversion on a blue/green two-color light-emitting diode". *Appl. Phys. Lett.* **92**, 091112 (2008).

Part III

Appendices

A. Materials and methods (DNA related studies)

A.1 Nanoelectrodes fabrication

Electrodes were fabricated using standard electron beam lithography. Slightly boron-doped (100)-silicon wafer, with 200 nm thermally grown SiO_2 at the top as a passivation layer, was used as a substrate. For a mask polymethylmethacrylate (Microchem A2 PMMA) was spin-coated with 2000-2500 rpm and baked for 5 min on a hot plate (160 ^oC). Patterning was done by scanning electron microscope (SEM) LEO 1430+ equipped with Raith Elphy Plus lithography software was used for fabrication of electrodes for single DNA molecule trapping and Raith eLine was used for the fabrication of electrodes for DNA origami trapping. After patterning the resist was developed by immersing the sample in a mixed (1:3) solution of methyl-iso-butylketon (MIBK) and isopropyl alcohol (IPA) for about 30 seconds at room temperature (22 ^oC). After that the sample was rinsed with IPA . Undeveloped residues from mask openings were removed using a short oxygen flash in reactive ion etcher (Oxford Plasmalab 80 Plus RIE). The metal evaporation took place in an ultrahigh vacuum (UHV) chamber, pressure being of the order of 10^{-8} mbar during the evaporation. The thickness of the evaporated gold layer was 15-20 nm, under which 1-2 nm of titanium was used as an adhesion layer. After evaporation, the PMMA mask was removed by lift-off in hot acetone. PMMA residues were removed from the substrate using oxygen plasma. For the experiments on trapping single DNA molecules the electrodes were $\sim$100 nm wide with $\sim$100 nm gap between them. For DNA origami trapping the electrode width near the gap was $\sim$20 nm and the width of the gap was $\sim$80 nm.

A.2 Carbon nanotube electrode fabrication

The nanostructure containing gold electrode as a one and a multi-walled carbon nanotube (MWCNT) as another electrode was fabricated by two-step e-beam lithography with nanoscale pattern alignment and an AFM imaging in between. In the first e-beam lithography step, a metallic mark grid was patterned with LEO 1430+ SEM on the 300 μm thick silicon wafer containing 700 nm thick low-pressure chemical vapor deposition (LPCVD) grown Si_3N_4 on both sides. The grid was fabricated using a two layer PMMA resist: 11% PMMA in Ethyl Lactate was spinned using 6000 rpm and baked for 2 minutes on hot plate(160 ^oC), and on top of it 2% PMMA in Anisole was spinned using 3000 rpm and baked for 2 minutes. The resist was developed for 30 seconds in MIKB:IPA (1:2) and 30 seconds in methyl glycol:methanol (1:2), then flushed with IPA and finally He dried. Metallization (5 nm Ti and 15 nm Au) was done as in the previous section. A mixture of MWCNTs in powder form, obtained from the research group of S. Iijima, was dissolved in 1,2-dichloroethane by diluting and sonicating several times to unravel the intrinsically formed nanotube clumps until the solution was ho-

mogeneous. Several drops of the CNT-solution were spun on the substrate using 3000 rpm. Tubes were located on the surface by imaging with AFM and/or SEM (LEO 1430+). In the second lithography step, the prefabricated mark grid was used for the stage alignment to make electrical contacts to the nanotubes located by AFM imaging. Metallization was done as above.

A.3 Fabrication of DNA fragments and thiol-modified DNA

DNA fragments of lengths varying from 27 bp to 8 kbp were fabricated by three different methods: 1) 27 bp fragments – by annealing of synthetic oligonucleotides. 2) 145 and 444 bp fragments – using PCR (Polymerase Chain Reaction). 3) 1065, 5141 and 8461 bp fragments – using a restriction enzyme digestion of plasmids multiplied in bacteria. The obtained concentrations were measured spectrophotometrically. All fragments (except 27 bp fragment) were eluted to Hepes/NaOH buffer, i.e., 3 mM Hepes and 1 mM NaOH, and stored in a refrigerator in small aliquots.

TABLE A.1 The oligos used as primers for PCR

Name	Base sequence
Primer1	GGT GAA TTC GCC GGC ACC TAC ATC ACA
Primer2	TGT GAT GTA GGT GCC GGC GAA TTC ACC
Primer3	CCC GAT GGT CAT GTT GGC GCC CAG ATC GTT GGT
Primer4	CTG CTA GAT CTA TGG TGC ACG CAA CCT CCC C
Primer5	GAG TGA AGA TGA TGA TGC CGA CC
Primer6	HS-$(CH_2)_6$-GCC AGA AAG TGC TCG CTG AC
Primer7	HS-$(CH_2)_6$-TTC TCG ACA AGC TTT GCG GG
Primer8	DTPA-GCC AGA AAG TGC TCG CTG ACT G
Primer9	DTPA-CTT CTC GAC AAG CTT TGC GGG

27 bp fragments were made by mixing stoichiometric amounts of complementary oligonucleotides (TAGC, Copenhagen, Denmark) *Primer1* and *Primer2* (see Table A.1) in 6.5 mM Hepes buffer (pH 7.0 adjusted with NaOH) and heating the solution to 70 ^{o}C for 5 minutes and then cooling it at room temperature. 145 and 444 bp DNA fragments were produced by PCR reaction using TAQ polymerase (Fermentas) with oligonucleotides *Primer3* and *Primer4* or *Primer4* and *Primer5*, respectively, as primers in PCR reaction. The PCR product was subjected to 1% agarose gel electrophoresis and extracted with GFXTM PCR, DNA and Gel Band Purification Kit (Amersham Biosciences). Chicken avidin complementary DNA in pFastBac1-plasmid (Invitrogen) was used as a template in the PCR reaction.

1 kbp DNA fragments were generated by digesting the pBVboostFG plasmid using BglI and SpeI restriction enzymes. 5 kbp fragments were produced by linearizing pFASTBAC1 plasmid (Invitrogen) containing chimeric avidin expression construct using HindIII enzyme. 8 kbp fragments were generated by linearizing pBVboostFG containing modified avidin expression construct using ApaI enzyme. The restriction enzymes were from Promega.

Fragments were purified as explained above in the case of PCR products. Plasmids were produced by cultivating transformed *E. coli* JM109 cell line (Stratagene) at 37 °C in suspension and isolating the plasmids from overnight cultures by using plasmid purification kit (Macherey-Nagel, Düren, Germany). Two different types of chemical DNA-modifications,

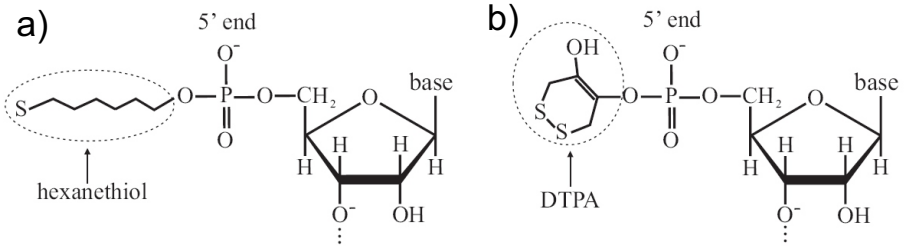

FIGURE A.1 a) Hexanethiol- and b) DTPA-modification in the 5′ end of the oligonucleotide.

i.e., hexanethiol (HS-$(CH_2)_6$) and DTPA (dithiol-phosphoramidite), were used (see Fig. A.1) to attach DNA molecules to electrodes. dsDNA containing a modification group in the both ends of the molecule was obtained by using 5′-modified oligonucleotides as primers in PCR (see Table A.1). Oligonucleotide *Primer6* (purchased from Synthegen, Houston, Texas) was used as a forward primer and *Primer7* as a reverse primer for hexanethiol-modified 414 bp DNA (C6-DNA). Oligonucleotide *Primer8* (purchased from TAG Copenhagen A/S) was used as a forward primer and *Primer9* as a reverse primer for DTPA-modified 415 bp DNA (DTPA-DNA). The PCR was done as above.

A.4 Preparation of DNA solution

Prior to a labelling and use in DEP studies, the DNA fragments were diluted into Hepes/NaOH buffer, which has pH 6.9 and conductivity 20 μS/cm. For confocal microscopy, the DNA was labelled with double-stranded DNA specific fluorescent label PicoGreen (Molecular Probes, Eugene, USA). PicoGreen stock solution was first diluted 1:100 into Hepes/NaOH buffer and then mixed 1:1 with the DNA solution to obtain the final solution, i.e., 1:200 diluted PicoGreen into Hepes/NaOH buffer. The final concentrations of the fragments were chosen so that the concentration of the nucleotides remained the same in all cases. The fluorescent dye molecules attach approximately uniformly along the double helix, which ideally results in the same amount of fluorescence in the solutions of DNA molecules of different length. The final concentration of PicoGreen was 1.6 μM yielding a dye to base pair ratio of 1:5.

For DNA immobilization experiments performed in situ under confocal microscope, 10 nM solutions of C6-DNA and DTPA-DNA diluted into Hepes/NaOH buffer were used. Unlike in the case of unmodified DNA fragments, for thiol-modified DNA the reduction agents were used (in some cases) to break sulphur-sulphur bonds formed between separate DNA molecules and to make thiol-groups more reactive. The reduction agent, either TCEP-HCl (Tris(2-Carboxyethyl)Phosphine and Hydrochloride) or $NaHB_4$ (Sodium Borohydride),

was first added to Hepes/NaOH buffer in which the DNA solution was then diluted to and kept about 1 h before the DEP experiment for the reduction to take place. Also, some experiments were performed without using a reductive agent at all. Prior to the experiments 1.6 μM PicoGreen was added as above.

A.5 Charging effects

The measuring set-up can be modeled by the circuit presented on Fig.A.2a). R_{system} is the resistance of the cables and connectors, C_{system} is the capacitance of the sample. The bias voltage changes in steps and the current is measured after the settling time τ (see Fig.A.2b)). Let us consider a voltage sweep down with initial voltage V_0, voltage step V_τ, and stabiliza-

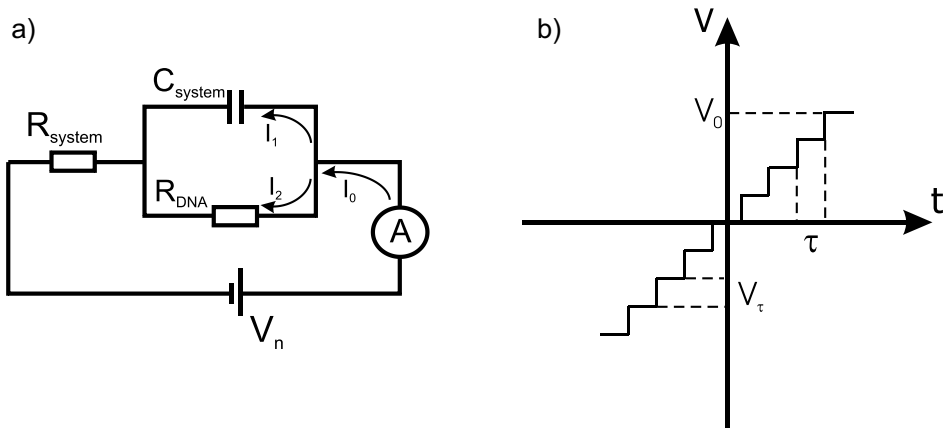

FIGURE A.2 a) Equivalent circuit of measurement set-up. b) Etep-like voltage sweep.

tion time τ. For convenience, in all the equations C_{system} will be denoted as C_s, R_{system} as R_s and R_{DNA} as R_0. The equivalent circuit on Fig.A.2a) can be described by the system of equations

$$\begin{cases} q/C_s = R_0 I_2 \\ I_1 + I_2 = I_0 \\ I_0 R_s + I_2 R_0 = V_n \\ I_1 = dq/dt. \end{cases} \tag{A.1}$$

Here q is the charge of the capacitor. From this system, the differential equation for the time dependent charge of the capacitor can be derived

$$\frac{dq}{dt} + q\left(\frac{1}{C_s R_0} + \frac{1}{C_s R_s}\right) = \frac{V_n}{R_s}. \tag{A.2}$$

For the time interval $0 < t < \tau$ (first step in voltage sweep), the solution of Equation A.2 is

$$q_1 = C_1 e^{-\lambda t} + V_1 \frac{1}{\lambda R_s}. \tag{A.3}$$

Here $\lambda = \frac{1}{C_s R_0} + \frac{1}{C_s R_s}$, $V_1 = V_0 - V_\tau$. The constant C_1 can be found from the condition $q_1 = V_0 C_s$ at the time moment $t = 0$, thus

$$C_1 = V_0 \left(C_s - \frac{1}{\lambda R_s} \right) + \frac{V_\tau}{\lambda R_s}. \tag{A.4}$$

For the time interval $\tau < t < 2\tau$ the charge of the capacitor is

$$q_2 = C_2 e^{-\lambda(t-\tau)} + V_2 \frac{1}{\lambda R_s}. \tag{A.5}$$

Here $V_2 = V_0 - 2V_\tau$ and the constant C_2 is defined by the condition

$$q_2(t = \tau) = q_1(t = \tau) = C_1 e^{-\lambda \tau} + \frac{V_1}{\lambda R_s}. \tag{A.6}$$

It can be easily seen that for the time interval $(n-1)\tau < t < n\tau$ that corresponds to n^{th} step, the charge of the capacitor is given by

$$q_n = C_n e^{-\lambda(t-(n-1)\tau)} + V_n \frac{1}{\lambda R_s}. \tag{A.7}$$

Where $V_n = V_0 - nV_\tau$, and the constant C_n is given by the iteration relation

$$C_n = C_{n-1} e^{-\lambda \tau} + V_\tau \frac{1}{\lambda R_s}. \tag{A.8}$$

Thus,

$$C_n = V_0 \left(C_s - \frac{1}{\lambda R_s} \right) e^{-\lambda(n-1)\tau} + V_\tau \frac{1}{\lambda R_s} (1 + e^{-\lambda \tau} + e^{-\lambda 2\tau} + ... + e^{-\lambda(n-1)\tau}). \tag{A.9}$$

By using the relation

$$1 + x + x^2 + x^3 + ... + x^{n-1} = \frac{1 - x^n}{1 - x}, \tag{A.10}$$

The equation A.9 can be written in the compact form

$$C_n = V_0 \left(C_s - \frac{1}{\lambda R_s} \right) e^{-\lambda(n-1)\tau} + V_\tau \frac{1}{\lambda R_s} \frac{1 - e^{-\lambda n \tau}}{1 - e^{-\lambda \tau}}. \tag{A.11}$$

From the system of equations A.1 the measured current is

$$I_0 = \left(V_n - \frac{q}{C_s}\right)\frac{1}{R_s}. \tag{A.12}$$

For each step the current is measured after the settling time τ, so, for the n^{th} step, the measured current is

$$I_0^n = \left(V_n - \frac{C_n e^{-\lambda\tau} + \frac{V_0 - nV_\tau}{\lambda R_s}}{C_s}\right)\frac{1}{R_s}. \tag{A.13}$$

Finally, after simplification, the measured current is given by

$$I_0^n = \frac{V_0 - nV_\tau}{R_0 + R_s} - \frac{V_0 e^{-\lambda n\tau}}{R_0 + R_s} - V_\tau \frac{R_0}{(R_0 + R_s)R_s}\frac{e^{-\lambda\tau}(1 - e^{-\lambda n\tau})}{1 - e^{-\lambda\tau}} \tag{A.14}$$

With the assumption that $R_0 >> R_s$, which is true for our samples with MΩ resistance, and denoting $e^{-\lambda\tau}$ as α, the equation takes the form given in Section 3

$$I = \frac{V_n}{R} + I_0\alpha\frac{1 - \alpha^n}{1 - \alpha} + I_c. \tag{A.15}$$

Here $I_0 = -V_\tau/R_s$, $I_c = -V_0 e^{-\lambda n\tau}/R_0$. The time constant of charging is

$$\tau_c = 1/\lambda = \left(\frac{1}{C_s R_0} + \frac{1}{C_s R_s}\right)^{-1} \approx C_s R_s. \tag{A.16}$$

A.6 Fabrication of DNA origami

Origamis for dielectrophoretic trapping

The thiol-gold interaction was used to attach origami to the electrodes. Thiol-modified oligonucleotides were purchased unpurified at 100 nM scale from Integrated DNA Technologies (IDT). The sequences of the strands are the following:
Rectangular origami structure
For one end
5'AGCATAAAGCTAAATC CTC TCT CTC TCT CTC TCT CTC TCT CTC TCT CT /3ThioMC3-D/ 3'
5'/5ThioMC6-D/ CTC TCT CTC TCT CTC TCT CTC TCT CTC TCT CTC TGT AGC TCA ACA TGT 3'
For the other end
5'/5ThioMC6-D/ CTC TCT CTC TCT CTC TCT CTC TCT CTC TCT CTC GAC AAA AGG TAA AGT 3'
5' AAA TCA GAT ATA GAA GCT CTC TCT CTC TCT CTC TCT CTC TCT CTC TCT /3ThioMC3-D/ 3'
16 bases of each strand are complementary with M13mp18 DNA sequence on the ends, and 32 bases long repetitive CT sequence is used as a spacer between the origami structure and the thiols.
Smiley origami structure

For one side

5′ /5ThioMC6-D/ CTC TCT CTC TCT CTC TCT CTC TCT CTC TCT CTT CCT TGA AAA CAA CTT TTT 3′

5′ CAT TTC AAT TCC CTT AGA ACT CTC TCT CTC TCT CTC TCT CTC TCT CTC TCT /3ThioMC3-D/ 3′

For the other side

5′ /5ThioMC6-D/ CTC TCT CTC TCT CTC TCT CTC TCT CTC TCT CTA AAA ACA GGA AGC GAG TAA 3′

5′ GAT ATT CAA GAA AAG CCC CCT CTC TCT CTC TCT CTC TCT CTC TCT CTC TCT /3ThioMC3-D/ 3′

19 bases of each strand are complementary with M13mp18 DNA sequence on the sides, and 32 (for 3′ thiol modification) or 31 (for 5′ thiol modification) bases long repetitive CT sequence is used as a spacer between the origami structure and the thiols.

Single-stranded DNA from M13mp18 virus (New England Biolabs) was used as the scaffold for the fabrication of origami structures. The origami structures were prepared by mixing the following components (in the order of mixing)
- 5 μL 10x TAE Mg++ buffer (1x: 40 mM Tris, 19 mM acetic acid, 1 mM EDTA, 12.5 mM magnesium acetate)
- distilled water: 19.73 μL for rectangular origami structures and 18.57 μL for disk-shaped origami structures
- 5 μL of 10x T4 DNA Ligase reaction buffer (New England Biolabs, B0202S)
- 5.37 μL of 0.93 nM M13mp18 DNA
- 6.9 μL of staple strand mix (192 staple strands, each at 0.78 μM concentration) for rectangular origami structures and 8.06 μL of staple mix (224 staple strands, each at 0.67 μM concentration) for disk-shaped origami structures - 5 μL of thiol-modified side strands (each at 1 μM concentration)
- 3 μL of T4 Polynucleotide Kinase (New England Biolabs, M0201S)

T4 Polynucletide Kinase was used for adding phosphate at the 5′ end of staple strands for the following ligation procedure. The final volume of solution for anneal is 50 μL with 10 nM concentration of scaffold strand and 10x excess concentration of each staple strand. Annealing procedure was done using a PCR machine (Bio-Rad). Solution sample was first kept for 1 hour at 37 ^{o}C (optimal condition of Kinase enzyme reaction) then heated up to 90 ^{o}C and cooled down to 20 ^{o}C at the rate of 1 ^{o}C/min in 0.1 ^{o}C steps.

Origami for streptavidin assembly

For approach 1

Single-stranded DNA from M13mp18 virus (New England Biolabs) was used as the scaffold for the fabrication of origami structures. Rectangular origami structures were used as a template. Staple strands were purchased unpurified at 100 nm scale from Integrated DNA Technologies (IDT). 24 strands at the following positions had 5′ biotin modification.

r1t12f, r1t14f, r1t16f, r1t18f, r1t20f, r1t16e, r3t10f, r3t12f, r3t16f, r3t8e, r3t10e, r3t12e, r3t14e, r3t16e, r-1t10f, r-1t12f, r-1t16e, r-1t16f, r-3t10e, r-3t12e, r-3t14e, r-3t16e, r-3t8e (names according to P.W.K. Rothemund, Nature **440**, 297 (2006)).

DNA origami structures were prepared by thermal anneal of 50 μL sample with 10 nM concentration of scaffold strand and 10x excess concentration of each staple strand in 1x TAE Mg++ buffer (40 mM Tris, 1mM EDTA, 12.5 mM magnesium acetate). Annealing procedure was done using a PCR machine (24-well Piko^{TM} Thermal Cycler, Finnzymes). Solution sample was first heated up to 90 ^{o}C and cooled down to 20 ^{o}C at the rate of 1 ^{o}C/min in 0.1 ^{o}C steps. After anneal, the origami sample was diluted to 1 nM concentration with 1x TAE Mg++ Buffer. Recombinant streptavidin (STV) (Roche Applied Science) was dissolved in water (1 mg per 100 μL or $\sim$180 μM). 5 μL of 180 μM STV solution was added to 100 μL of 1 nM origami solution. The ratio of biotin modified strands to STV in final solution was $\sim$1:30 to assure that each biotin strand is modified with STV.

For approach 2

Biotin modified staple strands were diluted to 10 μM concentration in water. After that, each staple strand was mixed with 180 μM water solution of recombinant STV in 1:1 volume ratio. Mixtures were kept in 6 ^{o}C fridge for several days to allow STV attachment. After that all strand were mixed together (concentration of each staple strand in solution 0.21 μM and STV concentration 90 μM). At the final step, the solution was mixed with 900 μM water solution of biotin in 2:1 volume ration (ST/biotin ratio 1:6) to increase the thermal stability of STV. DNA origami structures were prepared by thermal anneal of 10 μL sample with 10 nM concentration of scaffold strand and 10x excess concentration of each staple strand (including those modified with STV) in 1x TAE Mg++ buffer. The sample was annealed from 70 ^{o}C to 20 ^{o}C at the rate of 1 ^{o}C/min in 0.1 ^{o}C steps.

DNA orgami structures with 50 ^{o}C - 20 ^{o}C anneal

DNA origami structures were prepared by thermal anneal of 10 μL sample with 10 nM concentration of scaffold strand and 20x excess concentration of each staple strand in 1x TAE Mg++ buffer. The sample was annealed from 50 ^{o}C to 20 ^{o}C at rate of 1 ^{o}C/min in 0.1 ^{o}C steps.

Ligation procedure

Ligation was done using T4 DNA ligase (from New England Biolabs (M0202S)) which is an enzyme that catalyses the formation of a phosphodiester bond between juxtaposed 5' phosphate and 3' hydroxyl termini in duplex DNA . The procedure was performed in the following way (for 100 μL of final solution, in the order of mixing)

- 67 μL of distilled water
- 9 μL of 10x TAE Mg++ buffer
- 9 μL of 10x Ligase reaction buffer
- 10 μL of annealed origami solution
- 5 μL of T4 DNA ligase

After mixing, the sample was kept for 8 hours in a dark place at room temperature. Origami structures are 10 times diluted from the original concentration in the annealed solution (from 10 nM to 1 nM).

Spin filtering and buffer exchange

For filtering and buffer exchange Millipore Microcon YM-100 spin filters were used (MW cutoff of 100 kDa). The procedure was done in the following way:
- 100 μL of origami sample was mixed with 300 μL of our buffer of choice and put into the YM spin filter.
- Sample was spun for 12 min at 1000 relative centrifugal force (rcf) and 4 ^{o}C.
- After that the sample was removed from the centrifuge. The filter had only a few tens of microliters of sample left in it. The filter was taken out and the liquid in the tube below was removed. Then the filter was reinserted and 400 μL of the buffer was added.
- Sample was spun for 7 min at 1000 rcf and 4 ^{o}C. This left us with 100 μL of sample retained in the spin filter.
- Finally, the spin filter was removed, placed upside down in a fresh tube and spun in a microcentrifuge for 2-3 min to collect the solution.

It is assumed that all origami structures are recovered from the filter membrane, thus filtering does not change the concentration of origami structures in the solution.

B. Materials and methods (molecular plasmonics)

B.1 Waveguide fabrication and deposition of molecules

The 5 or 10 μm wide plasmonic waveguides used in the experiments were fabricated by regular e-beam lithography and lift-off technique on ITO (Indium tin oxide) coated glass substrates. As a positive resist, a spin coated 700 nm thick layer of PMMA (Microchem C6) was used, which was baked for 5 minutes at 160ºC after the spinning. Patterning was done by Raith eLine e-beam writer using 20 kV acceleration voltage. The patterning was followed by a development in MIBK:IPA (1:3) (Methyl isobutyl ketone : isopropyl alcohol) -mixture and cleaning by IPA and a flash of oxygen plasma. After that the metallization was done in an e-beam evaporator equipped with UHV chamber. First a thin layer ($\sim$2 nm) of titanium was evaporated as an adhesion layer and after that a $100 - 130$ nm thick layer of silver was evaporated with a rate of $3 - 4$ nm/s. As a final step the rest of the resist and excess metal was stripped (lift-off) in acetone.

The immobilization of the dye molecules onto the desired locations was as well done by e-beam lithography involving a precise alignment step using marks created at the same process step as the waveguide. To avoid a destructive contamination of the areas where the molecules were not proposed, a negative SU-8 resist (Microchem SU-8 2025) was used in which the molecules were embedded. This produced an excellent contrast in a dye concentration between the patterned and unpatterned areas, especially if compared to positive resists, e.g. PMMA, which tend to leave residues on the exposed areas and thus contaminate the intended clean areas.

To produce the needed dye-SU-8 mixtures a diluted SU-8 solution was first prepared, with solid content of 22.85%, by diluting the stock solution with cyclopentanone as 1:2. The coumarin 30 (C30) was then mixed with diluted SU-8 and further diluted by cyclopentanone if needed. The concentration of C30 varied from 3.5 to 7.5 g/l and the molecular ratio between C30 and SU-8 resin varied between 2:1 and 1:2. On the other hand the rhodamine 6G (R6G) had to be dissolved into ethanol before mixing with the diluted SU-8. The used R6G concentrations varied between 1.7 and 12 g/l and molecular ratio between R6G and SU-8 between 3:8 and 6:5. The spin coating of dye solutions was always done with 3000 rpm and the concentration of the solution was used as a parameter to define the thickness of the layer. After that the patterning was done on the areas where the dye molecules were intended and the rest of the surface was cleaned using SU-8 developer (Microchem).